DISSERTATION

Plasticity of neuronal gamma-oscillations via the specific cellular plasticity of parvalbumin-positive interneurons

Plastizität neuronaler Gamma-Oszillationen durch die spezifische zelluläre Plastizität Parvalbumin-positiver Interneurone

zur Erlangung des akademischen Grades

Medical Doctor - Doctor of Philosophy (MD/PhD)

vorgelegt der Medizinischen Fakultät

Charité – Universitätsmedizin Berlin

von

Michael Hadler

Erstbetreuung: Prof. Dr. rer. nat. Jörg R. P. Geiger

Datum der Promotion: 28.02.2025

Table of contents

List of tables

List of figures

List of abbreviations

ACSF	Artificial cerebrospinal fluid
AD	Alzheimer’s disease
AMPAR	α-Amino-3-hydroxy-5-methyl-4-isoxazolepropionic receptor
CED	Cambridge Electronic Design
CFC	Contextual fear conditioning
ChR2	Channelrhodopsin 2
CI-AMPAR	Calcium-impermeable AMPAR
CP-AMPAR	Calcium-permeable AMPAR
D-AP5	D-amino-5-phosphonopentanoate
DCZ	Deschloroclozapine dihydrochloride
DG	Dentate gyrus
diH_20	Deionized water
DMSO	Dimethyl sulfoxide
DREADD	Designer receptors exclusively activated by designer drugs
EC	Entorhinal cortex
EEG	Electroencephalography
GABA	Gamma-aminobutyric acid
$GABA_AR$	$GABA_A$ receptor
GENUS	Gamma entrainment using sensory stimuli
GLM	Generalized linear model
GPCR	G-protein coupled receptor
Hz	Hertz
iGluR	Ionotropic glutamate receptor
KA	Kainate
KAR	Kainate receptor

LFP	Local field potential
LTP	Long-term potentiation
LC	Locus coeruleus
MCS	Multichannel Systems
MEA	Multi-electrode array
mGluR	Metabotropic glutamate receptor
mGluR5-PAM	mGluR5 positive allosteric modulator
MPEP	2-Methyl-6-(phenylethynyl)pyridine hydrochloride
MWU	Mann-Whitney U-Test
NASPM	Naphthyl-spermine hydrochloride
NMDAR	N-methyl-D-aspartate receptor
PCP	Phencyclidin
PKA	Protein kinase A
PKC	Protein kinase C
pMEA	Perforated MEA
PSD	Power spectral density
PVI	Parvalbumin interneuron
PVI-LTP	PVI long-term potentiation
rTMS	Repetitive transcranial magnetic stimulation
SCZ	Schizophrenia
SPW-R	Sharp-wave ripples
STDP	Spike-timing dependent plasticity
tES	Transcranial electrical stimulation
VGCC	Voltage-gated calcium channel
WSR	Wilcoxon Signed-Rank test

Abstract (English)

The synchronization of cellular activity during neuronal oscillations is considered an established mechanism of central nervous system processes. In particular, oscillations in the gamma-frequency range (30 – 80 Hertz) are regarded as biomarkers for cognitive abilities, as their spectral amplitude correlates with cortical performance in health and disease. However, it remains elusive to what extent synaptic plasticity, as occurs following learning, can influence the spectral amplitude of gamma-oscillations, and whether there is an identifiable cellular basis for the plasticity of gamma-oscillations.

This work presents a robust protocol for quantifying and mechanistically dissecting the long-term, activity-dependent increase in amplitude of ex vivo gamma-oscillations ("gamma-potentiation") using electrophysiological recordings. In acute brain slices from the mouse hippocampus, it is demonstrated that the one-time induction of gamma-oscillations leads to a long-lasting increase in the spectral amplitude of subsequent gamma-oscillations. Using pharmacological and genetic interventions it is demonstrated that gamma-potentiation can be fully explained by activity-dependent plasticity of glutamatergic synapses onto parvalbumin-positive interneurons (PVI). Two cell-type-specific metabotropic pathways specific to PVIs are required for gamma-potentiation: A canonical Gq-pathway activated by group I metabotropic glutamate receptors that recruits protein kinase C, and a Gi-sensitive pathway that recruits protein kinase A. Ultimately, gamma-potentiation is mediated by a conductance increase of calcium-permeable AMPA receptors on PVIs.

This work identifies a mutual relationship between synaptic plasticity of PVIs and network plasticity of gamma-oscillations: Gamma-oscillations induce plasticity in PVIs, which translates to an increased spectral amplitude of subsequent gamma-oscillations. This principle of cell-to-network plasticity holds potential for an improved understanding of memory processes in health, adds to current models of neuropsychiatric pathophysiology and, finally, may guide future therapeutic strategies.

Zusammenfassung (Deutsch)

Die Synchronisierung zellulärer Aktivitäten während neuronaler Oszillationen gilt als etablierter Mechanismus zentralnervöser Prozesse. Insbesondere Oszillationen im Gamma-Frequenzbereich (30 – 80 Hertz) gelten als Biomarker für kognitive Fähigkeiten, da ihre spektrale Amplitude im Gesunden wie im Krankheitszustand mit kortikaler Leistung korreliert. Hierbei blieb bisher unerforscht, inwiefern synaptische Plastizitätsprozesse, wie sie z.B. nach Lernvorgängen auftreten, die spektrale Amplitude von Gamma-Oszillationen beeinflussen können, und ob es eine identifizierbare zelluläre Grundlage für eine solche Plastizität von Gamma-Oszillationen gibt.

In dieser Arbeit wird ein robustes Protokoll vorgestellt, mit der die dauerhafte, aktivitätsabhängige Amplituden-Zunahme von ex vivo Gamma-Oszillationen („Gamma-Potenzierung“) in elektrophysiologischen Aufnahmen quantifiziert und mechanistisch aufgeschlüsselt wurde. In akuten Hirnschnitten vom Hippocampus der Maus wird demonstriert, dass die einmalige Induktion von Gamma-Oszillationen zu einer Zunahme der spektralen Amplitude späterer Gamma-Oszillationen führt. Mit Hilfe pharmakologischer und genetischer Interventionen wird aufgezeigt, dass Gamma-Potenzierung komplett erklärt werden kann durch die aktivitäts-abhängige Plastizität glutamaterger Synapsen auf Parvalbumin-positive Interneurone (PVI). Hierbei werden zwei zelltyp-spezifische metabotrope Signalwege in PVIs benötigt: Ein kanonischer Gq-Signalweg, der durch Gruppe I metabotrope Glutamatrezeptoren aktiviert wird und die Protein Kinase C rekrutiert, sowie ein Gi-sensitiver Signalweg, welcher die Protein Kinase A rekrutiert. Schlussendlich wird Gamma-Potenzierung durch eine Zunahme der Leitfähigkeit Kalzium-permeabler AMPA-Rezeptoren auf PVIs vermittelt.

Diese Arbeit identifiziert eine wechselseitige Beziehung zwischen der synaptischen Plastizität von PVIs und der Netzwerk-Plastizität von Gamma-Oszillationen: Gamma-Oszillationen induzieren Plastizität auf PVIs, welche in eine erhöhte spektrale Amplitude folgender Gamma-Oszillationen übersetzt wird. Ein solches Prinzip der Zell-zu-Netzwerk Plastizität birgt Potenzial für ein verbessertes Verständnis von Lernprozessen im Gesunden, erweitert aktuelle Modelle neuropsychiatrischer Pathophysiologie und kann letztendlich zukünftige therapeutische Strategien leiten.

1 Introduction

1.1 Gamma-oscillations as a correlate of cognitive processes

1.1.1 Gamma-oscillations in the mammalian cortex

Neuronal oscillations are periodic fluctuations of electrical currents, measured predominantly in the extracellular space of neurons. While they are present in nearly all structures of the central nervous system, the cerebral cortex has emerged as a dominant source of spectrally and functionally distinct oscillatory patterns (Buzsáki & Draguhn, 2004). Despite the functional diversity of cortical subregions, almost all cortical areas utilize similar spectra of neuronal oscillations, reflecting different states of cortical activity (Buzsáki, 2006). Different bands of neuronal oscillations can be described based on their period [or frequency, measured in Hertz (Hz) as cycles per second], shown in Table 1.

This work, summarizing the findings of Hadler et al. (2024b), focuses on gamma-oscillations, a ubiquitously occurring rhythm observed during states of cognitive processing. However, the mechanism through which gamma-oscillations support these states remains elusive. Single-cell recordings suggest that gamma-activity synchronizes local neuronal activity in short time windows, with different neuronal subtypes demonstrating a preferred activation phase. For example, hippocampal pyramidal neurons preferentially activate early in a gamma-oscillation period with certain interneurons following suit at approximately half-phase (resulting in a delay of a few milliseconds), and other neurons remain inactive (Klausberger and Somogyi, 2008). The co-activation of participating neurons through synchrony presumably facilitates the encoding of information relevant to the respective cortical area. When neuronal populations from multiple functionally specialized areas are synchronized, this enables the temporal linking of this information in neuronal *ensembles* (also referred to as "binding by synchrony"). This relationship is thought to underlie learning processes and the generation of memory contents across various modalities (Griffiths & Jensen, 2023). However, more recent analyses argue synchrony in the gamma-frequency range may rather arise from states of computation on the cellular level than underlie these, leaving the question of cause and effect of neuronal synchrony up to debate (Fernandez-Ruiz et al., 2023).

This work focuses on slow (30 – 50 Hz) gamma-oscillations in the mouse hippocampus, which have been extensively investigated both mechanistically and functionally (Hájos

and Paulsen, 2009). This study particularly addresses the plasticity of this phenomenon as an expression of cellular processes. In the following, a brief outline to analyzing oscillations is given, followed by an introduction of physiological and pathological states of neuronal oscillation plasticity.

Table 1: Neuronal oscillations in the mammalian cortex.

Band	**Frequency (Hz)**	**Function (exemplary)**
Delta	0.5 – 4	Decoupling from peripheral inputs during sleep
Theta	4 – 10	Synchronization of distant cortical areas and pacemaker for faster, local rhythms (e.g., gamma)
Alpha	10 – 15	Cortical reflection of thalamocortical inputs
Beta	15 – 30	Initiation and execution of movements (motor areas)
Gamma	**30 – 120**	Encoding of area-specific cognitive functions (e.g., declarative memory processes in the hippocampus or contrast processing in the visual cortex)
Ripple	120 – 250	"Memory trace" during rest or sleep phases. Often accompanied by a "sharp wave"

Own representation. Contents adapted from Buzsáki, 2006.

1.1.2 Physiological plasticity of neuronal oscillations

Gamma-oscillations typically occur in vivo within brief intervals (< 1 second), which can be described based on three essential qualities:

- When (and where) does an oscillatory signal appear?
- Which frequencies characterize the signal?
- Which spectral amplitudes (“power”) represent the respective frequencies?

This work focuses on changes in gamma-oscillation power. The recorded magnitude of power depends on two factors: 1. The properties of the measuring device [e.g., electrodes of electroencephalograms (EEG)] and its localization relative to the signal source. 2. The factual amplitudes of the involved electrical currents (Chapter 1.2.3). Biologically relevant

changes of neuronal oscillations are due to the latter point, including short-term, transient changes of neuronal excitability (e.g., the transition from wakefulness to sleep) and long-term changes in local neuronal connections. The long-lasting *plasticity* of oscillation power caused by such changes occurs physiologically over two time scales (Figure 1):

1. Postnatal development (years): In humans, task-specific gamma-oscillations are observable from childhood, e.g., in EEG recordings during the recognition-based *Mooney Face Test*. Task-related gamma-power positively correlates with age and task performance, reaching a plateau in young adulthood (16 – 25 years). This development-dependent plasticity correlates with simultaneous changes in the number and weighting of cortical synaptic connections, including of inhibitory interneurons (Uhlhaas and Singer, 2010).
2. Learning (minutes to days): The effects of learning on neuronal oscillations have been extensively studied following classical and operant conditioning in the hippocampus of rodents. For example, classical fear conditioning (CFC) causes power increases of theta-, gamma-, and ripple-oscillations (Ognjanovski et al., 2017; Xia et al., 2017; He et al., 2021). Learning-induced plasticity of neuronal oscillations continues to occur in adult animals following the plateau reached during postnatal development.

Both developmentally and learning-associated changes of gamma-power correlate with the activation of a specific neuronal cell-type: Inhibitory interneurons expressing the anti-oxidant parvalbumin (parvalbumin-positive interneurons, PVIs). During postnatal development, the synaptic connectivity of PVIs increases dramatically (Uhlhaas and Singer, 2010), contributing to the generation of gamma-oscillations through enhanced synaptic inhibition (Chapter 1.2.3). Additionally, changes in neuronal oscillations observed after learning processes and the success of the learning process itself have been attributed to the selective activation of this cell class in several animal experiments (Karunakaran et al., 2016; Ognjanovski et al., 2017; Xia et al., 2017; He et al., 2021).

As physiologically occurring plasticity processes correlate with cognitive performance, detrimental changes of gamma-oscillations accompany pathological states of reduced cognitive performance, which is discussed in the following.

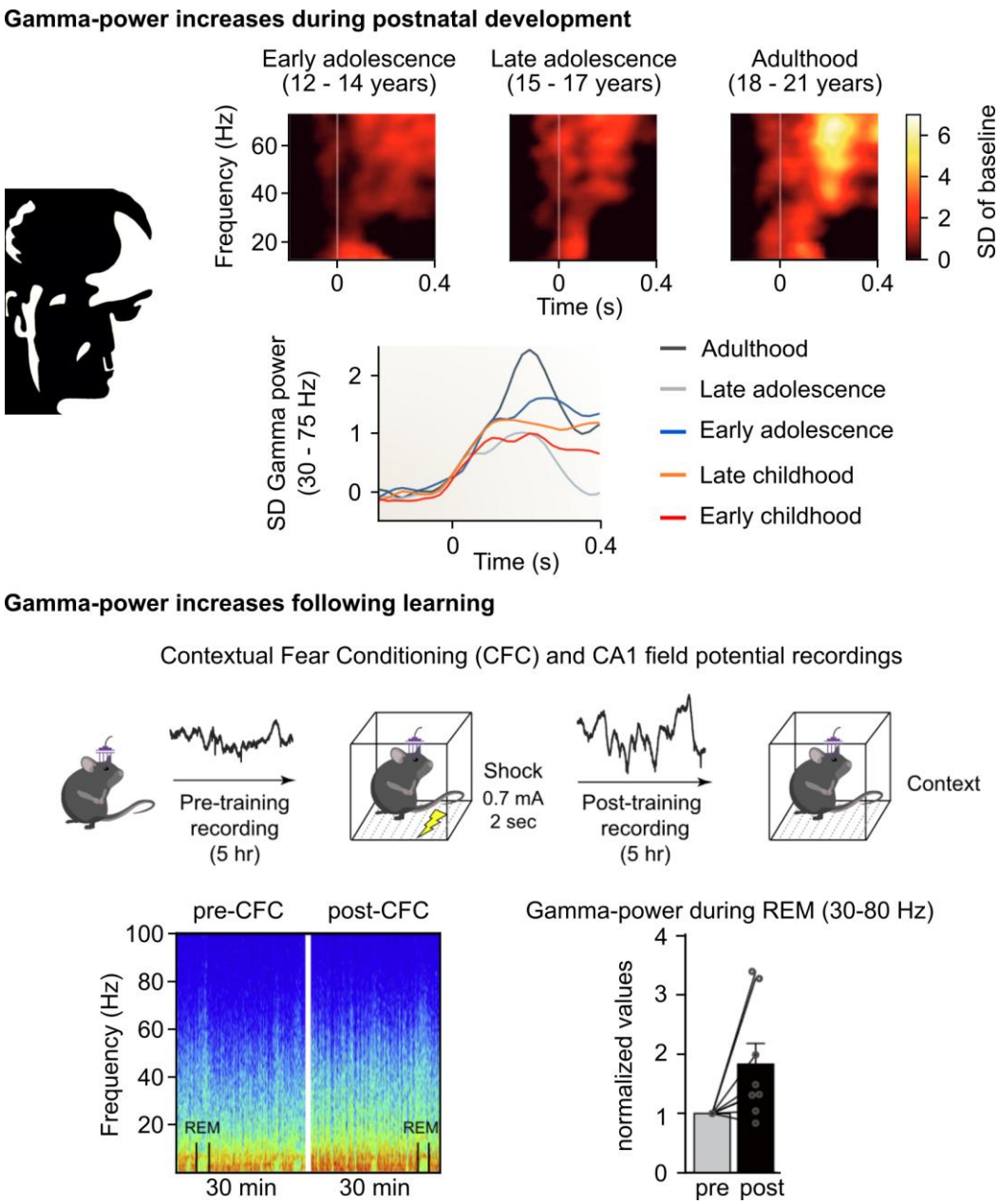

Figure 1: Physiological plasticity of gamma oscillations.

Above: Spectrograms of human parietal EEG-recordings at different ages during the "Mooney Face Test" (image on left) and time-power curves averaged from a population of human subjects. The highest response [standard deviation (SD) from baseline gamma-power (30 – 75 Hertz, Hz)] is observed in adulthood. Adapted from Figures 2 and 5 from Uhlhaas and Singer (2010). Below: Contextual fear conditioning (CFC) in mice induces gamma-power increases within hours. A mouse is implanted with electrodes in the CA1 region, and recordings performed before and after conditioning (spectrograms below). Periods of rapid-eye movement (REM)-sleep are identified for analysis. Following training, gamma-power is increased. Adapted from Figure 7 in He et al. (2021).

1.1.3 Pathological plasticity of neuronal oscillations

Several neurological or neuropsychiatric diseases are accompanied by disruptions in neuronal oscillations. The transition between healthy and diseased states represents a process of pathological plasticity. Depending on the underlying condition, this manifests as the occurrence of physiologically irregular oscillations (e.g., hypersynchronization in epilepsy), the functionally inadequate occurrence of physiological oscillations (e.g., beta-oscillations of the subthalamic nucleus in Parkinson's disease), or the absence or restriction of physiological oscillations during regular cognitive processes. Restrictions of gamma-oscillations occur, amongst others, in two distinct neurodevelopmental diseases (Figure 2):

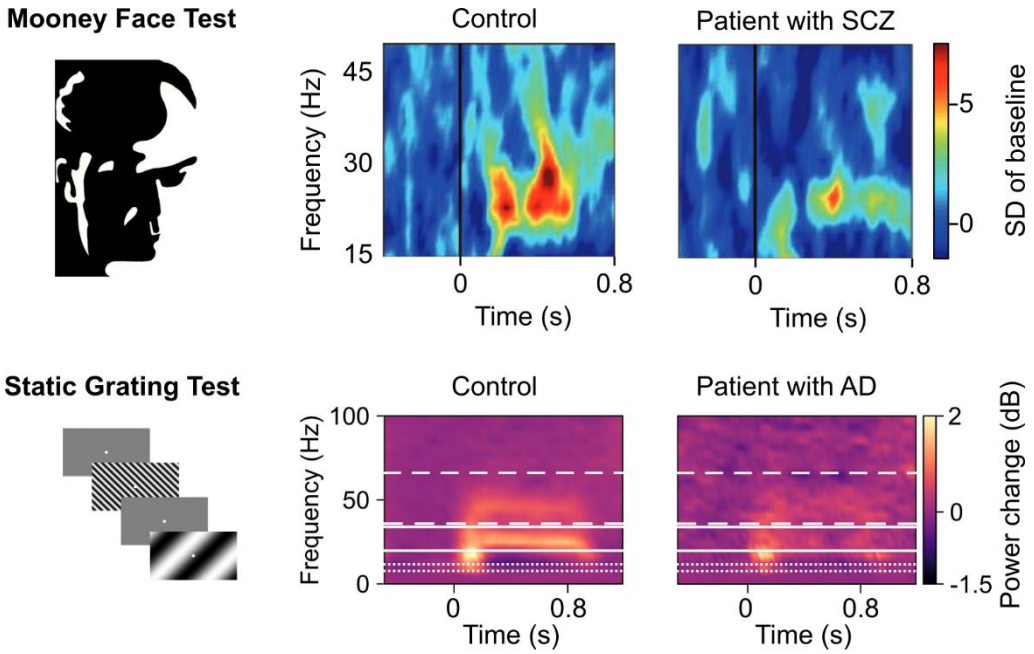

Figure 2: Gamma-oscillation power is reduced in patients with schizophrenia and Alzheimer's disease.

Exemplary spectrograms of EEG recordings from the parietal cortex of patients with schizophrenia (SCZ) or Alzheimer's disease (AD). Above: Exemplary image from the Mooney Face Test. The evoked power in the gamma-frequency range is reduced in SCZ patients, quantified as the standard deviation (SD) of baseline power (adapted from Figure 2 in Uhlhaas and Singer, 2010). Below: A static grating test evokes gamma-oscillations in participants. The power is reduced in AD patients, quantified as changes in decibel (dB; adapted from Figures 1 and 3 in Murty et al., 2021).

- Schizophrenia (SCZ): A mental disorder prevalently manifesting in late adolescence to early adulthood and characterized by psychotic, anhedonic and cognitive symptoms. EEG studies in SCZ patients reveal different, sometimes conflicting changes in gamma-power: During states of predominantly psychotic symptoms, an abnormal increase in gamma-power at rest can be observed. On the other hand, task-evoked oscillations (e.g., following auditory stimuli or the Mooney Face Test) demonstrate reductions of gamma-power (Uhlhaas and Singer, 2010).
- Alzheimer's disease (AD): Neurodegenerative disease and the most common form of dementia. The accumulation of tau-protein and Aβ-peptide triggers a cascade of neuronal cell death, manifesting as progressive anterograde and retrograde amnesia. Preclinical studies in AD mouse models and humans show that gamma-oscillations exhibit power deficits in early, minimally symptomatic stages, which progresses with increasing memory loss (Murty et al., 2021; Hijazi et al., 2023).

SCZ and AD are multifactorial conditions with no specifically attributable cause, which complicates the search for targeted therapeutic strategies. Encouragingly, both post-mortem examinations of identified SCZ or AD patients and preclinical studies in corresponding animal models point to a cellular source of defective gamma-oscillations: PVIs, which contribute to the generation of gamma-oscillations (Chapter 1.2.3) and the physiological plasticity of neuronal oscillations (Chapter 1.1.2), exhibit disease-related deficiencies in their anatomical and physiological properties (Hijazi et al., 2023; McCutcheon et al., 2023). PVIs are therefore considered a promising target for therapeutic interventions: In animal models of SCZ and AD, deficits of gamma-oscillations and cognitive performance are alleviated by activation of PVIs. To this end, the chemogenetically active, Gq-coupled hM3Dq-receptor (Marissal et al., 2018; Huang et al., 2021) and the optogenetically active cation channel channelrhodopsin 2 (ChR2) have emerged as powerful tools specifically activating PVIs (Cho et al., 2015; Etter et al., 2019). Despite these successes, an understanding of how PVI activation by such tools eases behavioural deficits is still lacking (Figure 3).

The central role PVIs hold in neuropsychiatric pathology and treatment of these etiologically and phenomenologically distinct conditions may emanate from their close connection to the generation of the gamma-rhythm and its physiological plasticity. This warrants a closer examination of the mechanistic foundations of gamma-oscillations, particularly in the intensively studied rodent hippocampus.

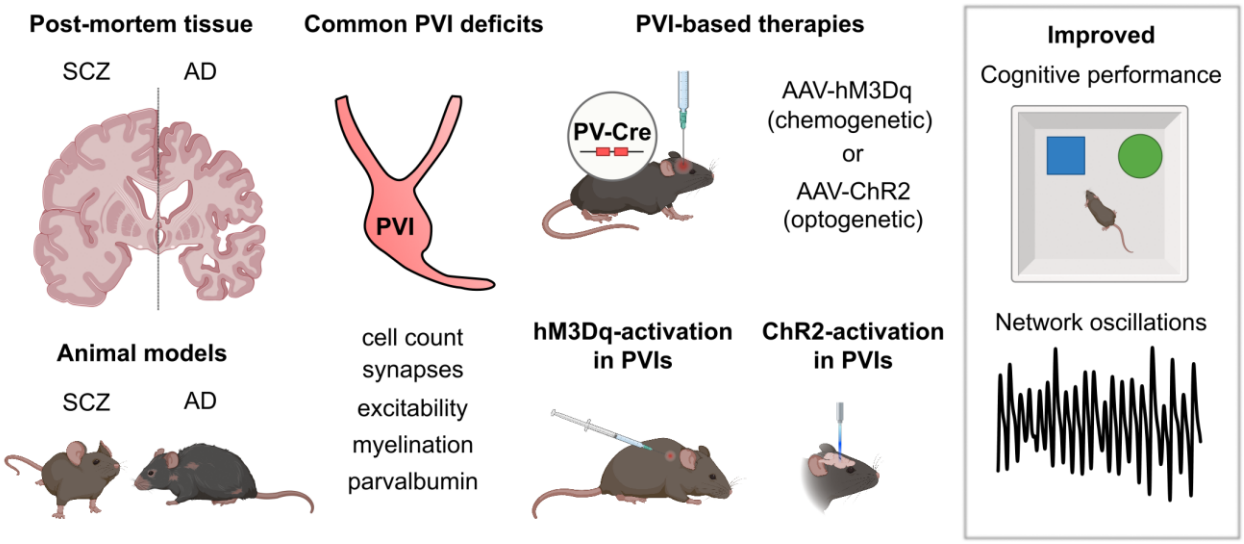

Figure 3: Parvalbumin interneurons in schizophrenia and Alzheimer's disease.

Left: Schematic of post-mortem tissue (above) obtained from patients with schizophrenia (SCZ, left) or Alzheimer's disease (AD) and animal models of both diseases (below). Despite morphological differences between SCZ and AD tissue, e.g. pronounced neurodegeneration in AD, deficits of parvalbumin interneuron (PVI) functions are common to both diseases, including reduced cell count, PVI synapses and the expression of parvalbumin. Right: In animal models, viral (adeno-associated virus, AAV) expression of chemogenetic (hM3Dq) or optogenetic (channelrhodopsin 2, ChR2) tools specifically under the parvalbumin promoter (PV-Cre) underlie PVI-based therapies. Applying these leads to improved cognitive performance in animals, illustrated here in an object recognition task, and improved network oscillations. Adapted from Figure 2 in Hadler et al., 2024a.

1.2 Cellular and synaptic foundations of hippocampal gamma-oscillations

The neuronal cell bodies of the hippocampus are densely packed in the pyramidal cell layer of the *cornu ammonis*, which is divided into three sections (CA3, CA2, and CA1). This work focuses on the CA3 subregion. Approximately 70 – 90% of CA3 neurons are excitatory pyramidal neurons and 10 – 30% inhibitory interneurons. Both cell classes receive synaptic inputs from outside the hippocampus and form reciprocal synaptic connections amongst each other.

1.2.1 Glutamatergic transmission

Synapses originating from pyramidal neurons release glutamate and act excitatory by activating postsynaptic ionotropic glutamate receptors (iGluRs). iGluRs are nonselective cation channels comprising receptors sensitive to α-amino-3-hydroxy-5-methyl-4-isoxazolepropionic (AMPARs), N-methyl-D-aspartate (NMDARs) or kainate (KARs). The proportion of each receptor varies with the observed synapse type (Kullmann and Lamsa, 2007; Reiner and Levitz, 2018):

- Synapses targeting pyramidal neurons contain NMDARs and AMPARs with low calcium permeability (calcium-impermeable AMPARs, CI-AMPARs).
- Synapses targeting interneurons contain a lower density of NMDARs and CI-AMPARs, instead expressing calcium-permeable AMPARs (CP-AMPARs). The redistribution towards CP-AMPARs is pronounced in PVIs (Geiger et al., 1995).
- KARs are predominantly expressed extrasynaptically.

Metabotropic glutamate receptors (mGluRs) are G-protein coupled receptors (GPCRs) that trigger intracellular signaling cascades and mediate, amongst others, synaptic plasticity. Group I mGluRs (mGluR1 and mGluR5) locate postsynaptically and activate Gq-proteins, which, through divergent pathways, increase cytosolic calcium levels and activate protein kinase C (PKC). Upon sufficient activation, this facilitates an increase of glutamatergic transmission (Chapter 1.3). Group II/III mGluRs (mGluR2-4 and mGluR6-8) locate presynaptically and activate Gi-proteins, which inhibit synaptic transmission. This work focuses on group I mGluRs.

1.2.2 GABAergic transmission

Synapses originating from interneurons release gamma-aminobutyric acid (GABA) and target ionotropic $GABA_A$ receptors ($GABA_ARs$) and metabotropic $GABA_B$ receptors. The latter, targeting Gi-proteins, is not further discussed in this work.

$GABA_ARs$ are nonselective anion channels with a reversal potential of roughly -65 mV. Upon activation, they exert their inhibitory effect by "*shunting*" the postsynaptic membrane potential, effectively short-circuiting incoming depolarizations (Bartos et al., 2007). Therefore, the activation and inactivation times of $GABA_ARs$ create a time window of postsynaptic inactivity, setting the foundation for synchronization in the gamma-rhythm.

1.2.3 Generation of gamma-oscillations in the CA3 microcircuit

The CA3 pyramidal neuron population is characterized by an increased excitability, which, upon activation, generates a burst of uncoordinated, divergent glutamatergic excitation. This convergently excites the local interneuron population through iGluRs, which in turn prompts wide-spread GABA-mediated inhibition of the pyramidal neuron population. Once $GABA_ARs$ have inactivated, the pyramidal neuron population resumes its activity in a tighter temporal sequence, having followed their GABAergic pacemakers. Their activities are *synchronized*, and the same interplay of excitation and *feedback* inhibition is repeated with higher precision until a state of reproducible periodicity between both cell populations is achieved. This interaction persists until the pyramidal neuron excitation ceases (Bartos et al., 2007; Hájos and Paulsen, 2009). Sources of excitation include mossy fiber inputs from the dentate gyrus (DG), the entorhinal cortex (EC), or excitatory neuromodulation via cholinergic inputs. These processes also excite the interneuron population, which pre-emptively synchronizes pyramidal neuron activities (*feedforward inhibition*). The facultative independence of CA3 gamma-oscillations from external sources, however, is supported by in vivo experiments demonstrating them following surgical transection of extrahippocampal inputs (Bragin et al., 1995).

The generation of specific oscillation frequencies depends on the interneuron population's composition, which represents an anatomically and physiologically diverse cell group (Tzilivaki et al., 2023). Essential for the gamma-rhythm are PVIs, which constitute roughly half the interneuron population in CA3 and are intricately connected to the surrounding microcircuit. They receive glutamatergic inputs with high convergence and form

fast GABAergic synapses with high divergence on the somata and axons of pyramidal neurons and other interneurons. Their inputs have a high proportion of CP-AMPARs, characterized by rapid kinetics and high single-channel conductance, and they reach action potential frequencies of > 300 Hz. This functional specialization renders them particularly suited to rapidly respond to suprathreshold changes in pyramidal neuron excitation and synchronize the local network in the gamma-frequency range (Hu et al., 2014).

The periodic interplay between pyramidal neurons and PVIs underlies the generation of the gamma-rhythm in nearly all cortical areas. Ultimately, the synaptic currents passing the synchronized cell membranes cumulate, making them measurable and quantifiable in the extracellular space (Figure 4). Considering Chapters 1.1.2 – 1.1.3, changes in these conductances, particularly in PVIs, represent a likely source of physiological and pathological plasticity of gamma-oscillations.

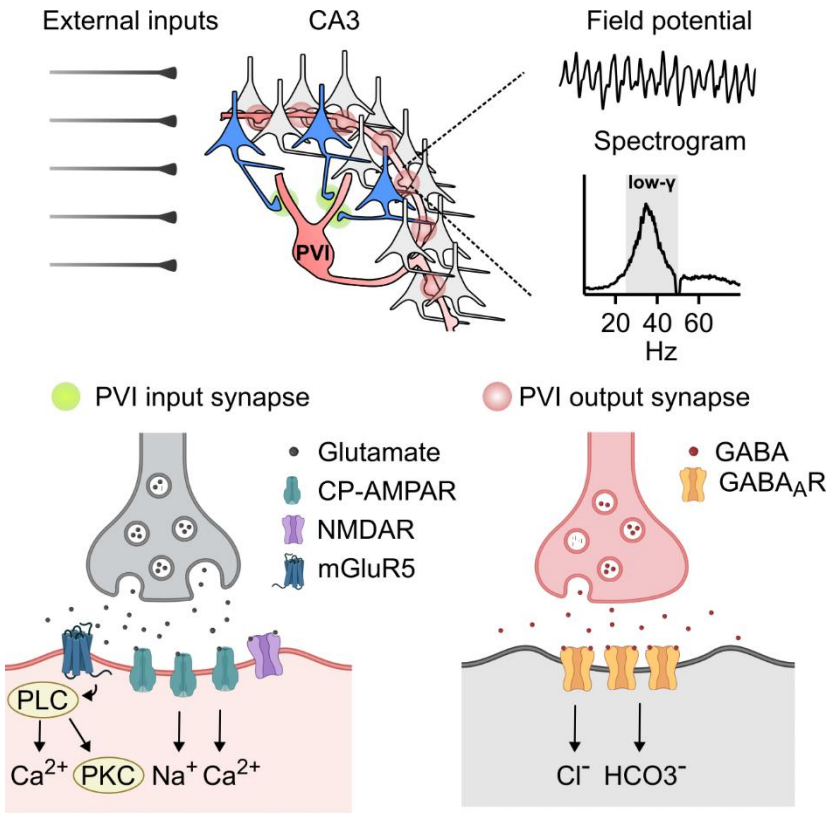

Figure 4: Cellular mechanisms of gamma-oscillations.

Above: External inputs drive the CA3 network, activating pyramidal neurons (blue), which target a parvalbumin interneuron (PVI, red) at convergent, calcium-permeable AMPA receptor (CP-AMPAR) containing glutamatergic synapses (green highlight). The PVI subsequently inhibits the pyramidal neuron population at divergent GABAergic synapses (red). The cumulative, rhythmic activity of the CA3 population is recorded in the field potential. Spectral analysis reveals a peak in the low gamma-frequency range (inset 'low-γ'; 25 – 50 Hertz, Hz). Below: Schematics of the PVI input and output synapses highlighted above. Excitatory transmission at the input synapse is mediated via CP-AMPARs and NMDA receptors (NMDARs) permeable for sodium (Na^+) and calcium (Ca^{2+}) and metabotropic glutamate receptor 5 (mGluR5), which activates a metabotropic cascade via phospholipase C (PLC), protein kinase C (PKC) and Ca^{2+}. Inhibitory transmission requires $GABA_A$-receptors ($GABA_ARs$) permeable for chloride (Cl^-) and hydrogen carbonate ($HCO3^-$). Own illustration. Created with BioRender.com.

1.3 Interactions of network oscillations and synaptic plasticity

The previous chapters outline an overview of gamma-oscillations at the synaptic, cellular, and network levels, which accompany cognitive processes in health and serve as a biomarker for impaired cognition in AD and SCZ. Understanding changes in gamma-oscillation power on the network level therefore requires corresponding connections to changes in synaptic and cellular function. An essential connection in this regard is the ability of gamma-oscillations to trigger cell-type specific, long-lasting synaptic plasticity.

1.3.1 Previous work: Cell-type specific synaptic plasticity induced by network oscillations.

Gamma-oscillations represent a state of increased neuronal activity in which both pyramidal neurons and interneurons elevate their action potential frequency. Interneuronal inhibition creates a preferred time window of co-activation within an oscillation cycle, promoting the induction of *spike-timing dependent plasticity* (STDP).

A previous study in the mouse hippocampus confirms this notion (Zarnadze et al., 2016): In single-cell recordings before, during, and after gamma-oscillations ex vivo, the authors observed changes in glutamatergic and GABAergic transmission on the participating neurons. However, the expression of synaptic plasticity depended on cell-type: Both glutamatergic and GABAergic inputs expressed long-term potentiation (LTP) on pyramidal neurons, with the relative increase in glutamatergic inputs prevailing, rendering them more excitable. This effect was increased in PVIs, which also expressed LTP at glutamatergic inputs yet reduced GABAergic inputs. In both cell types, the expression of glutamatergic LTP was mediated by mGluR5. Another group of interneurons, co-expressing the peptide cholecystokinin and themselves active during the gamma-episode, experienced net reduction of their excitability: Glutamatergic inputs remained unchanged, and GABAergic inputs expressed LTP. Therefore, gamma-oscillations cause a cell-type-specific change in effective synaptic connectivity at the local network level.

This was accompanied by an increased amplitude of coincident sharp-wave ripples (SPW-Rs), which positively correlated with the preceding power of gamma-oscillations. Therefore, a connection could be established between changes of synaptic amplitudes and concurrent network oscillations (Figure 5).

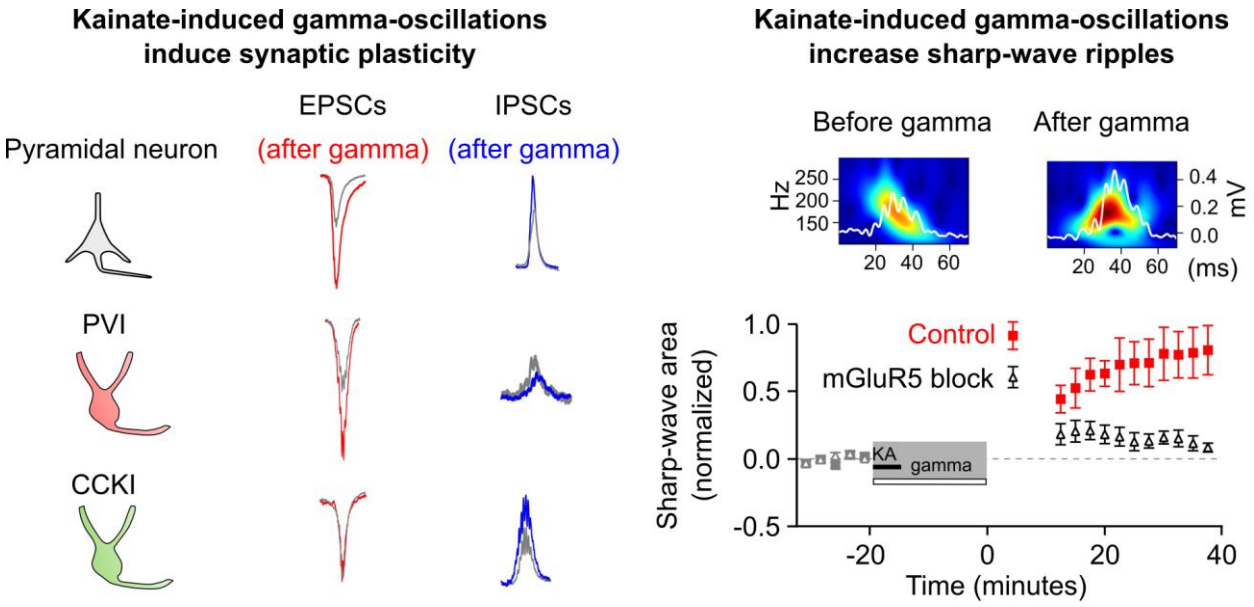

Figure 5: Gamma-oscillations induce cell-type specific synaptic plasticity.

Left: Kainate (KA)-induced gamma-oscillations induce cell-type specific changes in excitatory (EPSCs) and inhibitory postsynaptic currents (IPSCs). Schematics of a pyramidal neuron (grey), parvalbumin interneuron (PVI, red), and cholecystokinin interneuron (CCKI) next to respective exemplary EPSCs and IPSCs measured before (grey) and after gamma-oscillations (EPSCs in red, IPSCs in blue). EPSCs and IPSCs are increased in pyramidal neurons. In PVIs, EPSCs are increased following gamma-oscillations, but IPSCs are decreased. In CCKIs, EPSCs are unaltered and IPSCs are increased. Right: The amplitude of sharp-wave ripple (SPW-R) complexes is increased following an interval of KA-induced gamma-oscillations. Two field potential traces of SPW-Rs and their wavelet-transforms before and after gamma-oscillations are shown. Below: The increase of SPW-R amplitude is prevented by pharmacological blockade of metabotropic glutamate receptor 5 (mGluR5). Adapted from Figures 2, 4, 5 and 6 in Zarnadze et al., 2016.

1.3.2 Motivation of the study

Under consideration of Chapters 1.1–1.2 and Chapter 1.3.1, the following speculations can be made:

- Since gamma-oscillations induce LTP in pyramidal neurons and PVIs, and synaptic interactions between pyramidal neurons and PVIs generate gamma-oscillations, later episodes of gamma-oscillations should exhibit changes in their spectral properties, e.g. their power.
- As both the physiological and pathological plasticity of gamma-oscillations correlates with activities or changes in PVIs, the gamma-induced LTP of PVIs (PVI-LTP) may specifically contribute to plasticity of later gamma episodes.
- Preclinical interventions selectively activating PVIs are expressed, among other effects, by an increase in gamma-power and associated cognitive performance. Therefore, such interventions may act by inducing physiological plasticity of gamma-oscillations.

1.4 Hypotheses

The speculations in Chapter 1.3.2 motivate a series of experimentally testable hypotheses. Three core hypotheses will be explored in this work in an isolated ex vivo model of gamma-oscillations:

1. Do network oscillations in the gamma-frequency range undergo self-induced, activity-dependent, and long-lasting plasticity?
2. Can plasticity of gamma-oscillations be explained by synaptic plasticity, and to what extent does the cell-type-specific plasticity of PVIs contribute?
3. Do preclinically effective interventions targeting PVIs induce plasticity of gamma-oscillations?

2 Methods

2.1 Animal models

A list of mouse strains bred for acute brain slice preparation is given by Table 2:

Table 2: List of mouse models.

Mouse model	Description	Origin (repository)
C57Bl6/J	„Wild-type“	The Jackson Laboratory (RRID:IMSR_JAX:000664)
PV-Cre	Expression of Cre-Recombinase upon activation of the parvalbumin promoter.	The Jackson Laboratory (RRID:IMSR_JAX:017320)
Ai9	Knock-in of red fluorophore "tdTom". Expression after Cre-mediated recombination.	The Jackson Laboratory (RRID:IMSR_JAX:007909)
Loxp-mGluR5	Deletion of Grm5 exon 7 after Cre-mediated recombination; conditional mGluR5 knock-out.	The Jackson Laboratory (RRID:IMSR_JAX:028626)
Loxp-hM3Dq	Knock-in of xeno-receptor "hM3Dq". Expression after Cre-mediated recombination.	The Jackson Laboratory (RRID:IMSR_JAX:026220)
Flex-hM4Di	Knock-in of xeno-receptor "hM4Di". Expression after Cre-mediated recombination.	Provided by Benjamin Rost, DZNE Berlin (MGI:7528984)

Adapted from Hadler et al., 2024b.

PV-Cre animals were selectively cross-bred into four PVI-targeting mutants:

- PV-mGluR5: PV-Cre cross-bred with loxp-mGluR5. Offspring were homozygous for PV-Cre and either homozygous carriers or non-carriers of loxp-mGluR5 ("PV-mGluR5 KO" or "PV-mGluR5 WT").
- PV-Ai9: PV-Cre cross-bred with Ai9. Offspring were heterozygous für each allele. Control for PV-Ai9-hM4Di experiments.

- PV-Ai9-hM4Di: PV-Cre cross-bred with Ai9 and Flex-hM4Di. Offspring were heterozygous für each allele.
- PV-Ai9-hM3Dq: PV-Cre cross-bred with Ai9 and loxp-hM3Dq. Offspring were heterozygous für each allele.

2.2 Acute brain slice preparation

Adolescent mice [postnatal day 45 to 70, either males (C57Bl6/J) or both sexes (PV-mGluR5, PV-Ai9, PV-Ai9-hM4Di, PV-Ai9-hM3Dq)], were sacrificed in accordance with the guidelines of the Berlin State Office for Health and Social Affairs [Landesamt für Gesundes und Soziales (LAGeSo), licenses T0045/15 and T-CH0014/23].

Animals were anaesthetized with isoflurane, decapitated, and their brains transferred to cooled (4°C) sucrose-based saline (composition in mM: sucrose 75, NaCl 87, KCl 2.5, $NaHCO_3$ 25, NaH_2PO_4 1.25, $MgCl_2$ 3, $CaCl_2$ 0.5, glucose 10) saturated with carbogen (95% O_2, 5% CO_2). Each hemisphere was glued on its dorsal side and sectioned along the horizontal axis using a Leica VT 1200S microtome (Leica Biosystems). Up to 8 hippocampal slices were transferred to "interface" chambers and perfused with artificial cerebrospinal fluid (ACSF, in mM: NaCl 129, KCl 3, $NaHCO_3$ 21, NaH_2PO_4 1.25, $MgSO_4$ 1.8, $CaCl_2$ 1.6, glucose 10, 32–34 °C) under maximal carbogen saturation (1.3 L/min). Electrophysiological recordings were initiated after two hours under these conditions. In a series of experiments, "CA1-Mini" slices were prepared, in which the CA1 region of a slice was surgically isolated with a scalpel (Hadler et al., 2024b).

2.3 Electrophysiology

2.3.1 Local field potential (LFP)–recordings

Local field potential (LFP) recordings were performed in the CA3 and/or CA1 subregion. Borosilicate glass capillaries (GB150F-10P, Science Products) were pulled into micropipettes (P-97 Flaming/Brown, Sutter Instruments), filled with ACSF and used with chlorinated silver wire as electrodes (pipette resistance 3–10 megaohm). Electrodes were connected to a multi-amplifier system (EXB-EXT-02B, npi Electronic), signals digitized using an analog-to-digital converter [CED 1401, Cambridge Electronic Design (CED)] and stored to hard drive (Spike2, CED). By connecting multiple amplifiers, up to 16 channels could be recorded simultaneously. Sampling frequency was set at 5 kHz.

All LFP plasticity recordings followed the same protocol (Hadler et al., 2024b):

1. Baseline recording of spontaneous network activity (30 minutes)
2. First application period of kainate („KA_1“, 150 nM, 30 minutes)
3. Kainate washout, restoration of spontaneous activity ("Washout," 60 – 180 minutes)
4. Second application period of kainate („KA_2“, 150 nM, 30 minutes)
5. Kainate washout, end of recording (40 – 60 Minuten)

Pipette resistences were determined with a resistometer (EXB-REL08B, npi Electronic) before and after recordings and recordings with deviations >10% were discarded.

2.3.2 Multi-electrode array (MEA)-recordings

Multi-electrode array (MEA)-recordings were performed using a MEA2100-HS(2x)60 recording system [Multichannel Systems (MCS)], allowing for two parallel recordings with 60-channel MEAs featuring a 6 x 10 electrode configuration (100 µm inter-electrode spacing; Model 60pMEA100/30iR-Ti-gr, MCS). Slices were transferred from interface chambers to the ACSF-filled MEA chambers and positioned with the pyramidal neuron layer of CA3 on the electrodes. All measurements were conducted with perforated MEAs (pMEAs) and negative pressure applied with a vacuum pump (CVP-230V, MCS). MEA chambers were perfused with warm ACSF (32 – 34 °C) at a high flow rate (10 mL/min).

After an adaptation interval of 20 minutes, a 5-minute recording of spontaneous network activity was initiated (Multichannel Experimenter Software, MCS) to confirm good adherence of the slice. Subsequently, a 10-minute recording for the quantification of network oscillations was started, during the first 3 minutes of which kainate (200 nM) was intermittently applied. Sampling frequency was set at 20 kHz.

2.4 Pharmacology

All pharmacological agents reported in this study are listed in Table 3.

Table 3: List of pharmacological agents.

Substance	Manufacturer	Solvent
D-amino-5-phosphonopentanoate (D-AP5)	Cayman Chemicals	diH_2O
Deschloroclozapine dihydrochloride (DCZ)	Cayman Chemicals	diH_2O
GF 109203X	Tocris	DMSO
GYKI-53655 hydrochloride (GYKI-53655)	Hellobio	diH_2O
H-89	Cayman Chemicals	DMSO
JNJ-16259685	Tocris	DMSO
Kainat (KA)	Tocris	diH_2O
ML-218	Tocris	DMSO
2-Methyl-6-(phenylethynyl)pyridine hydrochloride (MPEP)	Cayman Chemicals	diH_2O
Naphthyl-spermine hydrochloride (NASPM)	Cayman Chemicals	diH_2O
Nifedipine	Tocris	DMSO
UBP-302	Tocris	DMSO

Adapted from Hadler et al., 2024b. diH_2O: deionized water; DMSO: dimethyl sulfoxide

Substances were stored as stock solutions in their respective solvents, including deionized water (diH_2O) or dimethyl sulfoxide (DMSO) at -20° C. Prior to the experiment, substances were thawed and dissolved in ACSF at their final concentrations. When testing DMSO-solved substances, control experiments were conducted with an equivalent dose of DMSO.

2.5 Analysis

All recordings were analyzed with custom-written code in MATLAB [The MathWorks; (Hadler et al., 2024b)].

2.5.1 LFP-experiments

1. Bandpass (1 - 100 Hz, 12-pole IIR digital filter) and bandstop (stop frequency 49 - 51 Hz, 12-pole IIR digital filter) filtering of the entire recording.
2. Recordings divided into 30-second segments and power spectral densities (PSD) calculated using the Welch method ("pwelch" function, frequency resolution 0.34 Hz).
3. Recordings with a decrease of power > 10% during KA_1 or KA_2 were excluded from further analysis.
4. Identification of a 10-minute interval during KA_1 reporting maximum cumulative power. PSD calculated as in point 2 and repeated in the corresponding time interval around KA_2.
5. Maximum amplitude ("Peak Power") and frequency values ("Peak Frequency") extracted for both intervals. Calculation of the relative increase in Peak Power ("Potentiation", Peak Power KA_2/Peak Power KA_1).

2.5.2 MEA-experiments

Steps 1 and 2 performed as in LFP-experiments (Chapter 2.5.1).

3. Selection of electrodes based on the positive polarity of SPW-Rs (pyramidal cell layer of CA3) and photographic documentation.
4. Identification of the 2-minute interval reporting maximum cumulative power across all electrodes. PSD calculated as in point 2.
5. Maximum amplitude ("Peak Power") and frequency values (“Peak Frequency”) extracted.
6. „Lead electrode“ identified based on the maximal power value.
7. Intralaminar inter-electrode distances calculated relative to the "Lead Electrode" as the sum of individual distances between adjacent electrodes ("shortestpath" function).

2.6 Statistics and data visualization

Statistical analyses and data visualization were performed in R 4.1.3 (Hadler et al., 2024b):

Absolute peak power values are reported as median [1st quartile; 3rd quartile] and compared non-parametrically using the Mann-Whitney U-test (MWU; unpaired comparisons) or the Wilcoxon Signed-Rank Test (WSR; paired comparisons).

Data points of positive-only and positively skewed parameters (Potentiation, Peak Frequency) were approximated with a generalized linear model (GLM) using the log-transformed gamma-function. Means, standard errors, t-statistics and group comparisons were obtained using the "emmeans" package.

P-values from group comparisons were adjusted using the Bonferroni-Holm correction. Statistical significance is reported below an alpha-level of 0.05.

2.7 Data and code availability

All data and statistical analyses reported in this work, (DOI: 10.5281/zenodo.8383858) and analysis scripts (DOI: 10.5281/zenodo.8432332), are archived indefinitely on the Zenodo platform.

3 Results

This chapter summarizes the results of “Gamma oscillation plasticity is mediated via parvalbumin interneurons” [Hadler et al. (2024b); page 72 in this thesis]. Exemplary figures of the publication are re-purposed here and referred to as self-citations.

3.1 Gamma-potentiation in the mouse hippocampus

3.1.1 LFP-protocol for the analysis of network plasticity in paired samples

In LFP recordings of hippocampal CA3 in slices from wild-type mice (C57Bl6/J, Chapter 2.1), bath application of KA induced network oscillations in the low gamma-frequency range (25 – 45 Hz). This was done twice (KA_1 and KA_2) at intervals of one or three hours and yielded two major findings (Figure 6):

- In KA_2, gamma-power was significantly and robustly increased compared to KA_1 after either one or three hours ([1 hour] KA_1: 5.66 [1.88; 16.93] µV² vs. KA_2: 11.84 [3.40; 32.50] µV², n = 15 slices; WSR, $p = 0.61 \times 10^{-5}$; [3 hours] Peak Power KA_1: 18.76 [10.42; 24.55] µV² vs. KA_2: 61.59 [26.94; 86.08] µV², n = 10 slices; WSR, $p = 0.58 \times 10^{-3}$).
- Double re-application of KA after one and three hours (KA_3) did not induce a cumulative increase in gamma-power measured after three hours (Potentiation [3h Control]: 2.64 +/- 0.27, n = 11 slices, vs. [1 + 3h]: 2.72 +/- 0.29, n = 10 slices; GLM, p = 0.84).

These findings demonstrate a reproducible protocol by which the one-time induction of gamma-oscillations induces a saturating long-lasting increase of gamma-oscillation power (“gamma-potentiation”), which can be measured and quantified within the same slice. Later sub-chapters report experimental series in which the magnitude of gamma-potentiation (Peak Power KA_2 / Peak Power KA_1) was quantified and compared following pharmacological and/or molecular interventions after one hour. Re-evaluation of the respective control cohorts revealed the mean magnitude of gamma-potentiation consistently ranged between 2 – 2.5 (Chapters 3.3 – 3.6), highlighting the reproducibility of this approach.

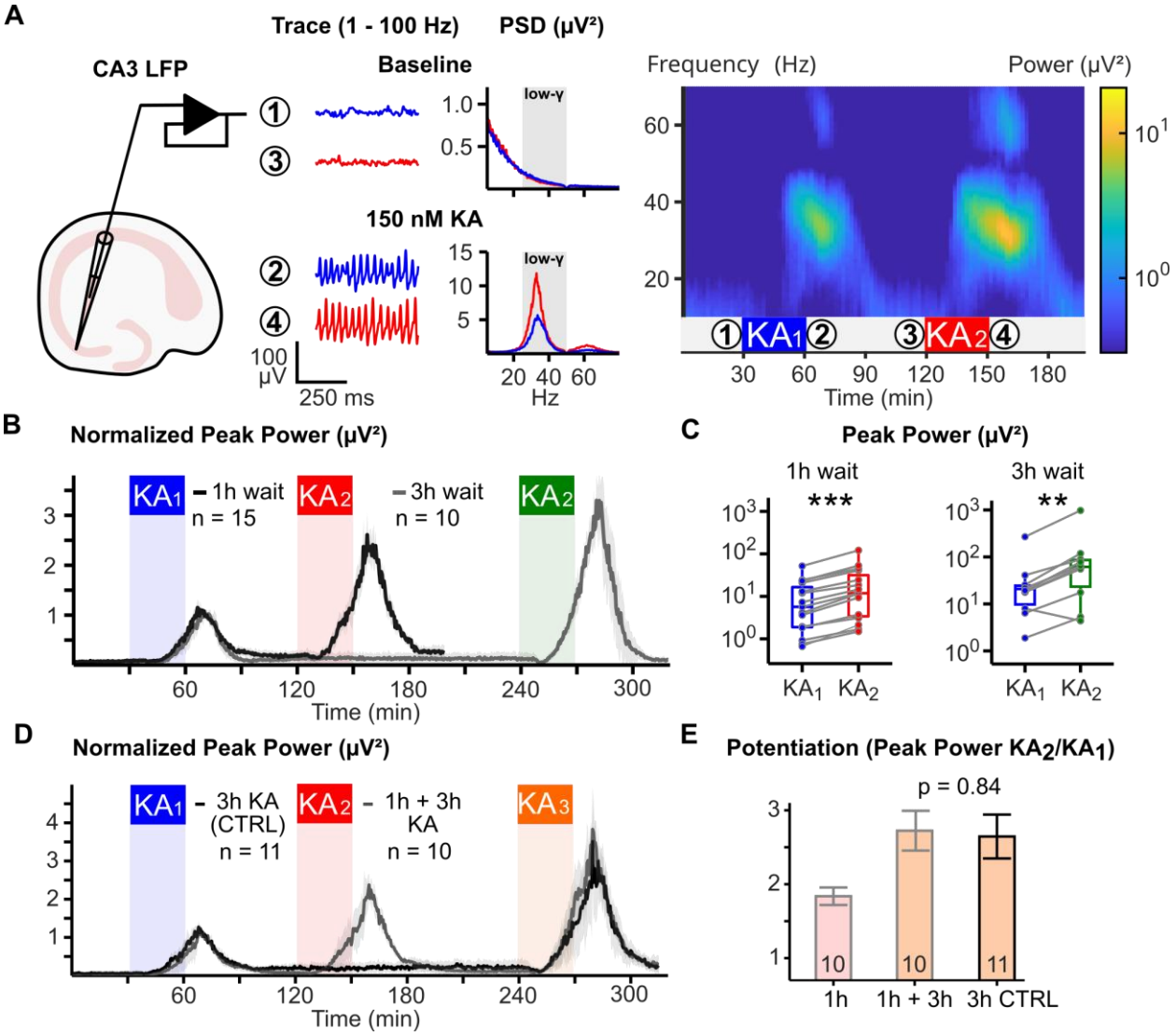

Figure 6: Gamma-potentiation in mouse CA3.

*(A) Left: Schematic of a local field potential (LFP) recording of the CA3 subregion in a hippocampal brain slice. Band-pass filtered traces (1 – 100 Hertz, Hz) and power spectral densities (PSD) before kainate (KA)-application ('Baseline'; 1 and 3) and during KA-induced gamma-oscillations ('150 nM KA'; 2 and 4). Right: Pseudocolor plot of the recording. KA_1 and KA_2 indicate the time periods of KA-application. (B) Time-Power plot of normalized peak power and 95% confidence interval (grey) for experiments with either 1- or 3-hour delay. (C) Boxplots of peak power in KA_1 and KA_2 with either 1- or 3-hour delay. ** and *** denote $p < 0.01$ and < 0.001 (Wilcoxon signed-rank test). (D) Same as (B) for experiments comparing KA re-application after a 1- and 3-hour delay (KA_3) versus control (CTRL) with after 3 hours. (E) Barplot of average gamma-power potentiation in (D). Error bars denote the standard error of the mean. P-value from a generalized linear model. N = number of slices tested. Adapted from Figures 1 and S2 in Hadler et al., 2024b.*

3.1.2 LFP-pMEA protocol for the analysis of unpaired samples

As in the paired LFP-protocol intervention (KA_1) and outcome (KA_2) were dependable, no definitive statement about the causality of gamma-potentiation could be made, warranting an alternative protocol to examine the effect of pre-conditioning during KA_1. This issue was addressed with pMEAs for the analysis of unpaired samples. To this purpose, gamma-oscillations were compared in pMEA recordings between naïve slices and those pre-treated during KA_1 in the LFP paradigm (Table 4; Figure 7):

- KA-application in pMEA-recordings induced gamma-oscillations at all electrodes covering the CA3 pyramidal cell layer.
- In each slice, gamma-power peaked at a specific electrode ("lead electrode") and decreased as a function of intralaminar distance.
- Slices pre-conditioned with KA in LFP-measurements displayed increased gamma-power in pMEA recordings compared to unconditioned slices. This applied to the lead electrode and sites up to 1 mm afar.

Therefore, gamma-potentiation is acquired by previous gamma-oscillations and expressed across the entire CA3 region. This protocol for the analysis of independent samples is revisited in Chapter 3.3.2 to elucidate the contribution of CP-AMPARs to gamma-potentiation.

Table 4: Summary of unpaired LFP-pMEA recordings.

Distance (µm)	Power KA_1 (µV²)	Power KA_2 (µV²)	n	p-Value (MWU)
0 (Lead)	8.14 [5.33; 13.16]	17.82 [15.84; 20.46]	11/11	1.53×10^{-3}
< 200	3.27 [2.34; 6.14]	9.43 [6.28; 14.26]	28/24	8.51×10^{-7}
200 – 400	3.19 [1.20; 4.51]	9.55 [6.34; 12.75]	28/28	2.29×10^{-8}
400 – 600	2.58 [0.84; 3.04]	6.45 [3.81; 8.49]	21/19	3.30×10^{-4}
600 – 800	1.66 [1.23; 2.88]	5.00 [2.75; 7.48]	15/18	3.30×10^{-4}
800 – 1000	1.71 [0.90; 2.28]	3.90 [3.00; 5.79]	7/14	2.27×10^{-3}

Data taken from Hadler et al., 2024b. n: number of electrodes tested, MWU: Mann-Whitney U-test; Lead: Lead electrode.

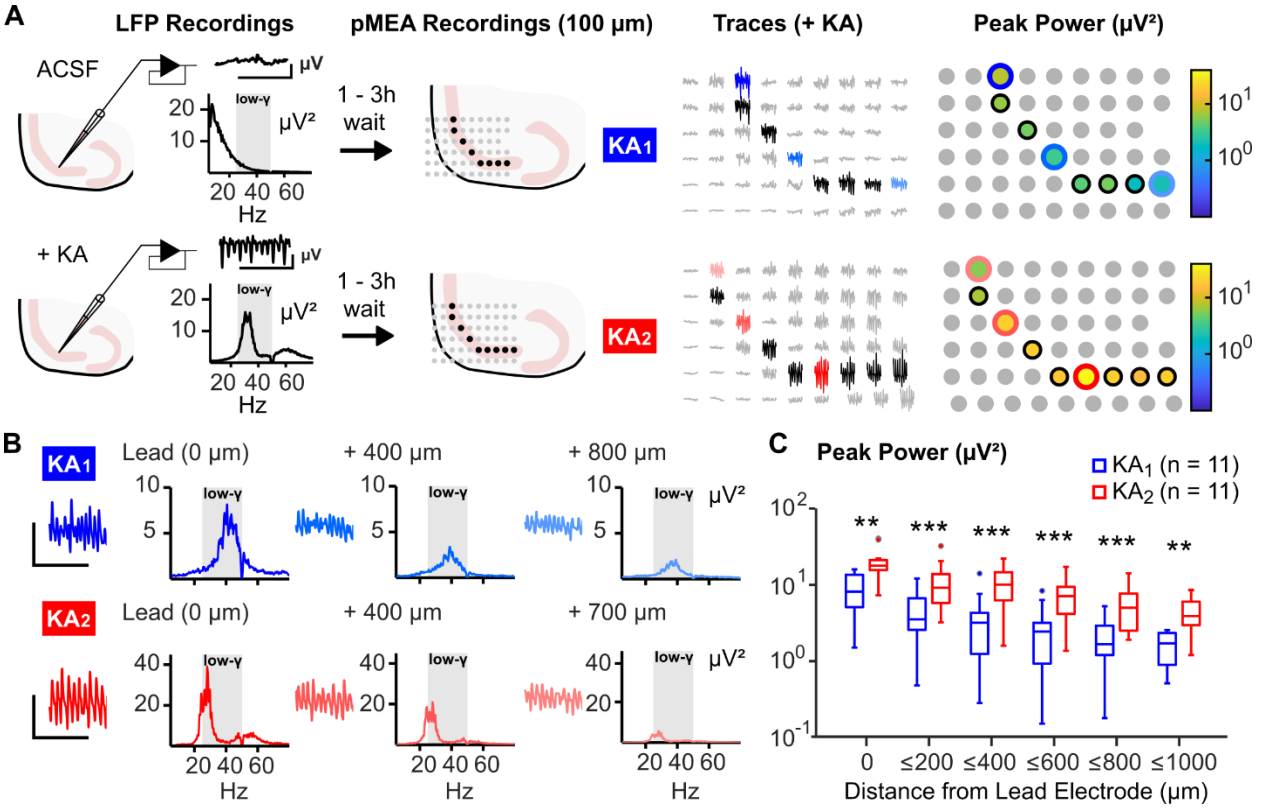

Figure 7: Gamma-potentiation of unpaired samples in LFP-pMEA recordings.

*(A) Left: In local field potential (LFP) recordings, slices are left to rest in artificial cerebrospinal fluid (ACSF) or treated with kainate (KA), yielding low-gamma activity. Slices are then transferred to perforated multi-electrode arrays (pMEAs) and electrodes selected covering CA3 (black). KA-application to untreated (KA_1, blue) and treated slices (KA_2, red) evokes gamma-activity. Right: Heatmaps of peak gamma-power. (B) Exemplary traces and power spectral densities (PSDs) taken from the experiments in (A). Recordings and PSDs from the electrode with the highest power ("Lead Electrode") are compared to distant sites, illustrating a decrease of peak power over distance. (C) Boxplots of peak power in both conditions (n = 11 slices tested each) pooled over the intralaminar distance from the lead electrode of each slice. Peak power is increased at all recording sites in treated slices (Mann-Whitney U-test, ** and *** denote $p < 0.01$ and < 0.001). Adapted from Figure 3 in Hadler et al., 2024b.*

3.2 Gamma-potentiation in CA1

In a first mechanistic intervention, gamma-potentiation was analyzed under consideration of hippocampal slice cytoarchitecture:

- Slow gamma-oscillations (30 – 50 Hz) originate in the CA3 subregion (Pietersen et al., 2014). Here, pyramidal neurons form reciprocal connections with other pyramidal neurons (PYR-PYR synapses) and interneurons (PYR-IN synapses).
- Gamma-oscillations generated in CA3 recruit pyramidal neuron and interneuron populations in CA1 via the Schaffer collaterals. The resulting CA1 slow gamma-oscillations (30 – 50 Hz) resonate with the upstream CA3 rhythm (Pietersen et al., 2014).
- In CA1, PYR-PYR synapses are nearly absent (Yang et al., 2014), and connectivity is dominated by PYR-IN synapses. Isolated stimulation of CA1 in CA1 Mini-slices generates mid-gamma oscillations [50 – 65 Hz, (Pietersen et al., 2014)].

Following this, the necessity of PYR-PYR synapses versus PYR-IN synapses for gamma-potentiation was investigated in intact hippocampal slices and CA1 Mini-slices (Figure 8):

- In LFP recordings of CA1 in intact slices, gamma-potentiation was confirmed for CA3 and CA1 low-gamma oscillations (Figure 8A).
- In CA1 Mini-slices, an adjusted protocol (2 x 400 nM KA) reproduced the roughly two-fold power increase (Peak Power KA_1: 1.94 [1.16; 5.55] μV^2 vs. KA_2: 4.44 [2.04; 10.03] μV^2; n = 13 slices; WSR, $p = 2.0 \times 10^{-4}$) for mid-gamma oscillations (Figure 8B).

Plasticity at the PYR-PYR synapse is therefore not required for the induction and expression of hippocampal gamma-potentiation. In the following, interventions at the PYR-IN synapse are explored within the framework of the CA3 model.

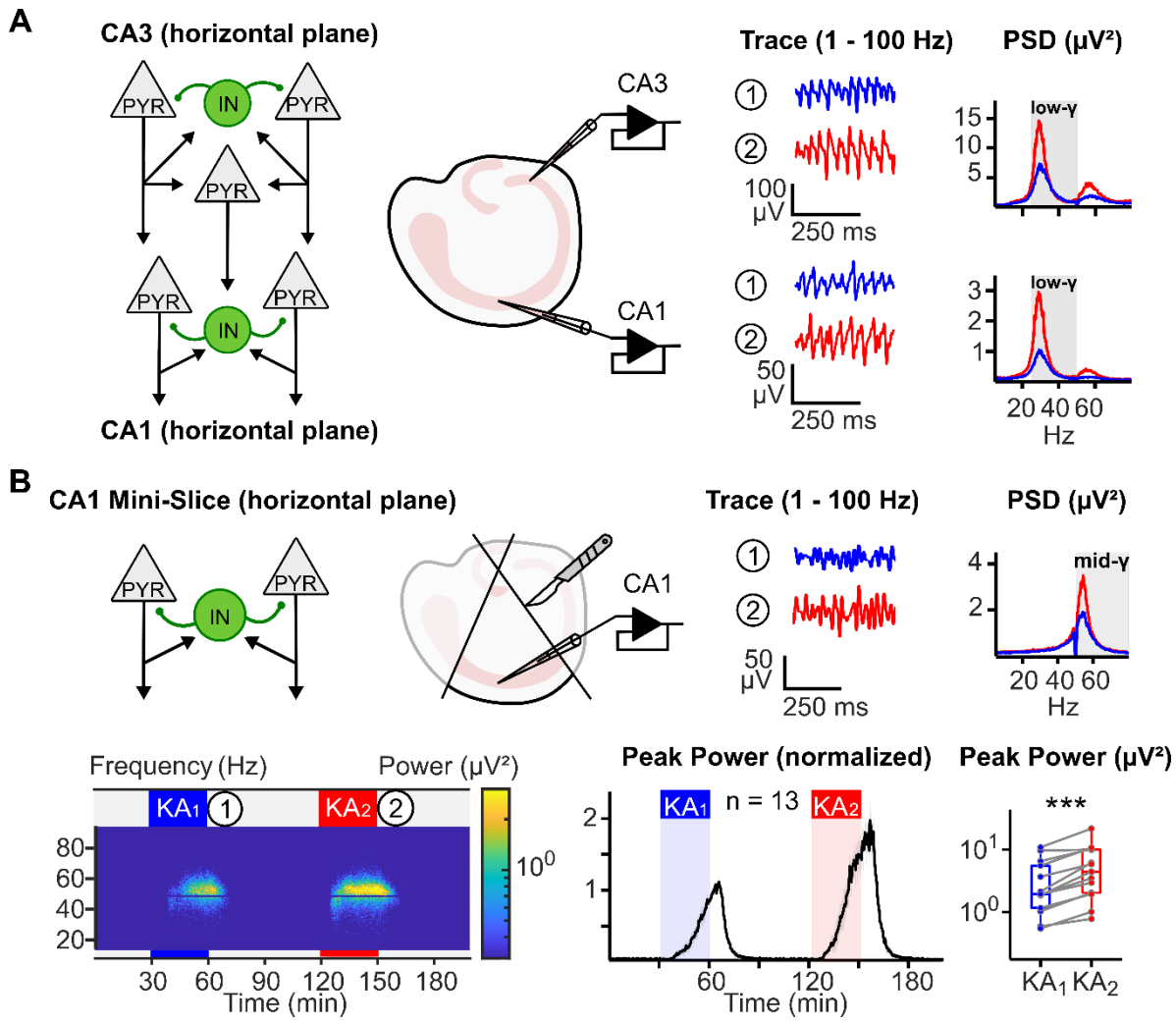

Figure 8: Gamma-potentiation in CA1 intact and Mini-slices.

*(A) Left: Schematic of the horizontal CA3-CA1 microcircuit. CA3 pyramidal neurons (PYRs) are interconnected amongst each other and with interneurons (INs) and target CA1 PYRs and INs via the Schaffer collateral pathway. Recording pipettes are placed in CA3 and CA1. Right: Traces and power spectral densities (PSDs) from an exemplary recording demonstrating gamma-potentiation of low-gamma activity (grey inset, "low-γ", 25 – 50 Hertz [Hz]) in CA1 concomitant to CA3. (B) Above: Schematic of the CA1 Mini-slice microcircuit. PYRs are interconnected with INs, but not amongst themselves. Schematic of the cuts separating CA1 from the subiculum and CA3. A recording pipette is placed in CA1. Exemplary traces and PSDs during KA_1 and KA_2 in a CA1-Mini slice, corresponding to the pseudocolor plot below. Grey inset "mid-γ" indicates 50 – 80 Hz. Below: Pseudocolor plot, Time-Power plot, and boxplot of peak power as in Figure 6 for CA1-Mini slices. *** denotes $p < 0.001$ (Wilcoxon Signed-Rank test). Adapted from Figure S3 in Hadler et al., 2024b.*

3.3 Synaptic mechanisms of gamma-potentiation

PYR-IN synapses differ from PYR-PYR synapses in their expression of iGluRs, characterized by an abundance of CP-AMPARs (Chapter 1.2). This was addressed by applying pharmacology to the paired LFP-protocol:

- D-AP5 (50 µM), an NMDAR-antagonist
- GYKI-53655 (50 µM), an unspecific AMPAR-antagonist
- NASPM (100 µM), an antagonist of CP-AMPARs
- UBP-302 (5 µM), an antagonist of the interneuron-specific KAR subunit GluK1

3.3.1 Identification of synaptic mechanisms in paired samples in CA3

Pharmacological blockade of iGluRs yielded the following profile of gamma-potentiation (Figure 9):

1. NMDARs are neither essential for the generation of gamma-oscillations nor required for gamma-potentiation (Figure 2 in Hadler et al., 2024b).
2. Under blockade of AMPARs, KA-application generates network oscillations, albeit at lower frequencies (10 – 15 Hz). The resulting oscillations are generated by NMDARs (Figure 2 in Hadler et al., 2024b), but do not undergo potentiation ([GYKI-53655] Peak Power KA_1: 1.43 [0.90; 9.22] µV² vs. KA_2: 3.89 [1.20; 14.21] µV², n = 9 slices; WSR, p = 0.09).
3. The selective blockade of CP-AMPARs mirrors global AMPAR blockade: KA-induced network oscillations peak at slower frequencies (20 – 25 Hz) and do not express potentiation ([NASPM] Peak Power KA_1: 16.57 [14.27; 18.52] µV² vs. KA_2: 15.20 [13.79; 19.52] µV², n = 9 slices; WSR, p = 1.0).
4. Blockade of GluK1 raises the threshold for KA-induced oscillations (400 nM) but does not influence the expression of gamma-potentiation (Figure S5 in Hadler et al., 2024b).

The contributions of GluK1 and CP-AMPARs to the generation of gamma-oscillations in CA3 – a region comprising PYR-PYR and PYR-IN synapses – underscore the mechanistic importance of excitation onto interneurons. The specific necessity of CP-AMPARs for long-term gamma-potentiation complements the cytoarchitectural argument from 3.1.2 at the synaptic level: CP-AMPAR-containing synapses (PYR-IN) are sufficient and required for the induction of network plasticity.

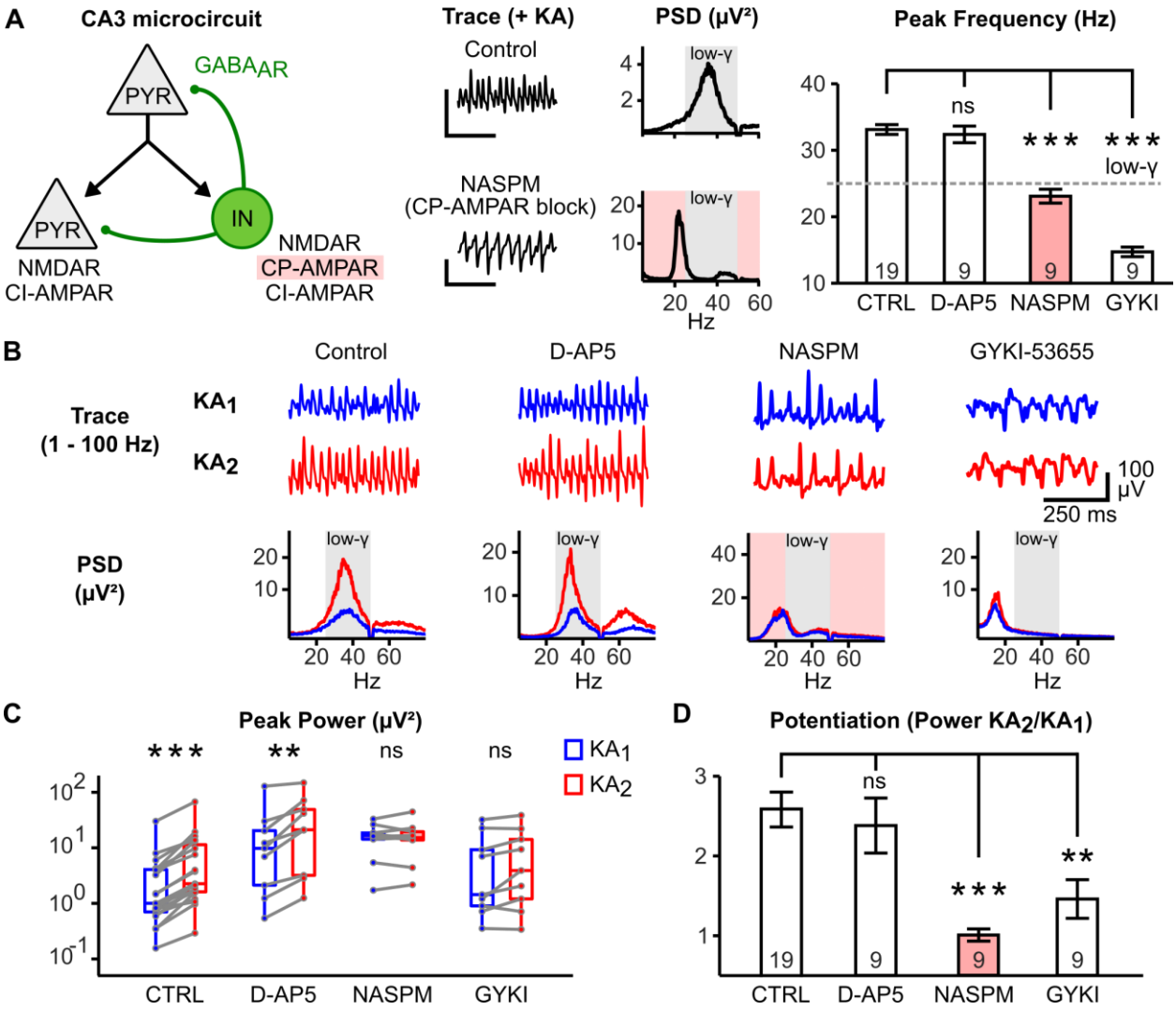

Figure 9: Ionotropic glutamate receptors mediating gamma-potentiation.

*(A) CA3 schematic with pyramidal neuron (PYR) and interneuron (IN) connections. PYR-IN synapses express NMDA receptors (NMDARs), calcium-permeable (CP-AMPARs; pink highlight), and calcium-impermeable AMPA receptors (CI-AMPARs). Blocking CP-AMPARs with naphthyl-spermine (NASPM) or all AMPARs with GYKI-53655 (GYKI) during kainate (KA)-application decreases peak frequencies below gamma-frequencies (low-γ; 25 – 50 Hertz, Hz). NMDAR-blockade with D-amino-5-phosphonopentanoate (D-AP5) does not affect peak frequency. Ns and *** denote $p > 0.05$ and $p < 0.001$ (generalized linear model). (B) Exemplary traces and power spectral densities (PSDs) during KA_1 and KA_2. (C) Peak power. ***, ** and ns denote $p < 0.001$, $p < 0.01$ and $p > 0.05$ (Wilcoxon Signed-Rank test). (D) Potentiation. Error bars denote the standard error of the mean. ***, ** and ns denote $p < 0.001$, $p < 0.01$ and $p > 0.05$ (generalized linear model). Numbers in barplots indicate number of slices. Adapted from Figure 2 in Hadler et al., 2024b.*

3.3.2 CP-AMPARs mediate network plasticity in unpaired samples

If CP-AMPARs contribute to both the generation of gamma-oscillations during KA_1 and the expression of potentiation during KA_2, an issue emerges similar to that of dependent samples in Chapter 3.1. Does CP-AMPAR blockade prevent potentiation of network oscillations because it:

1. … prevents the induction of plasticity?
2. … is necessary for the expression of potentiation?

Chapter 3.3.1 provides evidence toward the first question. Using the unpaired LFP-pMEA protocol from Chapter 3.1.2 addressed the second question (Figure 10):

- Pre-incubation with NASPM decelerated network oscillations (18 – 23 Hz) under KA-application in conditioned and unconditioned slices in pMEA recordings.
- Unlike control experiments (Chapter 3.1.2), peak power at the lead electrode remained unchanged between conditioned and unconditioned slices ([Control] Lead Electrode Peak Power KA_1: 8.14 [5.33; 13.16] μV^2 vs. KA_2: 17.82 [15.84; 20.46] μV^2, n = 11 slices; WSR, $p = 7.65 \times 10^{-4}$; [NASPM] Lead Electrode Peak Power KA_1: 17.34 [8.86; 20.79] μV^2 vs. KA_2: 7.93 [4.15; 15.88] μV^2, n = 11 slices; WSR, p = 0.11).

CP-AMPARs are thus necessary for the increase of power triggered by gamma-oscillations. This supports the conclusions from 3.2 and 3.3.1 on the interneuronal origin of gamma-potentiation and motivates a more in-depth, cell-type-specific analysis.

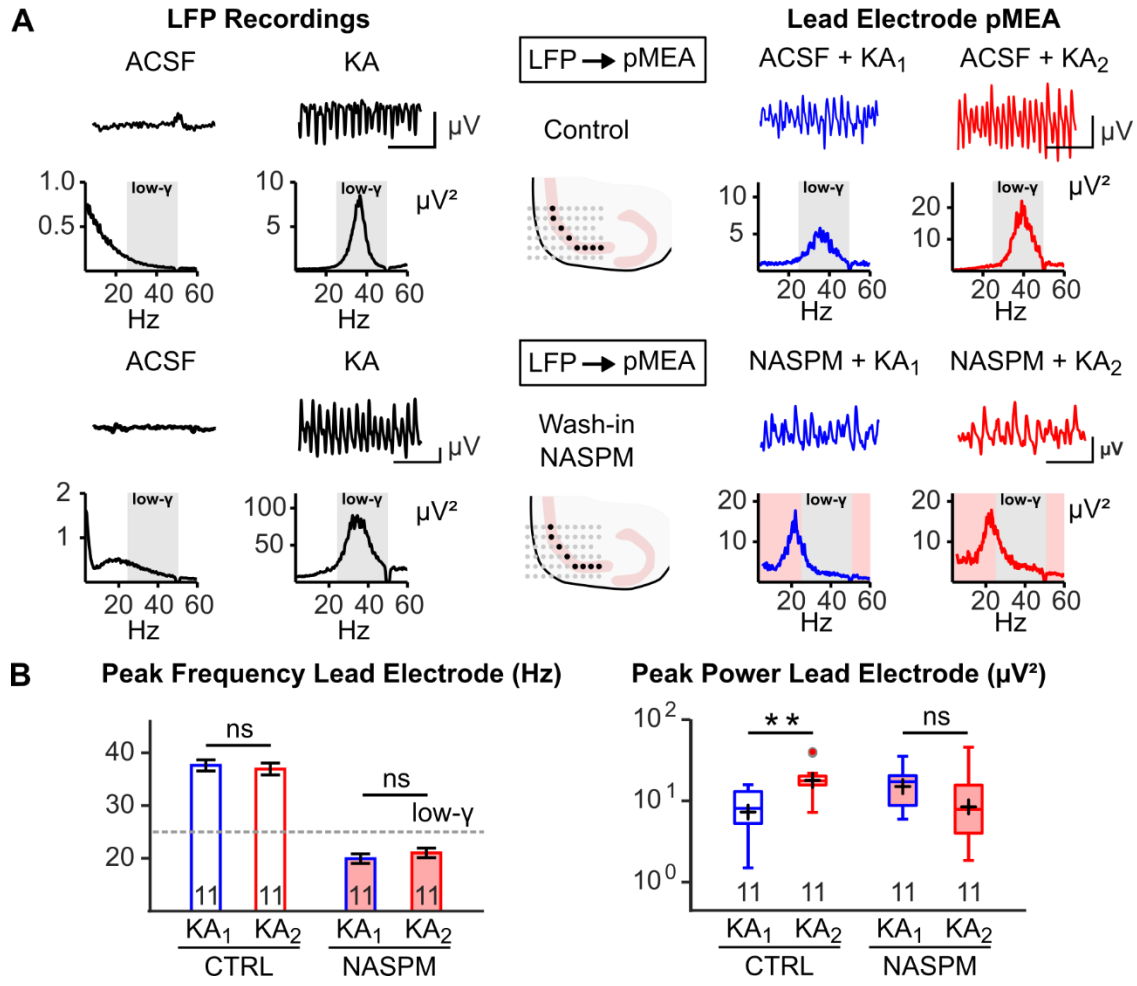

Figure 10: Calcium-permeable AMPA receptors express gamma-potentiation.

*(A) Simplified schematic of the local field potential (LFP)–perforated multi-electrode array (pMEA) approach from Figure 7. In LFP recordings, slices were either treated with kainate (KA) or not (artificial cerebrospinal fluid; ACSF) and subsequently transferred to pMEAs in control (CTRL) conditions or under bath-application of napthyl-spermine (NASPM). KA-induced oscillations were subsequently evoked and detected at the lead electrode in un-treated (KA_1) and treated (KA_2) slices. (B) NASPM decelerates KA-induced oscillations below gamma-frequencies (low-γ) in pMEA-recordings independent of pre-treatment. Changes in peak power observed in CTRL are absent in the presence of NASPM. ** and ns denote $p < 0.01$ and $p > 0.05$ (Mann-Whitney U-test). Error bars in barplots denote the standard error of the mean. Numbers in plots denote n = number of slices. Adapted from Figure 3 in Hadler et al., 2024b.*

3.4 The pharmacological profile of gamma-potentiation corresponds to established rules of PVI plasticity.

Chapters 3.2 and 3.3 suggested a mechanism of gamma-potentiation based on the potentiation of a predominantly CP-AMPAR-containing synapse. The highest density of CP-AMPARs is found in PVIs (Chapter 1.2.1) – therefore, PVI-LTP may underlie gamma-potentiation (Chapter 1.4). This is explored in the following under consideration of established mechanisms of PVI-LTP.

3.4.1 Gamma-potentiation in PV-mGluR5 mutants

PVI-LTP requires mGluR5-activation (Hainmüller et al., 2014). In slices from mice undergoing PVI-specific postnatal ablation of mGluR5 [PV-mGluR5, Chapter 2.1; (Barnes et al., 2015)], gamma-potentiation was quantified in LFP-recordings from two perspectives:

1. Influence of mGluR5 ablation: Comparison between wild-type (PV-mGluR5 WT) and mutant (PV-mGluR5 KO).
2. Influence of pharmacological mGluR5-blockade in both genotypes with MPEP (10 µM).

Figure 11 summarizes the results:

- MPEP application reduces the average magnitude of gamma-potentiation in PV-mGluR5 WT slices by roughly 50% ([WT Control] Potentiation: 2.31 +/- 0.22, n = 16 vs. [WT + MPEP] 1.49 +/- 0.13, n = 19; GLM, $p = 6.7 \times 10^{-3}$).
- The average magnitude of gamma-potentiation is reduced by 50% in PV-mGluR5 KO slices compared to WT slices ([KO Control] Potentiation: 1.53 +/- 0.11, n = 28; GLM, $p = 6.7 \times 10^{-3}$ vs. WT Control).
- Additional MPEP application did not affect the magnitude of gamma-potentiation in PV-mGluR5 KO slices ([KO + MPEP] Potentiation: 1.48 +/- 0.13, n = 19; GLM, p = 1 vs. KO Control).

mGluR5 activation thus represents a cell-type specific criterion for gamma-potentiation, relying on its expression in PVIs but explaining only 50% of overall potentiation. This warranted a more detailed pharmacological investigation of other potential signaling pathways.

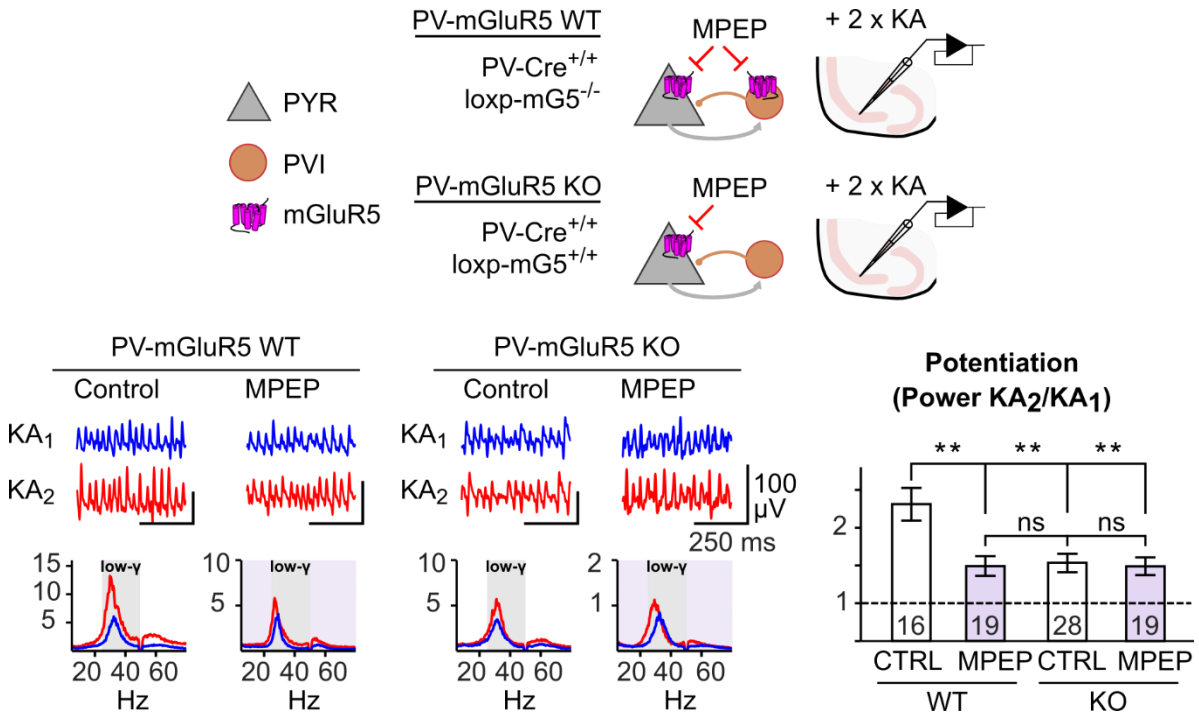

Figure 11: Metabotropic glutamate receptor 5 contributes to gamma-potentiation via parvalbumin interneurons.

*Above: Schematic of the experimental approach. In PV-mGluR5 WT animals, metabotropic glutamate receptor 5 (mGluR5) is expressed in pyramidal neurons (PYRs) and parvalbumin interneurons (PVIs). In PV-mGluR5 KO mutants, mGluR5 is not expressed in PVIs. 2-Methyl-6-(phenylethynyl)pyridine hydrochloride (MPEP) blocks mGluR5 in both models. Slices from both animals are tested under two-time application of kainate (KA). Below: Exemplary traces and power spectral densities of all conditions during KA_1 and KA_2. MPEP reduces the magnitude of potentiation in WT slices by approximately 50%. In KO slices, potentiation is already attenuated with no additional effect of MPEP. Error bars denote the standard error of the mean. ** and ns denote $p < 0.01$ and $p > 0.05$ (generalized linear model). Number of slices tested in barplots. Adapted from Figure 5 in Hadler et al., 2024b.*

3.4.2 Contributions of mGluR1, PKC und PKA towards gamma-potentiation

Other signaling molecules were considered suitable candidates for gamma-potentiation:

- mGluR1: Blockade by JNJ-16259685 (0.3 µM).
- PKC: Blockade by GF 109203X (3 µM).
- Protein Kinase A (PKA): Blockade by H-89 (3 µM).
- Voltage-gated calcium channels (VGCCs): Blockade of L- or T-Typ VGCCs by nifedipine (10 µM) and ML-218 (5 µM), respectively.

In slices from wild-type animals, pre-incubation with the respective antagonists resulted in the following (Figure 12):

- Pharmacological blockade of mGluR1 by JNJ-16259685 reduced the magnitude of gamma-potentiation by roughly 50% ([Control] Potentiation: 2.13 +/- 0.18, n = 15 vs. [JNJ-16259685] 1.44 +/- 0.12, n = 16; GLM, $p = 8.1 \times 10^{-3}$). Co-application of JNJ-16259685 and MPEP prevented the expression of gamma-potentiation ([MPEP + JNJ-16259685] Potentiation: 1.13 +/- 0.07, n = 23).
- Blockade of PKC by GF 109203X or PKA by H-89 prevented the expression of gamma-potentiation ([Control] Potentiation: 1.91 +/- 0.12, n = 24; [GF 109203X] 1.20 +/- 0.08, n = 20; [H-89] 1.18 +/- 0.07, n = 25).
- Blockade of L- or T-Type VGCCs had no influence on gamma-potentiation ([Control] Potentiation: 2.16 +/- 0.22, n = 8; [Nifedipine] 2.20 +/- 0.25, n = 6; [ML-218] 1.92 +/- 0.22, n = 6).

This global pharmacological profile completes the results from 3.4.1 regarding mechanisms of gamma-potentiation: In addition to the PVI-specific expression of mGluR5, activation of mGluR1 is required, which recruits PKC in line with a canonical Gq-signaling pathway. An additional prerequisite is given in the recruitment of PKA, but not VGCCs. This profile is nearly identical to previous knowledge of PVI plasticity (Kullmann and Lamsa, 2007; Tzilivaki et al., 2023).

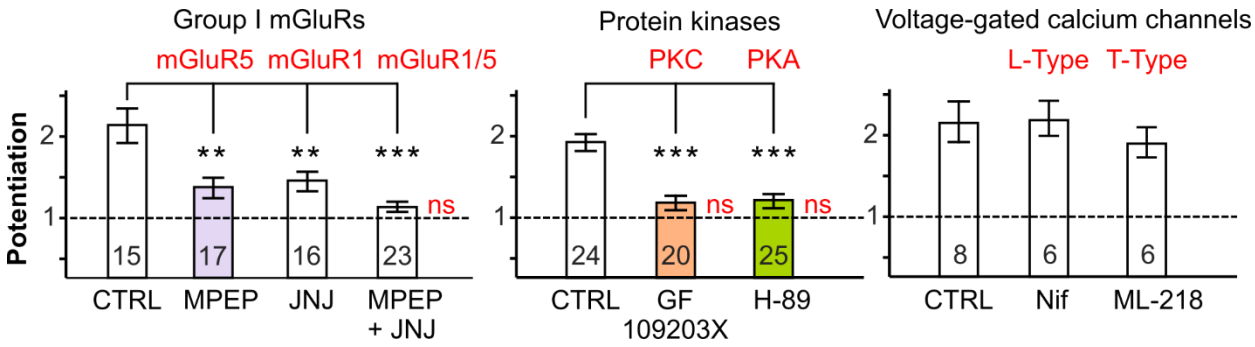

Figure 12: Gamma-potentiation requires group I metabotropic glutamate receptors, protein kinase C and protein kinase A.

*Summary of experiments in wild-type slices under pharmacological blockade of group I metabotropic glutamate receptors (mGluRs), protein kinases and voltage-gated calcium channels (VGCCs). Blockers of mGluR5 [2-Methyl-6-(phenylethynyl)pyridine hydrochloride (MPEP)], mGluR1 [JNJ-16259685 (JNJ)], protein kinase C (PKC; GF 109203X), protein kinase A (PKA; H-89), L-Type VGCCs [nifedipine (Nif)] and T-Type VGCCs (ML-218) were compared to control (CTRL) conditions. Error bars denote the standard error of the mean. *** and ** denote $p < 0.001$ and $p < 0.01$ (generalized linear model). Red ns denotes $p > 0.05$ for KA_1 versus KA_2 values (Wilcoxon Signed Rank test). Number of slices tested in barplots. Adapted from Figure 5 in Hadler et al., 2024b.*

3.5 PVI neuromodulation bidirectionally gates gamma-potentiation

Chapter 3.4.2 demonstrated a pharmacological profile of gamma-potentiation reminiscent of mechanisms governing PVI-LTP yet leaving two questions unanswered:

1. Is the effect of PKA blockade localized to PVIs?
2. Can the mGluR1 component be explained by its activation on PVIs?

These questions were addressed in brain slices from mice expressing one of two chemogenetic receptors of the DREADD class [Designer Receptor Exclusively Activated by Designer Drugs, (Roth, 2016)] in PVIs:

- hM3Dq: Based on the human M3 receptor, activation of which triggers a Gq-signaling pathway, activating PKC.
- hM4Di: Based on the human M4 receptor, activation of which triggers a Gi-signaling pathway, inactivating PKA.

In slices from PV-Ai9-hM3Dq and PV-Ai9-hM4Di animals (Chapter 2.1), the respective receptor was activated by bath application of DCZ, (Nagai et al., 2020). Testing both variants allowed bidirectional manipulation of PVIs in the context of gamma-potentiation.

3.5.1 PV-Ai9-hM4Di experiments

Slices from PV-Ai9-hM4Di mice were tested in LFP-recordings (Chapter 3.1.1) with and without continuous bath application of DCZ (3 µM). As a methodological control, the same experiment was conducted in slices from animals not co-expressing hM4Di (PV-Ai9, Chapter 2.1). The results are summarized in Figure 13:

- The initial induction of KA-induced gamma-oscillations was unaffected by DCZ and between genotypes.
- DCZ prevented the expression of gamma-potentiation in slices from PV-Ai9-hM4Di mutants ([PV-Ai9-hM4Di Control] Potentiation: 2.37 +/- 0.22, n = 15 vs. [PV-Ai9-hM4Di + DCZ] 1.09 +/- 0.10, n = 15; GLM, $p = 3.4 \times 10^{-5}$).
- In slices from PV-Ai9 control animals, the magnitude of gamma-potentiation remained unchanged with DCZ ([PV-Ai9 Control] Potentiation: 2.24 +/- 0.23, n = 13 vs. [PV-Ai9 + DCZ] 2.25 +/- 0.23, n = 13; GLM, p = 1).

Therefore, Gi-signaling in PVIs is sufficient to prevent gamma-potentiation, providing a cellular explanation for the PKA component observed in Chapter 3.4.2.

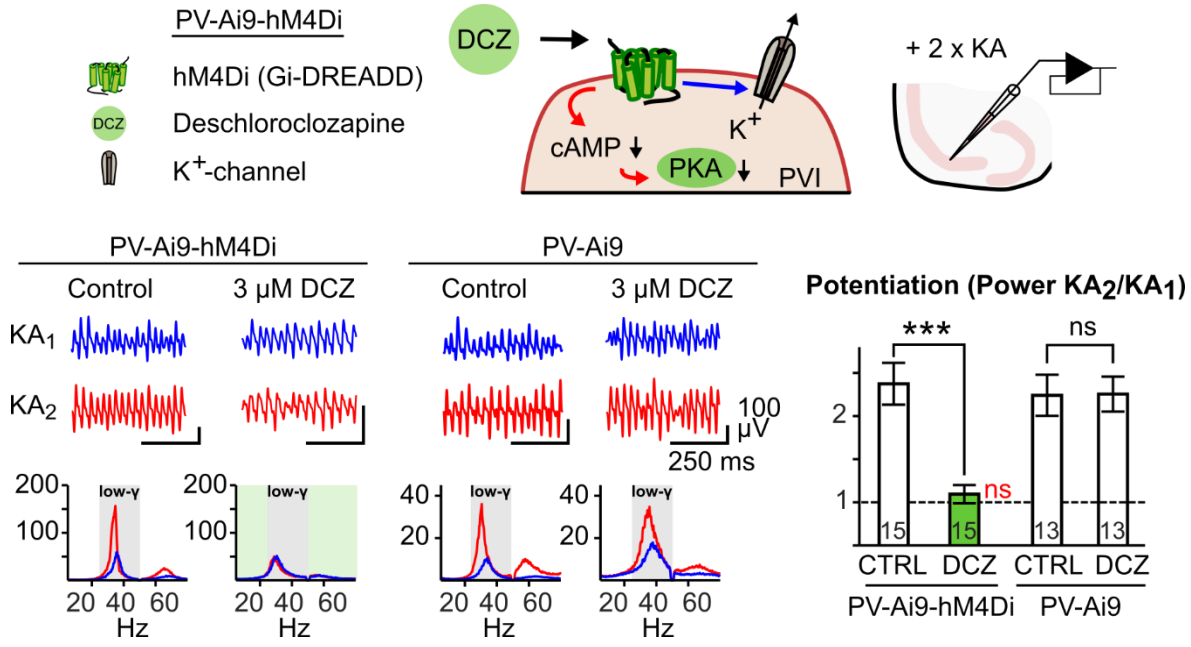

Figure 13: hM4Di-activation in parvalbumin interneurons prevents gamma-potentiation.

*Above: Schematic of PV-Ai9-hM4Di approach. Deschloroclozapine (DCZ) stimulates a parvalbumin interneuron (PVI)-specific cascade, reducing intracellular cyclic adenosine-mono-phosphate (cAMP) levels and protein kinase A (PKA) activity. The activation of potassium (K+) channels hyperpolarizes the PVI. PV-Ai9-hM4Di slices are screened for gamma-potentiation by two-time application of kainate (KA) in local field potential recordings. Below: Exemplary traces and power spectral densities from PV-Ai9-hM4Di slices and control PV-Ai9 slices with and without 3 µM DCZ (DCZ-application in PV-Ai9-hM4Di highlighted in green). DCZ-application prevents gamma-potentiation in PV-Ai9-hM4Di slices, but not in PV-Ai9 controls. Error bars denote the standard error of the mean. *** and ns denote $p < 0.001$ and $p > 0.05$ (generalized linear model). Red ns denotes $p > 0.05$ for KA_1 versus KA_2 values (Wilcoxon Signed Rank test). Number of slices tested in barplots. Adapted from Figure 6 in Hadler et al., 2024b.*

3.5.2 PV-Ai9-hM3Dq experiments

Gq-receptors (mGluR1 and mGluR5) mediate the complete expression of gamma-potentiation (Chapter 3.4), but the origin of mGluR1 activation remained unexplained. Accordingly, an approach to re-induce gamma potentiation was chosen in slices from PV-Ai9-hM3Dq animals:

- Since the mGluR5-component is mediated by PVIs, activation of hM3Dq in PVIs may restore this following pharmacological blockade with MPEP (10 µM).
- If the mGluR1-component is also mediated by PVIs, activation of hM3Dq in PVIs should restore the magnitude of gamma-potentiation entirely upon co-application of MPEP and JNJ-16259685 (0.3 µM).
- Should hM3Dq activation trigger a canonical Gq-pathway, pharmacological blockade of PKC (GF 109203X; 3 µM) should prevent the above.

The results are summarized in Figure 14:

- Gamma-potentiation was prevented in slices from PV-Ai9-hM3Dq animals following pharmacological blockade of mGluR5 and mGluR1 ([PV-Ai9-hM3Dq Control] Potentiation: 2.31 +/- 0.23, n = 14 vs. [PV-Ai9-hM3Dq + MPEP + JNJ-16259685] 1.10 +/- 0.12, n = 12; GLM, $p = 7.0 \times 10^{-5}$) or PKC (([PV-Ai9-hM3Dq Control] Potentiation: 1.93 +/- 0.22, n = 8 vs. [PV-Ai9-hM3Dq + GF 109203X] 0.86 +/- 0.08, n = 11; GLM, $p = 1.9 \times 10^{-5}$).
- Co-application of DCZ (3 µM) with MPEP and JNJ-16259685 during KA_1 and KA_2 fully restored the magnitude of gamma-potentiation compared to the DCZ-naive control ([PV-Ai9-hM3Dq + MPEP + JNJ-16259685 + DCZ] 2.32 +/- 0.24, n = 13; GLM, $p = 7.0 \times 10^{-5}$ vs. PV-Ai9-hM3Dq + MPEP + JNJ-16259685).
- Blockade of PKC with GF 109203X prevented the DCZ-mediated restoration of gamma-potentiation ([PV-Ai9-hM3Dq + GF 109203X + DCZ] 1.04 +/- 0.10, n = 11; GLM, p = 0.35 vs. PV-Ai9-hM3Dq + GF 109203X).

In summary, gamma-potentiation can be triggered by the activation of PVI-specific Gq-signaling pathway targeting PKC, providing a cellular basis for the mGluR1-component described in Chapter 3.4.2. This completes the cellular profile of gamma-potentiation, whereby molecular determinants in PVIs determine subsequent plasticity of network gamma-oscillations.

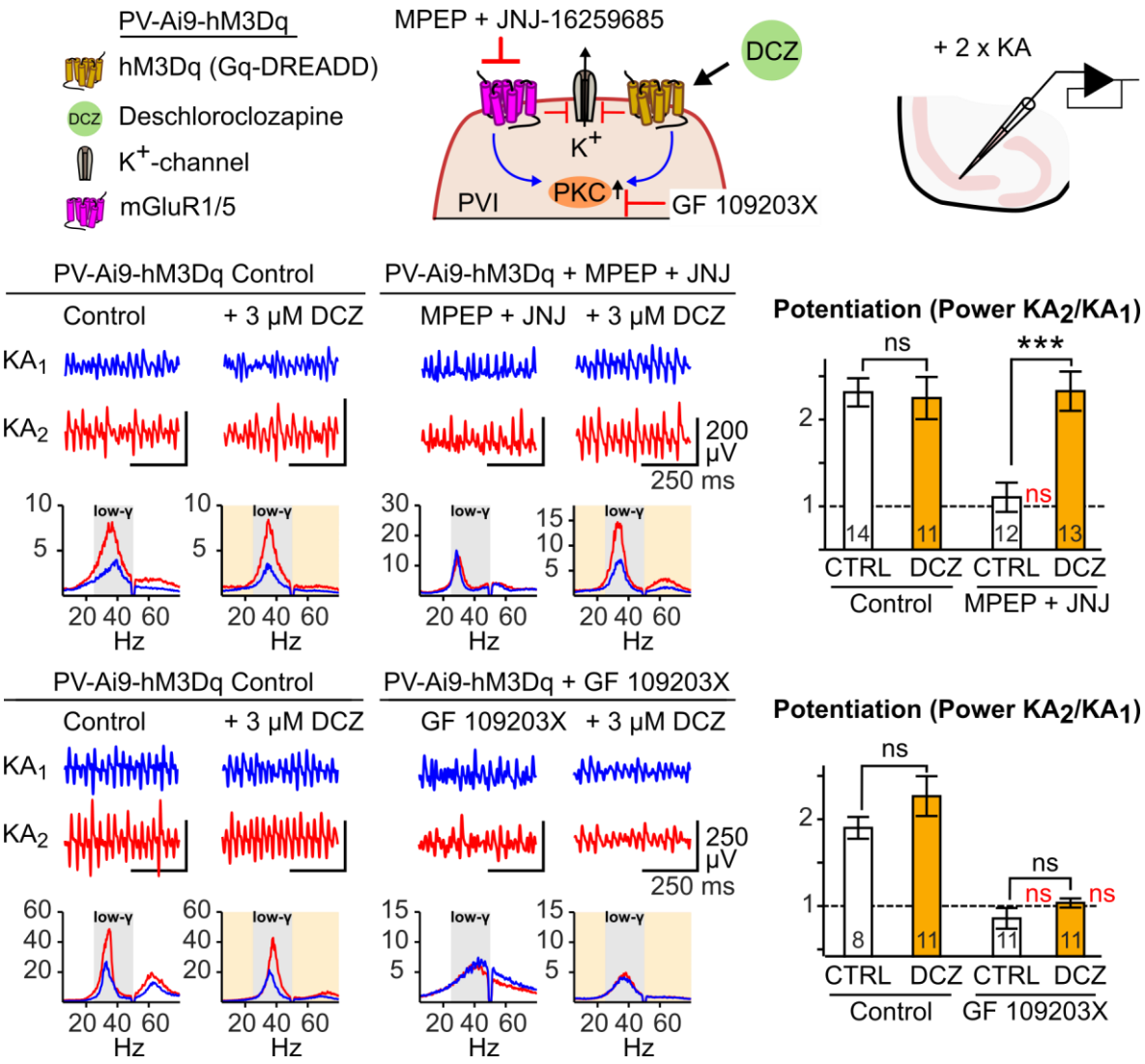

Figure 14: hM3Dq-activation in parvalbumin interneurons gates gamma-potentiation dependent on protein kinase C.

*Above: Schematic of PV-Ai9-hM3Dq approach. Deschloroclozapine (DCZ) stimulates protein kinase C (PKC) activity in parvalbumin interneurons (PVI) and blocks potassium (K+)-channels. Blockade of metabotropic glutamate receptors 1 and 5 (mGluR1/5) with MPEP and JNJ-16259685 (JNJ) or PKC with GF 109203X. PV-Ai9-hM3Dq slices are screened for gamma-potentiation by two-time application of kainate (KA) in local field potential recordings. Below: Exemplary traces and power spectral densities from PV-Ai9-hM3Dq slices with or without DCZ (yellow) under mGluR1/5- or PKC blockade. DCZ rescues gamma-potentiation after mGluR1/5-, but not PKC-blockade. Error bars denote the standard error of the mean. *** and ns denote $p < 0.001$ and $p > 0.05$ (generalized linear model). Red ns: $p > 0.05$ for KA_1 versus KA_2 values (Wilcoxon Signed Rank test). Number of slices in barplots. Adapted from Figure 6 in Hadler et al., 2024b.*

4 Discussion

4.1 Summary

1. The induction of ex vivo gamma-oscillations durably increases network excitability, manifested as an increase of subsequent gamma-oscillation spectral amplitude, "gamma-potentiation" (Chapter 3.1; Figure 15).
2. At the microcircuit level, a reciprocal network of pyramidal neurons and interneurons (PYR-IN) is sufficient for the expression of gamma-potentiation (Chapter 3.2).
3. The expression of gamma-potentiation requires CP-AMPARs, the dominant glutamate receptor at the PVI input synapse (Chapter 3.3).

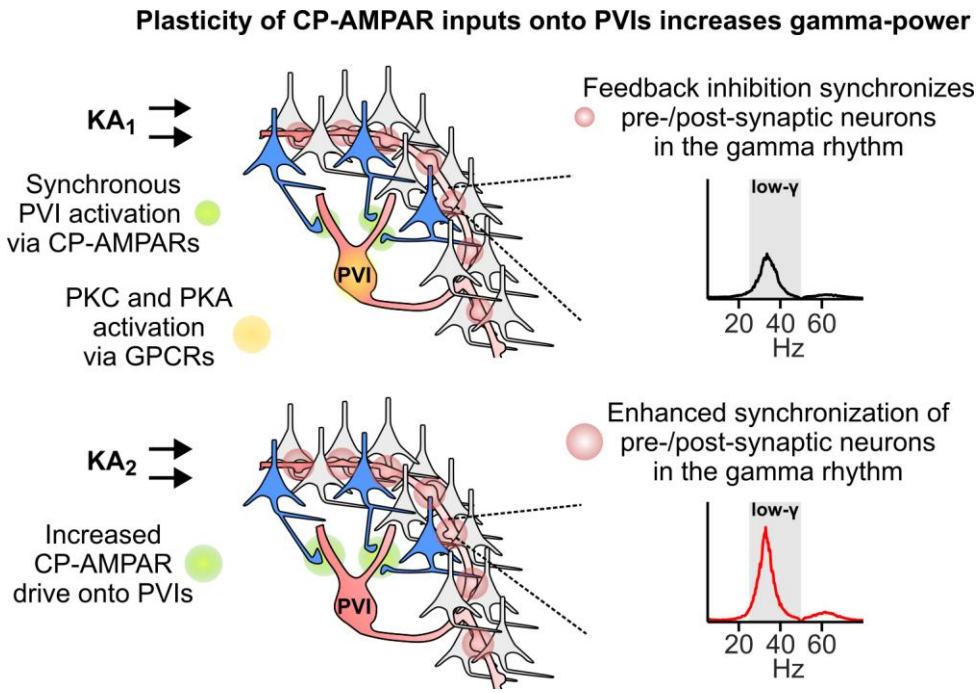

Figure 15: Synaptic mechanisms of gamma-potentiation.

Above: The first induction period with kainate (KA_1) drives parvalbumin interneurons (PVI) via calcium-permeable AMPA receptors (CP-AMPARs, green highlight) and enables the synchronization in the gamma rhythm (red highlight). The activation of protein kinase C (PKC) and protein kinase A (PKA) via G-protein coupled receptors (GPCRs) gates the emergence of plasticity (yellow highlight). Below: During the second induction period (KA_2), CP-AMPAR inputs to PVIs are increased (green highlight), leading to enhanced oscillations (red highlight). Own illustration.

4. The induction of gamma-potentiation is mediated by metabotropic signaling in PVIs, specifically the activation of mGluR5 and mGluR1 at the receptor level and the subsequent recruitment of PKC and PKA as effectors (Chapters 3.4 and 3.5).
5. The activation of DREADD-signaling pathways in PVIs gates the expression of gamma-potentiation (Chapter 3.5; Figure 16).

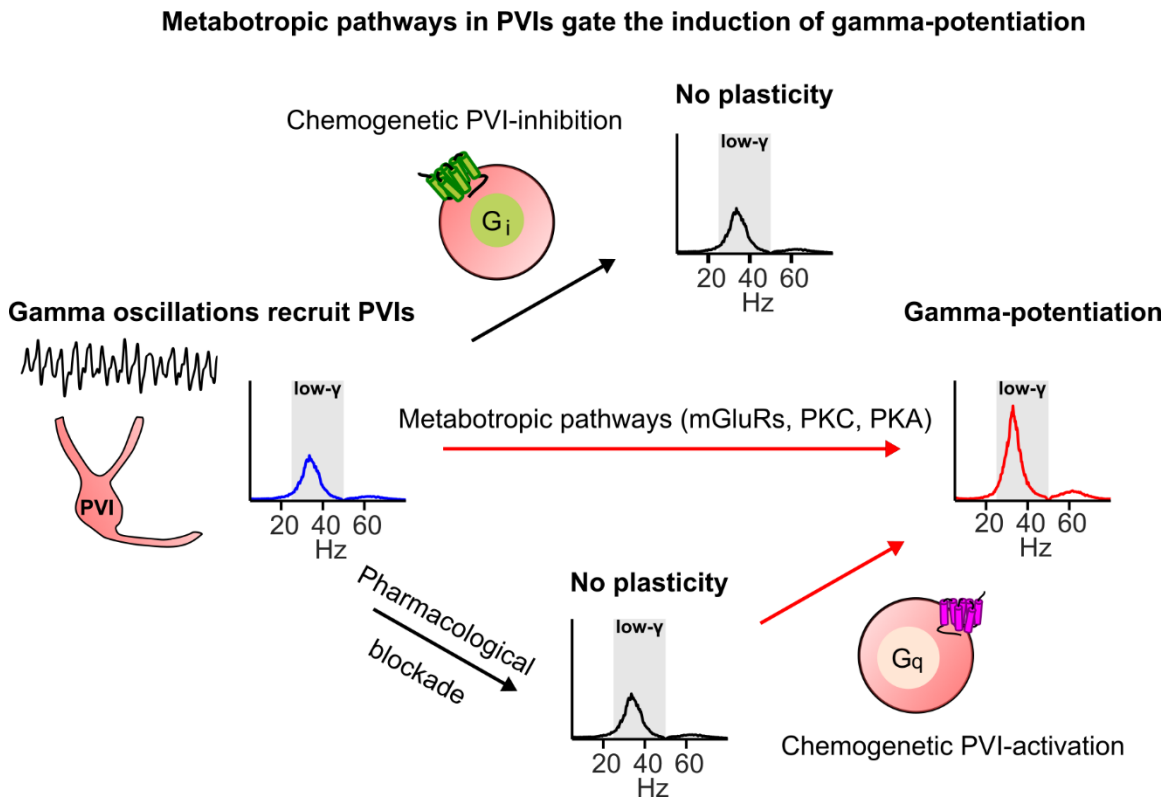

Figure 16: Metabotropic pathways gating gamma-potentiation.

Schematic illustrating the pharmacological and molecular approaches gating the induction of gamma-potentiation. During gamma-oscillations, parvalbumin interneurons (PVIs) are recruited in an activity-dependent matter. The activation of innate metabotropic pathways, including metabotropic glutamate receptors (mGluRs), protein kinase C (PKC) and protein kinase A (PKA), mediates gamma-potentiation. Chemogenetically inhibiting PVIs and activating a Gi-cascade prevents gamma-potentiation (above), as does pharmacological blockade of the innate pathways (below). In the latter case, chemogenetic activation of PVIs via a Gq-cascade reinstates gamma-potentiation. Own illustration.

4.2 Supporting in silico findings in Hadler et al., 2024b by collaborators

In collaboration with Alexandra Tzilivaki (ORCID: 0000-0003-0140-2864), an in silico network model of CA3 was designed to support the experimental results from Chapters 3.1 and 3.2. These chapters suggested gamma-potentiation required CP-AMPARs but did not sufficiently demonstrate that increased CP-AMPAR recruitment at the PYR-PVI synapse causes gamma-potentiation. Since gamma-oscillations induce LTP at both the PYR-PYR and PYR-PVI synapses (Zarnadze et al., 2016), two alternative hypotheses remained:

1. Gamma-potentiation is triggered by LTP at the PYR-PYR synapse. Since the blockade of CP-AMPARs suppresses the generation of the gamma-rhythm (Chapter 3.3) the expression of potentiation may be indirectly masked.
2. Gamma-potentiation is mediated at the PYR-IN synapse, but the enhanced transmission at this synapse originates heterosynaptically at the upstream PYR-PYR synapse rather than homosynaptically at the PYR-IN synapse.

In a network model comprising 20 pyramidal neurons and 2 PVIs, extracellularly measured gamma-oscillations were induced by activation of the pyramidal neurons. In repetitions of the simulations, either the CI-AMPAR conductance at the PYR-PYR synapse (PYR-LTP), the CP-AMPAR conductance at the PYR-PVI synapse (PVI-LTP), or both synapses (PYR+PVI-LTP) was selectively increased, and the resulting power was quantified [Figure 4 in Hadler et al., 2024b]:

- PYR+PVI-LTP reproduced the power increase of ex vivo gamma-potentiation.
- The isolated induction of PYR-LTP led to a subtle increase of gamma-oscillation power, inferior to the PYR+PVI-LTP condition.
- The isolated induction of PVI-LTP resulted in a power increase significantly superior to PYR-LTP and equivalent to PYR+PVI-LTP.

This additional inductive approach confirmed the conclusions from Chapters 3.2 and 3.3, indicating that gamma-potentiation can be entirely explained by an increased conductance at the CP-AMPAR-containing PVI input synapse and significantly enhanced the conclusions of the ex vivo findings.

4.3 Current state of research

Gamma-oscillations as a local network phenomenon were first described in the late 1980s (Gray et al., 1989; Gray & Singer, 1989). Since then, research on this phenomenon has focused on three overarching themes:

1. The mechanistic understanding of gamma-oscillation generation, particularly its cellular foundations (Chapter 1.2).
2. The predictive value of detecting or inducing gamma-oscillations for cognitive performance (Chapter 1.1.1 & 1.1.2).
3. Investigating disrupted gamma-oscillations as a symptom of neuropsychiatric disorders (Chapter 1.1.3).

It is noteworthy that, herein, gamma-oscillations are viewed as static phenomena, whose properties adapt over long-term processes, i.e. during postnatal development or the gradual onset of neurodegenerative diseases. However, recent studies reaffirm the notion that gamma-oscillations are subjected to spectral changes within minutes following learning (Chapter 1.1.3), yet a mechanistic understanding hereof on the cellular and synaptic levels remained elusive.

The significant contribution of this study lies in describing and mechanistically characterizing a short- to mid-term plasticity phenomenon inert to gamma-oscillations, “gamma-potentiation”, which is reciprocally linked to PVI-LTP (discussed by Craig et al., 2024). The following will delve into previous knowledge on PVI-LTP and neuronal oscillations, which form the basis for the interaction described here between the cellular and network levels.

4.3.1 Mechanisms of PVI-LTP

PVI-LTP was initially described in the DG in paired recordings and following extracellular electrical stimulation (Alle et al., 2001), which has become the default paradigm for subsequent investigations (Lamsa et al., 2007; Hainmüller et al., 2014; He et al., 2021). It is noteworthy that these paradigms exclusively apply stimulation frequencies within the gamma-frequency range (30–100 Hz). Upon stimulation, a postsynaptic metabotropic signaling cascade is recruited involving group I mGluRs, PKC, and a PVI-specific gamma-variant of the calmodulin-dependent kinase (gamma-CaMKII). Through the adjustment of

two parameters, PVI-LTP facilitates the synaptic recruitment of PVIs (Kullmann and Lamsa, 2007; Tzilivaki et al., 2023):

1. Increase of CP-AMPAR conductance.
2. Reduction of voltage-gated potassium channels of the Kv1 class, thereby promoting action potential frequencies in the gamma-range.

This study replicates this profile and transfers it to the broader level of network oscillations: Mechanisms mediating PVI-LTP also mediate a power increase of gamma-oscillations. In this context, the CP-AMPAR-expressing PVI input synapse is the essential functional structure (Chapter 3.3). This aligns with previous reports highlighting the specific contribution of intact CP-AMPARs on PVIs to generating synchronous gamma-oscillations (Fuchs et al., 2001, 2007), and suggesting a connection between PVI-LTP and subsequent gamma-power in vivo (He et al., 2021), though without identifying the mechanism described here (previous gamma-oscillations and metabotropic signaling in PVIs).

4.3.2 Cell-to-network plasticity: Implications for memory processes

Power increases of neuronal oscillations accompany successful memory processes (Chapter 1.1.2). This has been extensively studied in the context of hippocampal learning in rodents: Object-based learning precedes increases of gamma-power in CA3 and pyramidal neuron coupling to ongoing gamma-oscillations (Tort et al., 2009; Fernández-Ruiz et al., 2021), CFC induces power increases of CA1 theta-, gamma- and ripple-oscillations – effects that require the activation of PVIs (He et al., 2021; Ognjanovski et al., 2017; Xia et al., 2017). This work demonstrates that, in the case of gamma-oscillations, power increases can have a cell-type specific, synaptic origin: PVI-LTP. The transfer of cellular plasticity to the expression of network oscillations (*cell-to-network plasticity*) provides a mechanistic framework supporting the understanding of memory processes (Figure 17; discussed in Hadler et al., 2024a):

Upon memory acquisition (e.g. novel object exploration or CFC), groups of neurons synchronize their activities in the gamma-rhythm, forming functional neuronal ensembles (Fernández-Ruiz et al., 2021). The gamma-induced STDP amongst pyramidal neurons and PVIs (Zarnadze et al., 2016) putatively strengthens the synaptic connections between ensemble neurons, leading to their facilitated reactivation in later periods. This is accompanied by increases of theta- and gamma-oscillation power (Ognjanovski et al.,

2017; He et al., 2021; Hadler et al., 2024b), particularly during subsequent sleep, a functionally vulnerable period of memory consolidation (Karunakaran et al., 2016; Ognjanovski et al., 2018). During this period, the increased amplitude of oscillations strengthens the coupling of ensemble neurons to the ongoing oscillation (Fernández-Ruiz et al., 2021) as well as the functional connectivity amongst themselves (Ognjanovski et al., 2017). Thereby, by refining the specificity of a memory's neuronal representation, it can be stored as a long-lasting neuronal *engram* (Raven and Aton, 2021; Hadler et al, 2024a).

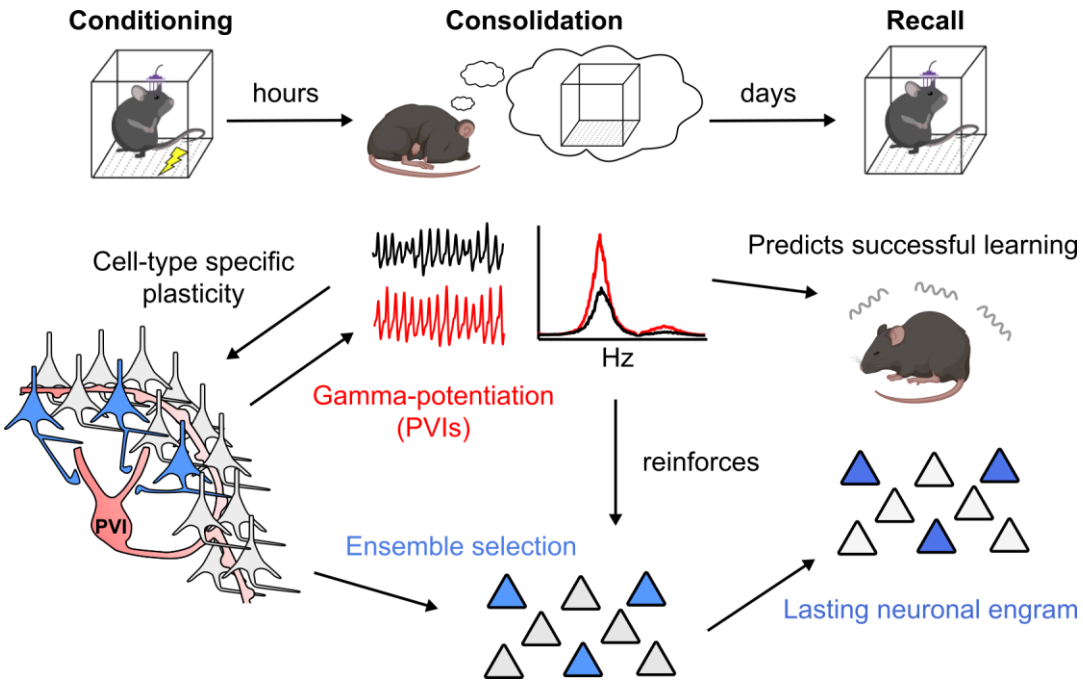

Figure 17: Cell-to-network plasticity underlying memory processes.

Above: Timeline of contextual fear conditioning in mice. In the hours following conditioning (electric shock), the memory of the conditioned context (cage) is consolidated during the next sleep epoch and is recalled in the following days. Below: Proposed mechanisms supporting memory consolidation on the cellular and network level. Upon conditioning, pyramidal neurons (grey) and parvalbumin interneurons (PVI, red) synchronize their activities (black field potential trace) and select a subset of ensemble pyramidal neurons (blue). The induction of cell-type specific plasticity strengthens the neuronal ensemble and induces gamma-potentiation (red field potential trace) via PVIs. During consolidation, enhanced gamma-oscillations reinforce the neuronal ensemble's specificity. This predicts the successful recall of the memory, illustrated by freezing behaviour, and is represented on the neuronal level by the formation of a lasting neuronal engram. Adapted from Figure 5 in He et al. (2021), Figure 1 in Hadler et al. (2024a) and images from BioRender.com

In line with the conclusions of this study, the success of memory formation is impaired by depriving PVIs of metabotropic stimuli and oscillations supporting PVI-LTP: This includes the genetic ablation of mGluR5 (Chapter 3.4.1; Barnes et al., 2015) or gamma-CaMKII (He et al., 2021) as well as the artificial activation of Gi-signaling via hM4Di (Ognjanovski et al., 2017; Xia et al., 2017), successfully used here to prevent gamma-potentiation (Chapter 3.5.1). Conversely, memory deficits can be reinstated by either the artificial induction of network theta- or gamma-oscillations (Ognjanovski et al., 2018; Li et al., 2022) or Gq-signaling in PVIs via hM3Dq-activation (Marissal et al., 2018), which in this study is sufficient to reinstate gamma-potentiation (Chapter 3.5.2).

In summary, a possible physiological function of gamma-potentiation lies in the optimized coordination of neuronal ensembles during memory consolidation. Crucial for this is the gamma-activity dependent induction of PVI-LTP and its subsequent transfer to the network level of gamma-oscillations.

4.4 Limitations

4.4.1 KA-induced gamma-oscillations

In this study, a controlled, reproducible ex vivo protocol was developed to reliably quantify gamma-potentiation (see Chapter 3.1.1). However, experiments were exclusively performed in the KA-model of gamma-oscillations, which presents a methodological bias: KARs are expressed on both pyramidal neurons and interneurons and contribute to synaptic plasticity processes in CA3 (Petrovic et al., 2017), which may influence gamma-potentiation.

This bias was partially addressed (Chapter 3.3.1) by examining the interneuron-specific KAR subtype GluK1 (Cossart et al., 1998). The GluK2 subtype, primarily expressed on pyramidal neurons, is necessary for the generation of KA-induced gamma-oscillations (Fisahn, 2004) and could not be ruled out as a source of interference. However, because the profile of gamma-potentiation can be explained entirely by PVI plasticity, the involvement of such a pathway is unlikely.

Alternative pharmacological induction strategies of gamma-oscillations ex vivo include (Bartos et al., 2007):

- The M1 receptor agonist Carbachol (Fisahn et al., 1998) or a combination of acetylcholine and the cholinesterase inhibitor physostigmine.
- The mGluR agonist (RS)-3,5-dihydroxyphenylglycine (Whittington et al., 1995)

Due to the unreliable onset and washout dynamics of both strategies, as well as their inert activation of Gq-cascades, these approaches were not pursued in this study.

In addition to pharmacological strategies for inducing gamma-oscillations, models based on focal electrical stimulation (Fuchs et al., 2001) or optogenetic excitation of PVIs (Sohal et al., 2009) exist. At the time of data collection, these methods were not available.

4.4.2 Comparison to in vivo neuronal oscillations

The results of this study were exclusively obtained ex vivo and have limited relevance for the physiologically occurring gamma-rhythm in vivo. The following lists similarities and differences between the ex vivo and in vivo models, which ultimately justify the motivation for the ex vivo approach of this work:

- Origin of hippocampal gamma-oscillations: In vivo, hippocampal gamma-oscillations rarely occur in isolation, being modulated by oscillations in the EC (Fernández-Ruiz et al., 2021). Under such circumstances, it cannot be assessed whether plasticity processes between local neurons have a significant impact on the local gamma-rhythm.
- Spatial detection of gamma-oscillations: In vivo, oscillations projected from the EC synchronize selective portions of the hippocampus (Fernández-Ruiz et al., 2021), leading to a selection bias at the recording site and potentially distorting plasticity measurements. In contrast, the global application of KA in the presented model triggers a global activation of the hippocampus, which was detected extensively in pMEA measurements.
- The CA3 region as an independent generator of gamma-oscillations: An exception to the influence of the EC is CA3, which autonomously generates gamma-oscillations in vivo (Bragin et al., 1995). The relationship between cellular organization and measured gamma-oscillations in CA3 is so constant that the spectral amplitude of KA-induced gamma-oscillations measured in acute slices positively correlates with the spectral amplitude previously measured in vivo in the same animal (Lu et al., 2011).

- Confounders of in vivo gamma-oscillations: In vivo, gamma-oscillations are modulated by physiologically occurring covariables, including other frequency spectra (especially theta-oscillations) and autonomic parameters such as the state of consciousness, running speed, or respiratory rate (Zheng et al., 2015; Zhong et al., 2017).

In summary, gamma-oscillations measured in acute slices represent at best an approximation of behavior at the cellular and network levels in vivo. Accordingly, future in vivo studies must focus on reproducing the postulated mechanisms and expression of gamma-potentiation. A significant advantage of the ex vivo method lies in the reproducibility of the approach, which was not feasible in vivo at the time of data collection.

4.4.3 Origin of PKA activation

It was previously unknown that PKA could be involved in synaptic plasticity processes of PVIs. On the contrary, an early study on PVI-LTP did not observe a contribution of PKA activation (Alle et al., 2001). Therefore, Chapters 3.4.2 and 3.5.1 report an unexpected partial finding. This raises the question of how PKA is recruited in acute slices during the induction of gamma-potentiation and which endogenous signaling pathways may be involved:

1. Canonical Gs-signaling pathway: Gs-coupled GPCRs in the hippocampus include dopamine receptors and norepinephrine-activated beta-adrenergic receptors. Inputs for both receptor classes originate from the locus coeruleus (LC), a region crucial for learning processes in CA3 (Wagatsuma et al., 2018). The extent to which severed LC fibers are active in acute hippocampal slices is unclear, but there is evidence for latent dopamine activity in acute brain slices (Edelmann and Lessmann, 2011).
2. Non-canonical Gq-signaling pathway (Chen et al., 2017): PKA has regulatory subunits that can be activated by endogenous Gq-cascades (e.g., by muscarinic or glutamatergic agonists). Since gamma-potentiation is based on a Gq-cascade, such an explanatory approach would be valid.

Ultimately, within the scope of this work, no definitive statement can be made about the origin of PKA activation beyond its localization on PVIs.

4.5 Implications for Clinical Practice and/or Future Research

The description of an intrinsic plasticity mechanism of gamma-oscillations, along with its cell-type-specific mechanistic profile, provides a deeper understanding of how disruptions of gamma-oscillations emerge and reveals new approaches for future interventions. These are summarized in Hadler et al. (2024a) and elaborated on in the following.

4.5.1 Deficits of PVI-mediated gamma-potentiation underlying memory deficits in AD and SCZ

AD and SCZ represent two highly prevalent, chronic neuropsychiatric diseases, which share a common burden of long-term memory deficits. Etiologically, AD and SCZ pathology varies between patient groups, including monogenetic causes, multifactorial causes, or neurodegeneration. These affect PVI function in different manners, as demonstrated in animal studies: For example, PVI-specific mutations of key signalling proteins implicated in SCZ such as mGluR5 (Barnes et al., 2015), T-Type VGCCs (Shen et al., 2021), or NMDARs (Korotkova et al., 2010) are independently sufficient to induce core behavioural features of SCZ in mice. Similarly, models of multifactorial causes in SCZ and neurodegeneration in AD present with deficiencies in PVI excitability, parvalbumin expression and myelination (Hijazi et al., 2023; McCutcheon et al., 2023). Ultimately, such interventions converge on reduced gamma-power as a common neurophysiological correlate capable of predicting deficiencies in memory testing (summarized in Hadler et al., 2024a).

Considering the presumptive role of gamma-potentiation in supporting synaptic plasticity (Chapter 1.3.1) and memory processes (Chapter 4.3.2), a line of argumentation can be drawn tying dysfunctions on the cellular and network levels to lasting cognitive deficiencies in AD and SCZ (Figure 18): Impaired PVI function results in their impaired synaptic recruitment following otherwise adequate external stimuli (e.g. visual cues in the Mooney Face Test), which can be observed on the network level as reduced gamma-power. The reduced level of synchronous GABAergic output leads to a loss of temporal fidelity in the pyramidal neuron population’s response, which fails to form a specific representation on the ensemble level (Chapter 1.1.1 & 4.3.1). The asynchronous co-activation of pyramidal neurons and PVIs thus adds to the innate, disease-associated impairments of PVI function and further decreases the probability of STDP at their synapses, impeding the induction of gamma-potentiation. Long-term memory consolidation, however, requires a period

of enhanced theta- and gamma-power obtained during learning and, in the case of gamma-oscillations, the specific induction of PVI-LTP (Chapter 4.3.2). Therefore, a lack of gamma-potentiation represents a possible bottleneck preventing successful long-term memory processes in diseases affecting PVI-function, such as AD and SCZ.

Such a model provides an important distinction between intermittent states of decreased gamma-power during cognitive processing (e.g. occasionally not recognizing a face in the Mooney Face test) and the vicious cycle of permanently deficient processing (e.g., memory impairments) or erroneous perception (e.g., sensory hallucinations) in patients. A PVI- specific, plasticity-based framework for the emergence of memory deficits may not

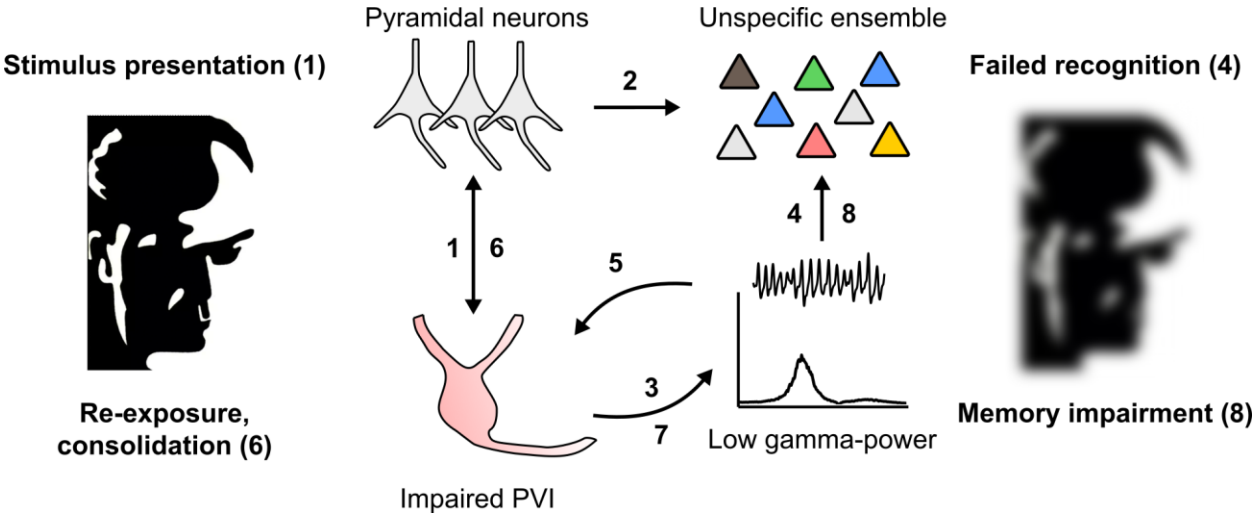

Figure 18: Lacking cell-to-network plasticity as a model of memory deficits.

Schematic of the vicious cycle of malfunctioning neuronal processing and cell-to-network plasticity underlying memory deficits. Upon presentation of an adequate stimulus (e.g., a Mooney Face card [Figure 2 in Uhlhaas and Singer, 2010]), pyramidal neurons insufficiently drive the parvalbumin interneuron (PVI) population due to disease-associated impairments (1), which fails to inhibit the pyramidal neurons, leading to unspecific ensemble selection (2) and reduced gamma-oscillations (3). These are insufficient to refine the ensemble, which fails to accurately represent the stimulus, precluding its correct recognition as a face (4). The failure to induce adequate gamma-activity and the PVI's innate impairments prevent the induction of PVI-LTP (5), leaving the deficient network unaltered. Upon re-exposure to the same image, intended for memory consolidation (6), the cycle of inadequate PVI activation (6), insufficient gamma-activity (7), and unspecific ensemble dynamics (8) begins anew, leading to an unsuccessful memory process. Own illustration.

only add to the understanding of AD and SCZ pathology, but also offers new avenues towards targeting these therapeutically.

4.5.2 Neuromodulation of PVIs as a target for the treatment of SCZ

Adding to observations of impaired PVI excitability (Chapter 4.5.1), deficits in neuromodulation, including the glutamatergic and dopaminergic systems (McCutcheon et al., 2023), are argued to contribute to SCZ pathology. Considering the relationship between memory deficits in SCZ and gamma-potentiation (Chapter 4.5.1) and the dependency of gamma-potentiation on metabotropic signalling (Chapters 3.4 and 3.5), targeting the specific neuromodulation of PVIs may serve as a promising therapeutic approach.

In this work, mGluR5 emerges as a suitable candidate for restoring aberrant gamma-oscillations – and, arguably, SCZ therapy. The "PV-mGluR5 KO" animal model utilized here exhibits disturbed gamma-potentiation (Chapter 3.4.1) and SCZ-like cognitive deficits (Barnes et al., 2015). In SCZ patients, mGluR5 is functionally impaired (Wang et al., 2020). Promisingly, preclinical studies show an antipsychotic effect following administration of positive allosteric modulators of mGluR5 (mGluR5-PAMs) in animal models of psychosis (Rook et al., 2015; Brown et al., 2023).

Particularly biased mGluR5-PAMs, selectively boosting the Gq-signalling pathway upon activation, show promise in improving cognitive performance with a low side-effect profile (Rook et al., 2015). In slices derived from phencyclidine (PCP)-treated rats, treatment with biased mGluR5-PAMs is sufficient to reinstate the power of ex vivo gamma-oscillations, providing a network correlate for improved cognitive performance (Brown et al., 2023). Similar to the experiments in Chapter 3.5.2 using PVI-specific hM3Dq-activation, this rescue is PKC-dependent. Therefore, it is conceivable that the effects of biased mGluR5-PAMs on gamma-oscillations and cognitive performance arise from reinstating gamma-potentiation by supporting PVI-LTP. The PVI-specificity of targeting Gq-pathways in SCZ is further supported by preclinical studies in animals models of chronic MK-801 treatment or the LgDel-mutation, in which selective activation of PVIs with hM3Dq is sufficient to restore gamma-oscillations and cognitive performance (Marissal et al., 2018; Huang et al., 2021). Further, additional hM3Dq-activation in PVIs outperforms sole treatment of PCP-treated mice with the common antipsychotic olanzapine (Arime et al., 2024), demonstrating its added benefit. Therefore, targeting Gq-signalling in PVIs may prove a

promising new target in SCZ, which can be evaluated on the network level by changes in gamma-oscillation power.

The "dopamine hypothesis" of SCZ locates the cause of positive and negative symptoms in the respective hyperactivity of the D2 receptor (positive symptoms, e.g., hallucinations) and/or hypoactivity of the D1 receptor (negative symptoms, e.g., affective blunting or memory impairments) in striato-cortical structures. Receptors of both classes are expressed on various cell types, including PVIs, and could influence gamma-potentiation. D1 and D2 receptors are coupled to Gs- and Gi-proteins, respectively, and influence the activity of PKA, which is essential for gamma-potentiation (Chapters 3.5.1 and 4.4.3). Chronic suppression of this cascade in PVIs via hM4Di (Chapter 3.5.1) induces SCZ-like states in mice (Huang et al., 2021), suggesting a PVI-centered interpretation of the dopamine hypothesis. The therapeutic potential inherent to this is compellingly confirmed in a study treating LgDel mice, in which D2R blockade or PVI activation are sufficient to rescue decreases of PVI protein expression profiles, disturbed gamma-oscillation power and cognitive deficits (Mukherjee et al., 2019).

In conclusion, the metabotropic profile of gamma-potentiation can be used as a model for the emergence of long-term aberrant gamma-oscillations in SCZ. Pharmacological and pharmacogenetic interventions targeting PVI-specific Gq- and Gs/i-signaling pathways already show high preclinical potential in the treatment of SCZ animal models and may exert their effects by supporting the induction of gamma-potentiation.

4.5.3 Gamma-induced plasticity of network oscillations as a guiding principle for future therapies

The previous chapters suggest a pathophysiological model of deficient gamma-potentiation with features of a vicious cycle: Reduced gamma-oscillations lead to reduced plasticity (Chapter 4.5.1), which is inadequately expressed due to impaired metabotropic signaling cascades (Chapter 4.5.2) - resulting in enduringly reduced gamma-oscillations and impeding memory processes. A possible strategy breaking through this cycle may lie in the imposed generation of oscillations by means of external stimulation.

To this point, optogenetic stimulation of PVIs at gamma-frequencies (40 Hz) has proven efficient to acutely alleviate cognitive impairments in animal models of AD and SCZ

(Chapter 1.1.3). The molecularly invasive approach underlying this currently remains unavailable to patients. Other, clinically feasible strategies may similarly engage PVIs, synchronize local neuronal populations at gamma-frequencies, and exert the same, procognitive effects. These include transcranial approaches by magnetic stimulation (repetitive transcranial magnetic stimulation; rTMS (Maiella et al., 2022)) or current application via EEG electrodes (transcranial electric stimulation; tES (Blanco-Duque et al., 2024)) and “gamma entrainment using sensory stimuli” (GENUS (Adaikkan and Tsai, 2020)), which applies visual or auditory cues at 40 Hz to awake subjects (Figure 19A). All approaches show promise in treating cognitive symptoms in AD and SCZ yet the underlying mechanisms are unknown and data on long-term efficacy remain sparse (summarized and discussed in Blanco-Duque et al., 2024, and Hadler et al., 2024a).

This study (Hadler et al., 2024b), alongside previous findings on gamma-induced plasticity (Zarnadze et al., 2016), predicts that approaches applying gamma-frequency stimulation (rTMS, tES, GENUS) may exert their effects on cognitive performance via the induction of neuronal plasticity, specifically of PVIs (discussed in Hadler et al., 2024a): PVIs have been shown to be recruited by gamma-frequency stimulation in rodents, with some studies demonstrating subsequent adaptations of their cellular properties, including increased excitability (Hoppenrath et al., 2016; Shen et al., 2021). Currently, this cannot be determined to occur in humans on the cellular level. However, findings demonstrating that gamma-stimulation can induce subsequent increases of gamma-power in healthy subjects and AD patients (Benussi et al., 2022; Maiella et al., 2022) are in line with the model of cell-to-network plasticity governing gamma-potentiation, as proposed in this study.

How may this be used to design new approaches in treating cognitive symptoms? Figure 19B illustrates a therapeutic strategy integrating the findings of this study with the clinical approaches presented here (Chapters 4.5.1 and 4.5.2): In states of impaired PVI function (Chapter 4.5.1), interactions between pyramidal neurons and PVIs are unlikely to generate adequate gamma-oscillations. By applying external stimulation to the network, e.g. via transcranial stimulation, the local neuronal network is entrained to co-activate at gamma-frequencies, increasing the likelihood of STDP. To overcome the limitations set by impaired PVI metabotropic functions (Chapter 4.5.2), pharmacological agents targeting PVI neuromodulation, e.g. biased mGluR5-PAMs, further decrease the induction threshold for PVI-LTP. By increasing the excitability of PVIs (Chapter 4.3.1), PVI-LTP sets

the stage for gamma-potentiation, enabling the network to generate an improved response to subsequent stimuli, as is necessary for physiological cognitive processes, such as the generation of memories (Chapter 4.3.2). Intriguingly, this model allows for the simultaneous, non-invasive monitoring of therapy success on the level of network gamma-oscillation power.

In summary, the findings of this study can be used beyond their immediate implications for cellular and network physiology. By merging them with preclinical and clinical findings on the pathophysiology of AD and SCZ, as well as therapeutic strategies applying gamma-frequency stimulation, a novel approach to treating and monitoring neuropsychiatric diseases may be at hand: The reinstatement of cognitive deficits by means of the physiological plasticity of gamma-oscillations via PVIs (discussed in Hadler et al., 2024a).

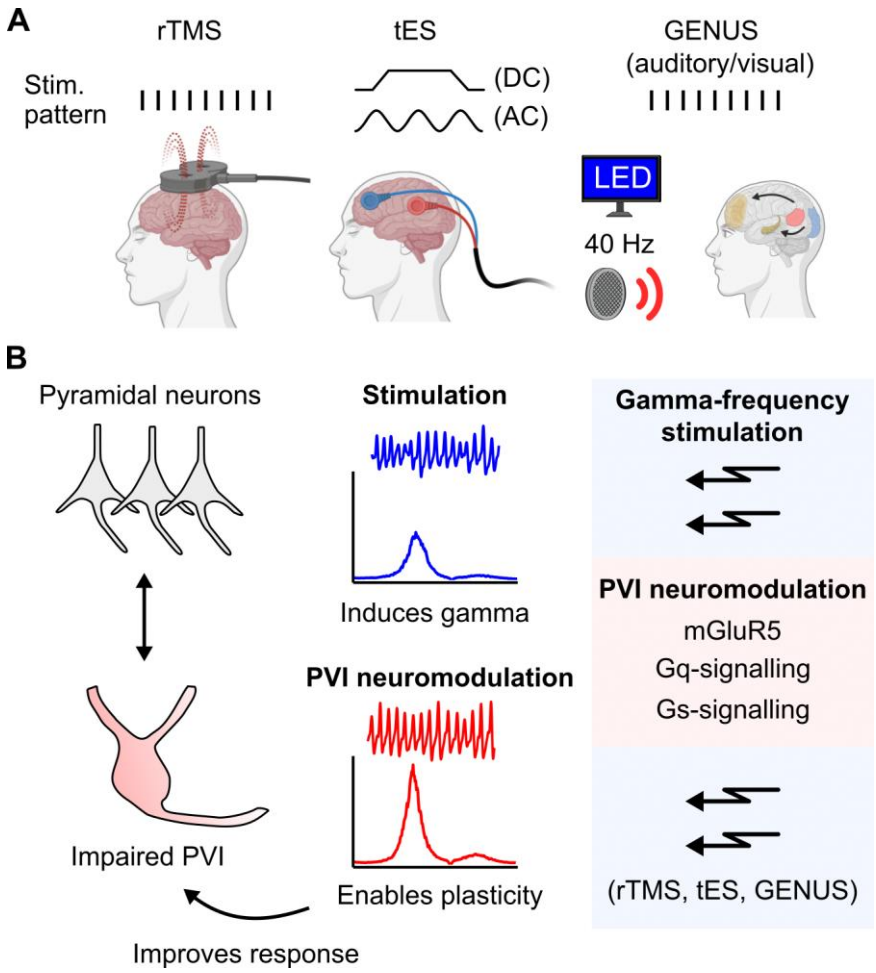

Figure 19: Future therapeutic strategies recruiting gamma-potentiation.

(A) Non-invasive gamma-stimulation recruiting 40 Hertz (Hz) activity in human patients (adapted from Figure 4 in Hadler et al., 2024a). Repetitive transcranial magnetic stimulation (rTMS), transcranial electrical stimulation (tES) and gamma entrainment using sensory stimuli (GENUS) are schematically illustrated with respective stimulation patterns (DC: direct current; AC: alternating current). In GENUS, the prefrontal cortex and hippocampus (highlighted in yellow) are entrained by visual (blue) and auditory (red) cortices. (B) Proposed therapeutical approach incorporating the findings of the study. External stimulation (blue box) recruits the pyramidal neuron and impaired parvalbumin interneuron (PVI) population to resonate at gamma frequencies, albeit at lower power (blue trace and spectrogram). Recruiting neuromodulation in PVIs (red box) lowers the threshold for the induction of plasticity, leading to subsequently improved PVI function and increased gamma oscillations (red trace and spectrogram). Own illustration.

5 Conclusions

Activity-dependent power increases of ex vivo hippocampal gamma-oscillations reflect synaptic plasticity of glutamatergic inputs onto PVIs. This plasticity is caused by a prior interval of hippocampal gamma-oscillations. The bidirectional relationship of cell-to-network plasticity provides a deeper understanding of cortical plasticity processes under physiological conditions, complements existing explanations of the pathogenesis of neuropsychiatric disorders, and serves as a promising starting point for the mechanistically motivated development of future therapies.

A significant strength of this study lies in the reproducibility of the described effect sizes and the experimental control over the mechanisms of pharmacological and molecular interventions. This control is provided by the choice of the ex vivo experimental approach yet warrants caution for the evaluation of future investigations: On the one hand, the mechanistic profile of gamma-potentiation (activation of metabotropic signaling pathways in PVIs and potentiation of CP-AMPAR conductance on PVIs) sets the stage for the study of gamma-plasticity in vivo. On the other hand, the substantial difference between the isolated ex vivo model and the ground truth model in vivo only allows for a limited transfer of the conclusions described here. Any future investigations in vivo and especially in patients will need protocols that permit comparable control over the generation of the gamma-rhythm.

Nonetheless, the cell-type-specific, metabotropically gated plasticity of network oscillations offers significant potential for precise, minimally invasive monitoring of neuropsychiatric therapies, in which targeted manipulations of molecularly defined structures (e.g., the PVI network) can be evaluated and optimized based on their effects on network-level spectral amplitude of the field potential.

Reference list

Adaikkan, C., Tsai, L.-H., 2020. Gamma Entrainment: Impact on Neurocircuits, Glia, and Therapeutic Opportunities. Trends in Neurosciences 43, 24–41. https://doi.org/10.1016/j.tins.2019.11.001

Alle, H., Jonas, P., Geiger, J.R.P., 2001. PTP and LTP at a hippocampal mossy fiber-interneuron synapse. Proceedings of the National Academy of Sciences 98, 14708–14713. https://doi.org/10.1073/pnas.251610898

Arime, Y., Saitoh, Y., Ishikawa, M., Kamiyoshihara, C., Uchida, Y., Fujii, K., Takao, K., Akiyama, K., Ohkawa, N., 2024. Activation of prefrontal parvalbumin interneurons ameliorates working memory deficit even under clinically comparable antipsychotic treatment in a mouse model of schizophrenia. Neuropsychopharmacology. 49, 720–730. https://doi.org/10.1038/s41386-023-01769-z

Barnes, S.A., Pinto-Duarte, A., Kappe, A., Zembrzycki, A., Metzler, A., Mukamel, E.A., Lucero, J., Wang, X., Sejnowski, T.J., Markou, A., Behrens, M.M., 2015. Disruption of mGluR5 in parvalbumin-positive interneurons induces core features of neurodevelopmental disorders. Molecular Psychiatry 20, 1161–1172. https://doi.org/10.1038/mp.2015.113

Bartos, M., Vida, I., Jonas, P., 2007. Synaptic mechanisms of synchronized gamma oscillations in inhibitory interneuron networks. Nature Reviews Neuroscience 8, 45–56. https://doi.org/10.1038/nrn2044

Benussi, A., Cantoni, V., Grassi, M., Brechet, L., Michel, C.M., Datta, A., Thomas, C., Gazzina, S., Cotelli, M.S., Bianchi, M., Premi, E., Gadola, Y., Cotelli, M., Pengo, M., Perrone, F., Scolaro, M., Archetti, S., Solje, E., Padovani, A., Pascual-Leone, A., Borroni, B., 2022. Increasing Brain Gamma Activity Improves Episodic Memory and Restores Cholinergic Dysfunction in Alzheimer's Disease. Annals of Neurology 92, 322–334. https://doi.org/10.1002/ana.26411

Blanco-Duque, C., Chan, D., Kahn, M.C., Murdock, M.H., Tsai, L., 2024. Audiovisual gamma stimulation for the treatment of neurodegeneration. Journal of Internal Medicine 295, 146–170. https://doi.org/10.1111/joim.13755

Bragin, A., Jando, G., Nadasdy, Z., Hetke, J., Wise, K., Buzsaki, G., 1995. Gamma (40-100 Hz) oscillation in the hippocampus of the behaving rat. Journal of Neuroscience 15, 47–60. https://doi.org/10.1523/JNEUROSCI.15-01-00047.1995

Brown, J., Grayson, B., Neill, J.C., Harte, M., Wall, M.J., Ngomba, R.T., 2023. Oscillatory Deficits in the Sub-Chronic PCP Rat Model for Schizophrenia Are Reversed by mGlu5 Receptor-Positive Allosteric Modulators VU0409551 and VU0360172. Cells 12, 919. https://doi.org/10.3390/cells12060919

Buzsáki, G., 2006. Rhythms of the Brain. Oxford University Press. https://doi.org/10.1093/acprof:oso/9780195301069.001.0001

Buzsáki, G., & Draguhn, A., 2004. Neuronal Oscillations in Cortical Networks. Science, 304(5679), 1926–1929. https://doi.org/10.1126/science.1099745

Chen, Y., Granger, A.J., Tran, T., Saulnier, J.L., Kirkwood, A., Sabatini, B.L., 2017. Endogenous Gαq-Coupled Neuromodulator Receptors Activate Protein Kinase A. Neuron 96, 1070-1083.e5. https://doi.org/10.1016/j.neuron.2017.10.023

Cho, K.K.A., Hoch, R., Lee, A.T., Patel, T., Rubenstein, J.L.R., Sohal, V.S., 2015. Gamma Rhythms Link Prefrontal Interneuron Dysfunction with Cognitive Inflexibility in Dlx5/6+/− Mice. Neuron 85, 1332–1343. https://doi.org/10.1016/j.neuron.2015.02.019

Cossart, R., Esclapez, M., Hirsch, J.C., Bernard, C., Ben-Ari, Y., 1998. GluR5 kainate receptor activation in interneurons increases tonic inhibition of pyramidal cells. Nature Neuroscience 1, 470–478. https://doi.org/10.1038/2185

Craig, M.T., Bielska, M.H., Jeffery, K., 2024. Mechanisms and implications of gamma oscillation plasticity. Trends in Neurosciences S0166223624000821. https://doi.org/10.1016/j.tins.2024.05.002

Edelmann, E., Lessmann, V., 2011. Dopamine Modulates Spike Timing-Dependent Plasticity and Action Potential Properties in CA1 Pyramidal Neurons of Acute Rat Hippocampal Slices. Frontiers in Synaptic Neuroscience 3. https://doi.org/10.3389/fnsyn.2011.00006

Etter, G., van der Veldt, S., Manseau, F., Zarrinkoub, I., Trillaud-Doppia, E., Williams, S., 2019. Optogenetic gamma stimulation rescues memory impairments in an Alzheimer's disease mouse model. Nature Communications 10, 5322. https://doi.org/10.1038/s41467-019-13260-9

Fernández-Ruiz, A., Oliva, A., Soula, M., Rocha-Almeida, F., Nagy, G.A., Martin-Vazquez, G., Buzsáki, G., 2021. Gamma rhythm communication between entorhinal cortex and dentate gyrus neuronal assemblies. Science 372, eabf3119. https://doi.org/10.1126/science.abf3119

Fernandez-Ruiz, A., Sirota, A., Lopes-dos-Santos, V., Dupret, D., 2023. Over and above frequency: Gamma oscillations as units of neural circuit operations. Neuron 111, 936–953. https://doi.org/10.1016/j.neuron.2023.02.026

Fisahn, A., Pike, F. G., Buhl, E. H., & Paulsen, O. (1998). Cholinergic induction of network oscillations at 40 Hz in the hippocampus in vitro. *Nature*, *394*(6689), 186–189. https://doi.org/10.1038/28179

Fisahn, A., 2004. Distinct Roles for the Kainate Receptor Subunits GluR5 and GluR6 in Kainate-Induced Hippocampal Gamma Oscillations. Journal of Neuroscience 24, 9658–9668. https://doi.org/10.1523/JNEUROSCI.2973-04.2004

Fuchs, E.C., Doheny, H., Faulkner, H., Caputi, A., Traub, R.D., Bibbig, A., Kopell, N., Whittington, M.A., Monyer, H., 2001. Genetically altered AMPA-type glutamate receptor kinetics in interneurons disrupt long-range synchrony of gamma oscillation. Proceedings of the National Academy of Sciences 98, 3571–3576. https://doi.org/10.1073/pnas.051631898

Fuchs, E.C., Zivkovic, A.R., Cunningham, M.O., Middleton, S., LeBeau, F.E.N., Bannerman, D.M., Rozov, A., Whittington, M.A., Traub, R.D., Rawlins, J.N.P., Monyer, H., 2007. Recruitment of Parvalbumin-Positive Interneurons Determines Hippocampal Function and Associated Behavior. Neuron 53, 591–604. https://doi.org/10.1016/j.neuron.2007.01.031

Geiger, J.R.P., Melcher, T., Koh, D.-S., Sakmann, B., Seeburg, P.H., Jonas, P., Monyer, H., 1995. Relative abundance of subunit mRNAs determines gating and Ca2+ permeability of AMPA receptors in principal neurons and interneurons in rat CNS. Neuron 15, 193–204. https://doi.org/10.1016/0896-6273(95)90076-4

Gray, C. M., König, P., Engel, A. K., & Singer, W. (1989). Oscillatory responses in cat visual cortex exhibit inter-columnar synchronization which reflects global stimulus properties. *Nature*, *338*(6213), 334–337. https://doi.org/10.1038/338334a0

Gray, C. M., & Singer, W. (1989). Stimulus-specific neuronal oscillations in orientation columns of cat visual cortex. *Proceedings of the National Academy of Sciences*, *86*(5), 1698–1702. https://doi.org/10.1073/pnas.86.5.1698

Griffiths, B. J., & Jensen, O. (2023). Gamma oscillations and episodic memory. *Trends in Neurosciences*, *46*(10), 832–846. https://doi.org/10.1016/j.tins.2023.07.003

Hadler, M.D., Alle, H., Geiger, J.R.P., 2024a. Parvalbumin interneuron cell-to-network plasticity: mechanisms and therapeutic avenues. Trends in Pharmacological Sciences 45, 586–601. https://doi.org/10.1016/j.tips.2024.04.003

Hadler, M.D., Tzilivaki, A., Schmitz, D., Alle, H., Geiger, J.R.P., 2024b. Gamma oscillation plasticity is mediated via parvalbumin interneurons. Science Advances 10, eadj7427. https://doi.org/10.1126/sciadv.adj7427

Hainmüller, T., Krieglstein, K., Kulik, A., Bartos, M., 2014. Joint CP-AMPA and group I mGlu receptor activation is required for synaptic plasticity in dentate gyrus fast-spiking interneurons. Proceedings of the National Academy of Sciences 111, 13211–13216. https://doi.org/10.1073/pnas.1409394111

Hájos, N., Paulsen, O., 2009. Network mechanisms of gamma oscillations in the CA3 region of the hippocampus. Neural Networks 22, 1113–1119. https://doi.org/10.1016/j.neunet.2009.07.024

He, X., Li, J., Zhou, G., Yang, J., McKenzie, S., Li, Y., Li, W., Yu, J., Wang, Y., Qu, J., Wu, Z., Hu, H., Duan, S., Ma, H., 2021. Gating of hippocampal rhythms and memory by synaptic plasticity in inhibitory interneurons. Neuron 109, 1013-1028.e9. https://doi.org/10.1016/j.neuron.2021.01.014

Hijazi, S., Smit, A.B., Van Kesteren, R.E., 2023. Fast-spiking parvalbumin-positive interneurons in brain physiology and Alzheimer's disease. Molecular Psychiatry. https://doi.org/10.1038/s41380-023-02168-y

Hoppenrath, K., Härtig, W., Funke, K., 2016. Intermittent Theta-Burst Transcranial Magnetic Stimulation Alters Electrical Properties of Fast-Spiking Neocortical Interneurons in an Age-Dependent Fashion. Frontiers in Neural Circuits 10. https://doi.org/10.3389/fncir.2016.00022

Hu, H., Gan, J., Jonas, P., 2014. Fast-spiking, parvalbumin GABAergic interneurons: From cellular design to microcircuit function. Science 345, 1255263. https://doi.org/10.1126/science.1255263

Huang, Y., Jiang, H., Zheng, Q., Fok, A.H.K., Li, X., Lau, C.G., Lai, C.S.W., 2021. Environmental enrichment or selective activation of parvalbumin-expressing interneurons ameliorates synaptic and behavioral deficits in animal models with schizophrenia-like behaviors during adolescence. Molecular Psychiatry 26, 2533–2552. https://doi.org/10.1038/s41380-020-01005-w

Karunakaran, S., Chowdhury, A., Donato, F., Quairiaux, C., Michel, C.M., Caroni, P., 2016. PV plasticity sustained through D1/5 dopamine signaling required for long-term memory consolidation. Nature Neuroscience 19, 454–464. https://doi.org/10.1038/nn.4231

Klausberger, T., Somogyi, P., 2008. Neuronal Diversity and Temporal Dynamics: The Unity of Hippocampal Circuit Operations. Science 321, 53–57. https://doi.org/10.1126/science.1149381

Korotkova, T., Fuchs, E.C., Ponomarenko, A., von Engelhardt, J., Monyer, H., 2010. NMDA Receptor Ablation on Parvalbumin-Positive Interneurons Impairs Hippocampal Synchrony, Spatial Representations, and Working Memory. Neuron 68, 557–569. https://doi.org/10.1016/j.neuron.2010.09.017

Kullmann, D.M., Lamsa, K.P., 2007. Long-term synaptic plasticity in hippocampal interneurons. Nature Reviews Neuroscience 8, 687–699. https://doi.org/10.1038/nrn2207

Lamsa, K.P., Heeroma, J.H., Somogyi, P., Rusakov, D.A., Kullmann, D.M., 2007. Anti-Hebbian Long-Term Potentiation in the Hippocampal Feedback Inhibitory Circuit. Science 315, 1262–1266. https://doi.org/10.1126/science.1137450

Li, K.T., He, X., Zhou, G., Yang, J., Li, T., Hu, H., Ji, D., Zhou, C., Ma, H., 2022. Rational designing of oscillatory rhythmicity for memory rescue in plasticity-impaired learning networks. Cell Reports 39, 110678. https://doi.org/10.1016/j.celrep.2022.110678

Lu, C.B., Jefferys, J.G.R., Toescu, E.C., Vreugdenhil, M., 2011. In vitro hippocampal gamma oscillation power as an index of in vivo CA3 gamma oscillation strength and spatial reference memory. Neurobiology of Learning and Memory 95, 221–230. https://doi.org/10.1016/j.nlm.2010.11.008

Maiella, M., Casula, E.P., Borghi, I., Assogna, M., D'Acunto, A., Pezzopane, V., Mencarelli, L., Rocchi, L., Pellicciari, M.C., Koch, G., 2022. Simultaneous transcranial electrical and magnetic stimulation boost gamma oscillations in the dorsolateral prefrontal cortex. Scientific Reports 12, 19391. https://doi.org/10.1038/s41598-022-23040-z

Marissal, T., Salazar, R.F., Bertollini, C., Mutel, S., De Roo, M., Rodriguez, I., Müller, D., Carleton, A., 2018. Restoring wild-type-like CA1 network dynamics and behavior during adulthood in a mouse model of schizophrenia. Nature Neuroscience 21, 1412–1420. https://doi.org/10.1038/s41593-018-0225-y

McCutcheon, R.A., Keefe, R.S.E., McGuire, P.K., 2023. Cognitive impairment in schizophrenia: aetiology, pathophysiology, and treatment. Molecular Psychiatry 28, 1902–1918. https://doi.org/10.1038/s41380-023-01949-9

Mukherjee, A., Carvalho, F., Eliez, S., Caroni, P., 2019. Long-Lasting Rescue of Network and Cognitive Dysfunction in a Genetic Schizophrenia Model. Cell 178, 1387-1402.e14. https://doi.org/10.1016/j.cell.2019.07.023

Murty, D.V., Manikandan, K., Kumar, W.S., Ramesh, R.G., Purokayastha, S., Nagendra, B., Ml, A., Balakrishnan, A., Javali, M., Rao, N.P., Ray, S., 2021. Stimulus-induced gamma rhythms are weaker in human elderly with mild cognitive impairment and Alzheimer's disease. eLife 10, e61666. https://doi.org/10.7554/eLife.61666

Nagai, Y., Miyakawa, N., Takuwa, H., Hori, Y., Oyama, K., Ji, B., Takahashi, M., Huang, X.-P., Slocum, S.T., DiBerto, J.F., Xiong, Y., Urushihata, T., Hirabayashi, T., Fujimoto, A., Mimura, K., English, J.G., Liu, J., Inoue, K., Kumata, K., Seki, C., Ono, M., Shimojo, M., Zhang, M.-R., Tomita, Y., Nakahara, J., Suhara, T., Takada, M., Higuchi, M., Jin, J., Roth, B.L., Minamimoto, T., 2020. Deschloroclozapine, a potent and selective chemogenetic actuator enables rapid neuronal and behavioral modulations in mice and monkeys. Nature Neuroscience 23, 1157–1167. https://doi.org/10.1038/s41593-020-0661-3

Ognjanovski, N., Broussard, C., Zochowski, M., Aton, S.J., 2018. Hippocampal Network Oscillations Rescue Memory Consolidation Deficits Caused by Sleep Loss. Cerebral Cortex 28, 3711–3723. https://doi.org/10.1093/cercor/bhy174

Ognjanovski, N., Schaeffer, S., Wu, J., Mofakham, S., Maruyama, D., Zochowski, M., Aton, S.J., 2017. Parvalbumin-expressing interneurons coordinate hippocampal network dynamics required for memory consolidation. Nature Communications 8, 15039. https://doi.org/10.1038/ncomms15039

Petrovic, M.M., Viana da Silva, S., Clement, J.P., Vyklicky, L., Mulle, C., González-González, I.M., Henley, J.M., 2017. Metabotropic action of postsynaptic kainate receptors triggers hippocampal long-term potentiation. Nature Neuroscience 20, 529–539. https://doi.org/10.1038/nn.4505

Pietersen, A.N.J., Ward, P.D., Hagger-Vaughan, N., Wiggins, J., Jefferys, J.G.R., Vreugdenhil, M., 2014. Transition between fast and slow gamma modes in rat hippocampus area CA1 *in vitro* is modulated by slow CA3 gamma oscillations: Intrinsic fast CA1 gamma is suppressed by slow CA3 gamma. The Journal of Physiology 592, 605–620. https://doi.org/10.1113/jphysiol.2013.263889

Raven, F., Aton, S.J., 2021. The Engram's Dark Horse: How Interneurons Regulate State-Dependent Memory Processing and Plasticity. Frontiers in Neural Circuits 15, 750541. https://doi.org/10.3389/fncir.2021.750541

Reiner, A., Levitz, J., 2018. Glutamatergic Signaling in the Central Nervous System: Ionotropic and Metabotropic Receptors in Concert. Neuron 98, 1080–1098. https://doi.org/10.1016/j.neuron.2018.05.018

Rook, J.M., Xiang, Z., Lv, X., Ghoshal, A., Dickerson, J.W., Bridges, T.M., Johnson, K.A., Foster, D.J., Gregory, K.J., Vinson, P.N., Thompson, A.D., Byun, N., Collier, R.L., Bubser, M., Nedelcovych, M.T., Gould, R.W., Stauffer, S.R., Daniels, J.S., Niswender, C.M., Lavreysen, H., Mackie, C., Conde-Ceide, S., Alcazar, J., Bartolomé-Nebreda, J.M., Macdonald, G.J., Talpos, J.C., Steckler, T., Jones, C.K., Lindsley, C.W., Conn, P.J., 2015. Biased mGlu 5 -Positive Allosteric Modulators Provide In Vivo Efficacy without Potentiating mGlu 5 Modulation of NMDAR Currents. Neuron 86, 1029–1040. https://doi.org/10.1016/j.neuron.2015.03.063

Roth, B.L., 2016. DREADDs for Neuroscientists. Neuron 89, 683–694. https://doi.org/10.1016/j.neuron.2016.01.040

Shen, M., Guo, Y., Dong, Q., Gao, Y., Stockton, M.E., Li, M., Kannan, S., Korabelnikov, T., Schoeller, K.A., Sirois, C.L., Zhou, C., Le, J., Wang, D., Chang, Q., Sun, Q.-Q., Zhao, X., 2021. FXR1 regulation of parvalbumin interneurons in the prefrontal cortex is critical for schizophrenia-like behaviors. Molecular Psychiatry. https://doi.org/10.1038/s41380-021-01096-z

Sohal, V.S., Zhang, F., Yizhar, O., Deisseroth, K., 2009. Parvalbumin neurons and gamma rhythms enhance cortical circuit performance. Nature 459, 698–702. https://doi.org/10.1038/nature07991

Tort, A.B.L., Komorowski, R.W., Manns, J.R., Kopell, N.J., Eichenbaum, H., 2009. Theta–gamma coupling increases during the learning of item–context associations. Proceedings of the National Academy of Sciences 106, 20942–20947. https://doi.org/10.1073/pnas.0911331106

Tzilivaki, A., Tukker, J.J., Maier, N., Poirazi, P., Sammons, R.P., Schmitz, D., 2023. Hippocampal GABAergic interneurons and memory. Neuron S0896627323004750. https://doi.org/10.1016/j.neuron.2023.06.016

Uhlhaas, P.J., Singer, W., 2010. Abnormal neural oscillations and synchrony in schizophrenia. Nature Reviews Neuroscience 11, 100–113. https://doi.org/10.1038/nrn2774

Wagatsuma, A., Okuyama, T., Sun, C., Smith, L.M., Abe, K., Tonegawa, S., 2018. Locus coeruleus input to hippocampal CA3 drives single-trial learning of a novel context. Proceedings of the National Academy of Sciences 115, E310–E316. https://doi.org/10.1073/pnas.1714082115

Wang, H.-Y., MacDonald, M.L., Borgmann-Winter, K.E., Banerjee, A., Sleiman, P., Tom, A., Khan, A., Lee, K.-C., Roussos, P., Siegel, S.J., Hemby, S.E., Bilker, W.B., Gur, R.E., Hahn, C.-G., 2020. mGluR5 hypofunction is integral to glutamatergic dysregulation in schizophrenia. Molecular Psychiatry 25, 750–760. https://doi.org/10.1038/s41380-018-0234-y

Whittington, M. A., Traub, R. D., & Jefferys, J. G. R. (1995). Synchronized oscillations in interneuron networks driven by metabotropic glutamate receptor activation. *Nature*, *373*(6515), 612–615. https://doi.org/10.1038/373612a0

Xia, F., Richards, B.A., Tran, M.M., Josselyn, S.A., Takehara-Nishiuchi, K., Frankland, P.W., 2017. Parvalbumin-positive interneurons mediate neocortical-hippocampal interactions that are necessary for memory consolidation. eLife 6, e27868. https://doi.org/10.7554/eLife.27868

Yang, Sunggu, Yang, Sungchil, Moreira, T., Hoffman, G., Carlson, G.C., Bender, K.J., Alger, B.E., Tang, C.-M., 2014. Interlamellar CA1 network in the hippocampus. Proceedings of the National Academy of Sciences 111, 12919–12924. https://doi.org/10.1073/pnas.1405468111

Zarnadze, S., Bäuerle, P., Santos-Torres, J., Böhm, C., Schmitz, D., Geiger, J.R.P., Dugladze, T., Gloveli, T., 2016. Cell-specific synaptic plasticity induced by network oscillations. eLife 5, e14912. https://doi.org/10.7554/eLife.14912

Zheng, C., Bieri, K.W., Trettel, S.G., Colgin, L.L., 2015. The relationship between gamma frequency and running speed differs for slow and fast gamma rhythms in freely behaving rats: Slow and Fast Gamma Correlations with Speed. Hippocampus 25, 924–938. https://doi.org/10.1002/hipo.22415

Zhong, W., Ciatipis, M., Wolfenstetter, T., Jessberger, J., Müller, C., Ponsel, S., Yanovsky, Y., Brankačk, J., Tort, A.B.L., Draguhn, A., 2017. Selective entrainment of gamma subbands by different slow network oscillations. Proceedings of the National Academy of Sciences 114, 4519–4524. https://doi.org/10.1073/pnas.1617249114

Statutory Declaration

“I, Michael Hadler, by personally signing this document in lieu of an oath, hereby affirm that I prepared the submitted dissertation on the topic:

„Plasticity of neuronal gamma-oscillations via the specific cellular plasticity of parvalbumin-positive interneurons“ (English),

or,

„Plastizität neuronaler Gamma-Oszillationen durch die spezifische zelluläre Plastizität Parvalbumin-positiver Interneurone“ (German),

independently and without the support of third parties, and that I used no other sources and aids than those stated.

All parts which are based on the publications or presentations of other authors, either in letter or in spirit, are specified as such in accordance with the citing guidelines. The sections on methodology (in particular regarding practical work, laboratory regulations, statistical processing) and results (in particular regarding figures, charts and tables) are exclusively my responsibility.

Furthermore, I declare that I have correctly marked all of the data, the analyses, and the conclusions generated from data obtained in collaboration with other persons, and that I have correctly marked my own contribution and the contributions of other persons (cf. declaration of contribution). I have correctly marked all texts or parts of texts that were generated in collaboration with other persons.

My contributions to any publications to this dissertation correspond to those stated in the below joint declaration made together with the supervisor. All publications created within the scope of the dissertation comply with the guidelines of the ICMJE (International Committee of Medical Journal Editors; http://www.icmje.org) on authorship. In addition, I declare that I shall comply with the regulations of Charité – Universitätsmedizin Berlin on ensuring good scientific practice.

I declare that I have not yet submitted this dissertation in identical or similar form to another Faculty.

The significance of this statutory declaration and the consequences of a false statutory declaration under criminal law (Sections 156, 161 of the German Criminal Code) are known to me.”

Date Signature (Michael Hadler)

Declaration of your own contribution to the publication(s)

I contributed to the following publication:

Hadler, M. D., Tzilivaki, A., Schmitz, D., Alle, H., & Geiger, J. R. P., Gamma oscillation plasticity is mediated via parvalbumin interneurons, *Science Advances*, 2024.

Contributions:

1. Conceptualization

The motivation of this project was to identify evidence for an interneuron-specific component of network oscillation plasticity. Under Professor Geiger's supervision (primary supervisor), I developed an experimental protocol for the highly reproducible investigation of network oscillation plasticity in the gamma-frequency range. After establishing this protocol, I independently researched and planned various strategies to investigate cell-type-specific contributions to this plasticity. In particular, this entailed the differential use of pharmacology and animal husbandry (in close collaboration with Andrea Wilke, technical assistant at the Institute of Neurophysiology).

2. Electrophysiology (experimental work)

All acute brain slice preparations were performed by myself (following initial guidance from Professor Geiger and Dr. Alle, co-supervisor), and all electrophysiological datasets were collected by me.

I primarily used an established experimental setup (Klisch, C., 2016, Establishment of a three-stage measurement concept for electrophysiological analysis of acute brain slices, Freie Universität Berlin) to perform multiple simultaneous single-field potential recordings in acute mouse brain slices (Figures 1–3 and 5–6 of the publication, as well as Figures S1–S3 and S5–S8 of the appendix), after receiving initial instructions from Dr. Gerevich (co-supervisor).

Additionally, I independently established the use of a commercially available multi-electrode array (MEA) setup in our institute, conducted pilot studies to optimize the handling of this setup, and collected all data presented in Figure 3 of the publication and Figure S4 of the appendix.

3. Data analysis and visualization

All analyses and visualizations presented were independently developed by myself using the programming environments MATLAB (from MATLAB version 9.6) and RStudio (R version 4.1.3), and curated for subsequent publication. In collaboration with Professor Geiger and Dr. Alle, the reproducibility of the analysis protocols was ensured, and the clarity of visualizations was refined through multiple iterations.

The simulation results generated by Alexandra Tzilivaki, as shown in Figure 4, were also analyzed and visualized by me. These results were curated and discussed in cooperation with Ms. Tzilivaki, Professor Geiger, Dr. Alle, and Professor Schmitz (supervisor of Ms. Tzilivaki).

4. Manuscript preparation

After completing the data collection and creating the initial draft of the figures, I drafted the original version of the publication manuscript in its entirety. This version underwent several revisions under my curation, with input from all authors involved.

_____

Signature of doctoral candidate (Michael Hadler)

Excerpt from Journal Summary List

Journal Data Filtered By: **Selected JCR Year: 2022** Selected Editions: SCIE,SSCI

Selected Categories: **“MULTIDISCIPLINARY SCIENCES”** Selected Category

Scheme: WoS

Total number: 73 Journale

Rank	Journal Title	Total Cites	Journal Impact Factor	Eigenfaktor
1	NATURE	964,876	64.8	1.10309
2	SCIENCE	818,308	56.9	0.80079
3	Nature Human Behaviour	14,216	29.9	0.05276
4	National Science Review	13,369	20.6	0.02511
5	Science Bulletin	15,992	18.9	0.02733
6	Nature Communications	675,323	16.6	1.40879
7	**Science Advances**	**126,246**	**13.6**	**0.33133**
8	PROCEEDINGS OF THE NATIONAL ACADEMY OF SCIENCES OF THE UNITED STATES OF AMERICA	788,686	11.1	0.67974
9	Research	4,694	11.0	0.00775
10	Journal of Advanced Research	9,575	10.7	0.00813

Printing copy(s) of the publication(s)

NEUROSCIENCE

Gamma oscillation plasticity is mediated via parvalbumin interneurons

Michael D. Hadler[1,2]*, Alexandra Tzilivaki[1,3,4], Dietmar Schmitz[1,3,4,5,6,7], Henrik Alle[1,2], Jörg R. P. Geiger[1,2]*

Understanding the plasticity of neuronal networks is an emerging field of (patho-) physiological research, yet the underlying cellular mechanisms remain poorly understood. Gamma oscillations (30 to 80 hertz), a biomarker of cognitive performance, require and potentiate glutamatergic transmission onto parvalbumin-positive interneurons (PVIs), suggesting an interface for cell-to-network plasticity. In ex vivo local field potential recordings, we demonstrate long-term potentiation of hippocampal gamma power. Gamma potentiation obeys established rules of PVI plasticity, requiring calcium-permeable AMPA receptors (CP-AMPARs) and metabotropic glutamate receptors (mGluRs). A microcircuit computational model of CA3 gamma oscillations predicts CP-AMPAR plasticity onto PVIs critically outperforms pyramidal cell plasticity in increasing gamma power and completely accounts for gamma potentiation. We reaffirm this ex vivo in three PVI-targeting animal models, demonstrating that gamma potentiation requires PVI-specific signaling via a Gq/PKC pathway comprising mGluR5 and a Gi-sensitive, PKA-dependent pathway. Gamma activity–dependent, metabotropically mediated CP-AMPAR plasticity on PVIs may serve as a guiding principle in understanding network plasticity in health and disease.

INTRODUCTION

Cortical networks implement task-specific computations by synchronizing the firing patterns of neurons to a set of defined rhythms, neuronal oscillations (*1*, *2*). Oscillations are distinct regarding both the cortical state that they accompany and the underlying synaptic interactions between the participating neurons (*3*, *4*). Similar to the plasticity of synaptic weights, the spectral amplitude ("power") of distinct oscillatory patterns adapts following learning (*5*–*7*) or deteriorates in states of disease (*8*). Crucially, such changes coincide with either beneficial or detrimental changes in the respective behavioral or cognitive performance. Experimental approaches using either sensory stimuli or optogenetic strategies corroborate the causal link between oscillatory amplitude and cognitive performance on short timescales (*9*–*11*) yet fail to explain how these changes are recalled after prolonged periods as required for successful learning. This warrants a cellular storage mechanism of oscillatory response tuning innate to neuronal networks.

Hippocampal gamma oscillations (30 to 80 Hz) contribute to the generation, storage, and retrieval of memories and have been studied extensively in vivo (*12*, *13*), ex vivo (*14*), and in silico (*15*). In the CA3 subregion, an understanding has emerged that gamma activity results from precisely timed synaptic feedback loops between local pyramidal cells and interneurons (*16*–*18*). Particularly fast-spiking, parvalbumin-positive interneurons (PVIs) are equipped with specific synaptic properties that facilitate synchronization at gamma frequencies, as they quickly transform converging glutamatergic inputs via GluA2-lacking, calcium-permeable AMPA receptors (CP-AMPARs) into divergent, powerful inhibition (*19*). During periods of increased neuronal activity, this promotes the co-activation of postsynaptic cells at short time intervals (*20*, *21*), benefiting the induction of synaptic plasticity. In line with this, recent studies have highlighted a vital importance of PVI activation for memory formation and maintenance (*22*–*25*). However, it is unclear how this relates to their role in promoting synchrony and further complicated by the fact that PVIs themselves are subjected to various forms of anatomical (*26*), molecular (*27*), and synaptic plasticity (*28*). It is therefore conceivable that PVI plasticity is sufficient to store long-term changes of gamma activity, facilitating its reinstatement upon retrieval.

We previously demonstrated that the induction of network gamma oscillations in vivo and ex vivo evokes long-term potentiation (LTP) of glutamatergic inputs onto both pyramidal cells and PVIs on a cellular level (*29*). Gamma-induced plasticity is mediated via group I metabotropic glutamate receptors (mGluRs), yet a broader profile of the involved signaling cascades remains to be determined. This prompts the question whether plasticity on a synaptic level affects later overall network activity and, if so, which role is attributed to the specific plasticity obtained by PVIs.

Here, in an ex vivo slice model of murine CA3, we demonstrate that evoked gamma power is markedly increased hours after previous episodes of gamma activity. CP-AMPARs not only are required for the generation of the gamma rhythm but also mediate the subsequent increase of power that we term "gamma potentiation." In an in silico microcircuit model of CA3 gamma oscillations, we predict that an increase of CP-AMPAR conductances at the pyramidal cell–to–PVI synapse completely accounts for gamma potentiation. Using both pharmacological and genetic tools specific to known plasticity rules of PVIs, we confirm that gamma potentiation can be explained entirely by the activation of metabotropic pathways in PVIs and uncover an additional requirement of both protein kinase C (PKC) and protein kinase A (PKA) activation. The cell-to-network transfer of PV input plasticity to output oscillations provides a synaptic basis to gamma frequency–specific network plasticity.

[1]Charité-Universitätsmedizin Berlin, corporate member of Freie Universität Berlin, Humboldt-Universität zu Berlin, Berlin Institute of Health, Charitéplatz 1, 10117 Berlin, Germany. [2]Institute of Neurophysiology, Charité-Universitätsmedizin Berlin, Berlin, Germany. [3]Einstein Center for Neurosciences Berlin, Charitéplatz 1, 10117 Berlin, Germany. [4]Neurocure Cluster of Excellence, Charitéplatz 1, 10117 Berlin, Germany. [5]German Center for Neurodegenerative Diseases (DZNE), Berlin, Germany. [6]Bernstein Center for Computational Neuroscience, Berlin, Germany. [7]Max Delbrück Center for Molecular Medicine in the Helmholtz Association, Robert Rössle-Straße 10, 13125 Berlin, Germany.
*Corresponding author. Email: michael.hadler@charite.de (M.D.H); joerg.geiger@charite.de (J.R.P.G.)

RESULTS

Gamma potentiation in the mouse hippocampus

In acute transverse hippocampal slices of adolescent mice [postnatal day 45 (P45) to P70], we performed multiple single-site local field potential (LFP) recordings in the CA3 pyramidal cell layer. After an initial recording of baseline activity, in which no oscillatory activity was detected, network oscillations in the low–gamma frequency range (25 to 45 Hz, recorded at 32° to 34°C) were reliably induced by bath application of kainate (KA_1, 150 nM for 30 min at 1.5 ml/min). Following a 1-hour washout period, during which oscillatory activity had completely subsided after 30 to 40 min, a second, identical period of network activity was induced (KA_2, 150 nM for 30 min). During this second application period of KA, peak low gamma power on average increased approximately twofold (Fig. 1A; KA_1: 5.66 [1.88, 16.93] μV^2 versus KA_2: 11.84 [3.40, 32.50] μV^2, $n = 15$ slices tested; $P = 6.1 \times 10^{-5}$, Wilcoxon signed-rank test). Whereas the absolute values of peak gamma power and frequency in the first induction period were highly variable across individual slices and conditions tested (fig. S1), they did not correlate with the subsequent relative increase of peak power (power KA_2/KA_1: 2.13 ± 0.11, from here on referred to as gamma potentiation). Across all sole LFP experiments reported in this study, the average potentiation was highly reproducible among control conditions across experimental groups, highlighting the stability of our ex vivo approach (fig. S1).

We confirmed that the increase of peak power was conserved even if the washout period was extended to 3 hours, suggesting a long-lasting change of oscillatory network excitability (Fig. 1, B and C; power KA_2/KA_1: 2.99 ± 0.71, $n = 10$). However, the overall magnitude of potentiation after 3 hours did not cumulate following two successive application periods of KA, indicating a saturating effect of the first induction period (fig. S2). All subsequently reported potentiation experiments were evaluated after a 1-hour waiting period.

In dual-site recordings, potentiation recorded in CA3 was concomitantly observed in downstream CA1 (fig. S3; CA1 power KA_2/KA_1: 2.80 ± 0.52, $n = 15$), which in intact slices is synchronized by CA3 in the low–gamma frequency range via the Schaffer collateral pathway (*30*). In "CA1-Mini" slices, in which CA3 and the subiculum are disconnected from CA1 (*31*), application of KA evokes rhythmic mid-gamma activity (50 to 60 Hz, recorded at 32° to 34°C). Applying an adjusted application protocol (400 nM KA, 2 × 30 min with 60-min washout) again revealed a roughly twofold increase of peak mid-gamma power (fig. S3; CA1-Mini power KA_2/KA_1: 1.81 ± 0.12).

These findings suggest a ubiquitous plasticity rule, by which intrinsic gamma activity in CA3 or CA1 induces long-term changes across the local microcircuit and enhances its oscillatory response on repeated identical stimulation. Our finding in transverse CA1-Mini slices, a slice model with reduced recurrent synaptic excitation

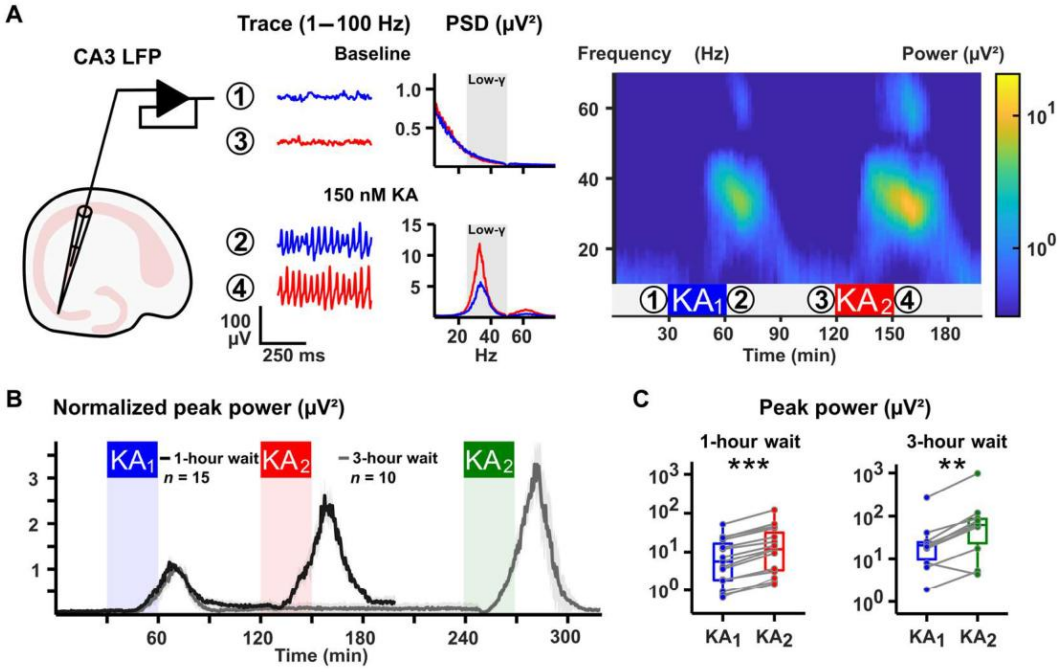

Fig. 1. Gamma potentiation in ex vivo mouse hippocampal CA3. (**A**) Left: Schematic of a hippocampal brain slice with an LFP electrode in the pyramidal cell layer of CA3. Center: Close-up band-pass–filtered traces (1 to 100 Hz) of the time periods preceding KA application (baseline, insets 1 and 3 in the pseudo-color plot) and during maximum gamma power in CA3 ("150 nM KA," insets 2 and 4). The root mean square (RMS)–averaged power spectral density (PSD) was obtained over a 10-min time window. Gray inset low-γ in the PSDs denotes the window spanning from 25 to 50 Hz. Right: Pseudo-color plot of the entire recording. Blue and red insets "KA_1" and "KA_2" denote the time period of KA application (150 nM). The color bar denotes the RMS-averaged power (log scale). (**B**) Time-power plot of peak power (15 to 49 Hz) for experiments with either 1- or 3-hour delay normalized to the first application period. Ribbons denote the 95% confidence interval. *n* is number of slices tested. (**C**) Paired boxplots of peak gamma power in both application periods with either 1-hour ($n = 15$) or 3-hour ($n = 10$) delay. $^{**}P < 0.01$ and $^{***}P < 0.001$ (Wilcoxon signed-rank test).

onto pyramidal cells (*32*), in particular points to plasticity acquired at local pyramidal cell–interneuron interactions.

Calcium-permeable AMPA receptors essentially contribute to the gamma rhythm, mediate and express gamma potentiation

Gamma oscillations arise from synaptic interactions between pyramidal cells and interneurons (*16*). Whereas GABA-mediated transmission is indispensable to oscillogenesis, we could analyze the contribution of individual glutamatergic components to gamma synchronization and its potentiation using pharmacology. To specifically address synaptic excitation onto interneurons, we targeted calcium-permeable AMPA receptors (CP-AMPARs) with the open-channel blocker naphthyl-spermine (NASPM; 50 to 100 μM) and compared this to approaches targeting AMPARs globally (GYKI-53655, 50 μM) and/or NMDARs (D-AP5, 50 μM) (Fig. 2A).

CA3 LFP recordings revealed a fundamental contribution of CP-AMPARs to gamma synchronization: Slices preincubated with NASPM before stimulation with KA exhibited oscillations markedly slower than controls (peak frequency control: 33.12 ± 0.74 Hz, $n = 19$ versus NASPM: 23.09 ± 1.04 Hz, $n = 9$; $P = 9.23 \times 10^{-9}$, generalized linear model), yet clearly synchronous. This decelerating effect was even more pronounced after blocking all AMPARs with GYKI-53655 (peak frequency GYKI: 14.71 ± 0.72 Hz, $n = 9$; $P = 1.75 \times 10^{-19}$ versus control, generalized linear model). Last, co-application of GYKI-53655 and D-AP5, which alone did not affect gamma activity, prevented the emergence of oscillations in eight of the nine slices tested (Fig. 2, B and C). We further confirmed the specific contribution of CP-AMPARs to the generation and maintenance of gamma activity in perforated multielectrode array (pMEA) experiments, permitting short-term drug application. Gamma activity was first established via KA, followed by an intermittent co-application of NASPM. Oscillations quickly desynchronized, quantified as a variable reduction of either peak power and/or frequency, as well as a breakdown of inter-site cross-correlation across CA3 recording sites, which partially recovered following washout of NASPM (fig. S4, A to C). Concerning gamma potentiation, when either GYKI-53655 or NASPM was pre-applied to our LFP protocol, the power of the resulting oscillations did not significantly increase during the second induction period (Fig. 2, D and E; GYKI power KA_1: 1.43 [0.90, 9.22] μV^2 versus KA_2: 3.89 [1.20, 14.21] μV^2, $n = 9$; $P = 0.10$, Wilcoxon signed-rank test; NASPM power KA_1: 16.57 [14.27, 18.52] μV^2 versus KA_2: 15.20 [13.79, 19.52] μV^2, $n = 9$; $P = 1.0$, Wilcoxon signed-rank test). D-AP5, on the other hand, had no such effect, with potentiation remaining unchanged (power KA_2/KA_1 control: 2.58 ± 0.21, $n = 19$ versus D-AP5: 2.38 ± 0.34, $n = 9$; $P = 0.61$, generalized linear model). To exclude a possible contribution of KA receptors, we also tested for effects of UBP-302 (10 μM), an antagonist to the GluK1-subunit. Whereas preincubation with UBP-302 did raise the threshold for gamma oscillation induction (400 nM instead of 150 nM), it did not prevent subsequent plasticity (fig. S5).

The dual role of CP-AMPARs in establishing gamma activity and mediating subsequent network plasticity limited the conclusions of our continuous LFP recordings. Combining our LFP protocol with subsequent pMEA recordings (6 × 10 grid, 100-μm interelectrode distance) allowed us to observe gamma oscillations at multiple sites covering CA3 and robustly compare independent samples. First, slices were either treated with KA as previously or perfused with regular artificial cerebrospinal fluid (ACSF) in LFP recordings. Slices were then left to rest for 1 to 3 hours and subsequently placed on pMEAs. In control experiments, both treated and untreated slices were stimulated with KA (200 nM, 3 min at 10 ml/min, 32° to 34°C), inducing low gamma activity (30 to 40 Hz) at sites covering the pyramidal cell layer of CA3c to CA3a (Fig. 3A). For each slice recorded, the electrode recording the highest gamma power was identified as the "lead electrode," variably situated in CA3c, CA3b, or CA3a. In both naïve ("KA_1") and treated ("KA_2") slices, peak power recorded at sites removed from the lead electrode gradually decreased as a function of intralaminar distance (Fig. 3B, 100 μm to 1 mm). Comparing these distance-based values revealed that, at all sites including the lead electrode, peak gamma power was markedly increased in treated slices compared to untreated slices (Fig. 3C; P values KA_1 versus KA_2 lead electrode/0 μm, 1.5×10^{-3}; <200 μm, 6.8×10^{-6}; <400 μm, 1.9×10^{-6}; <600 μm, 4.9×10^{-6}; <800 μm, 2.7×10^{-4}; <1000 μm, 2.2×10^{-3}; multiple Mann-Whitney U tests corrected by Holm). Therefore, gamma potentiation is expressed in an activity-dependent manner across the entire CA3 region.

In a separate set of experiments, both naïve and treated slices were perfused with NASPM (100 μM) once placed on the pMEAs and stimulated with KA (Fig. 3D). As observed in our LFP recordings, peak frequencies of both unstimulated (NASPM + KA_1) and stimulated slices (NASPM + KA_2) were decelerated (17 to 23 Hz) toward control (Fig. 3E) yet comparable in peak power and inter-site synchrony (fig. S4, D and E). However, other than in control recordings (lead electrode power KA_1: 8.14 [5.33, 13.16] μV^2 versus KA_2: 17.82 [15.84, 20.46] μV^2, $n = 11$; $P = 1.5 \times 10^{-3}$, Mann-Whitney U test), there was no increase of peak power at the lead electrode sites of unstimulated and stimulated slices after NASPM application (Fig. 3F). On the contrary, we observed a trend toward decrease that was not statistically significant (lead electrode power KA_1: 17.34 [8.86, 20.79] μV^2 versus KA_2: 7.93 [4.15, 15.88] μV^2, n = 11; $P = 0.15$, Mann-Whitney U test). Therefore, the increase of peak power is not just induced but also expressed via the activation of CP-AMPARs.

In summary, we could pharmacologically dissect mechanisms of gamma potentiation regarding the ionotropic glutamatergic transmission underlying its induction and expression: Whereas NMDARs and AMPARs contribute differentially to KA-driven oscillations, the generation and subsequent potentiation of gamma oscillations are mediated by AMPARs, expressed specifically by CP-AMPARs in an activity-dependent manner and independent of NMDARs and GluK1. This is strongly indicative of glutamatergic synaptic plasticity onto interneurons (*28*).

A biophysically constrained microcircuit model of CA3 low gamma oscillations predicts superior transfer of PVI-LTP to the resulting field potential

Gamma oscillations induce glutamatergic LTP onto both pyramidal cells (PYR) and predominantly CP-AMPAR–expressing PVIs (*29*). Whereas our pharmacological data suggested that an increase of CP-AMPA conductance at the PYR-PVI synapse underlies gamma potentiation, LTP at the calcium-impermeable AMPAR (CI-AMPAR)–expressing PYR-PYR synapse may, too, directly contribute to changes in the field potential or act heterosynaptically in recruiting PVIs. Lacking experimental tools to selectively target plasticity at PYR-PYR synapses, we turned to an in silico approach using computational modeling.

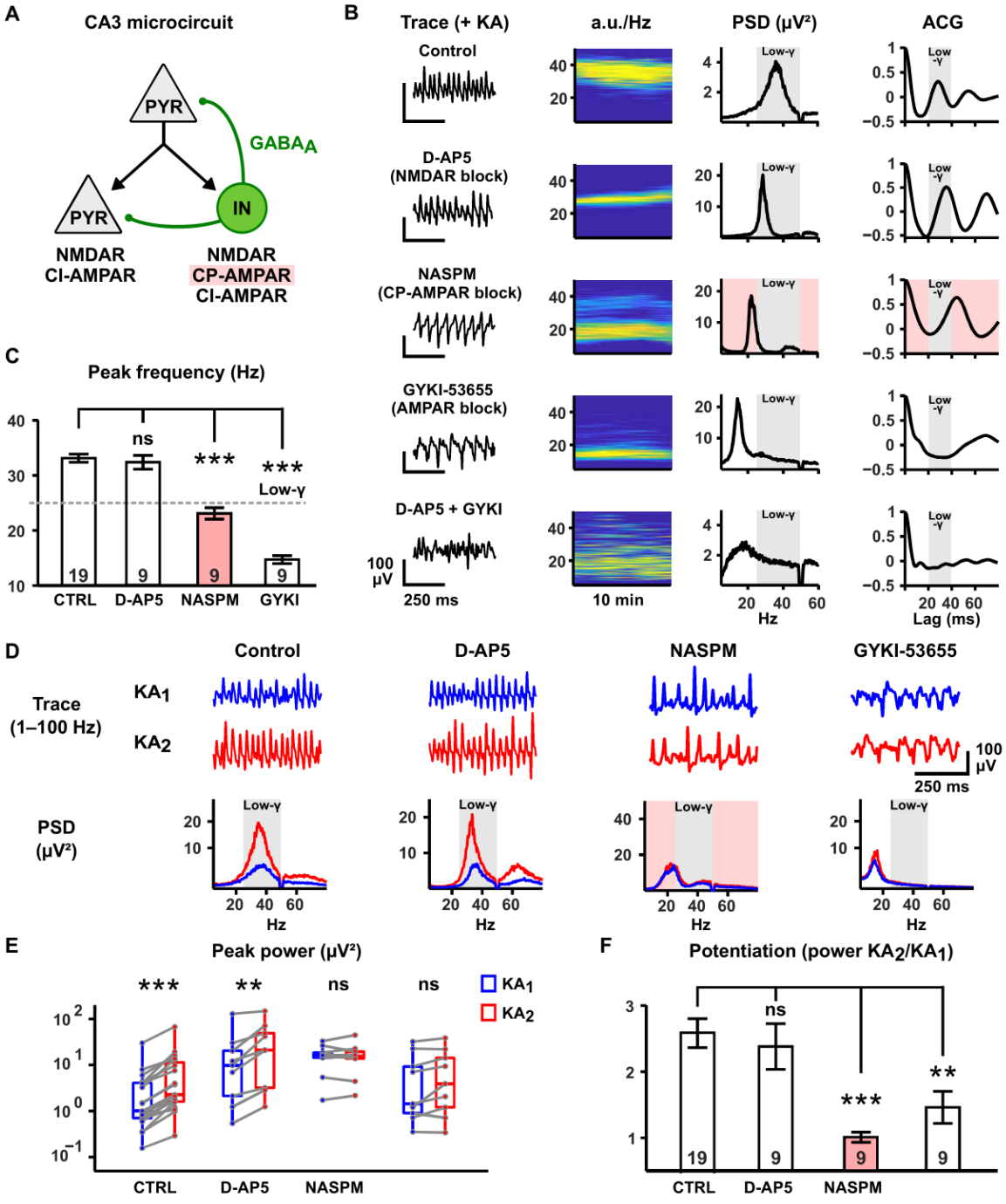

Fig. 2. Calcium-permeable AMPA receptors essentially contribute to the generation of the gamma rhythm and mediate gamma potentiation. (**A**) Synapse-type–specific targeting of glutamatergic transmission in CA3. Pyramidal cell (PYR) synapses targeting other PYRs express NMDA and calcium-impermeable AMPA receptors (CI-AMPARs). PYR synapses targeting interneurons (INs) additionally express calcium-permeable AMPA receptors (CP-AMPARs, pink inset). INs provide inhibition via γ-aminobutyric acid type A ($GABA_A$) receptors. (**B**) Contribution of ionotropic glutamate receptors to KA-induced oscillations. Traces, pseudo-color plots (power values plotted in arbitrary units, "a.u."), PSDs, and autocorrelograms (ACGs) of KA-induced oscillations after blockade of different ionotropic glutamate receptors. Gray insets low-γ in the PSDs and ACGs denote the windows spanning from 25 to 50 Hz and from 20 to 40 ms, respectively. Pink inset highlights the specific blockade of CP-AMPARs by NASPM. There is no discernible oscillatory activity under co-application of D-AP5 and GYKI. (**C**) Barplot summarizing the peak frequencies in the oscillating conditions in (B). Gray dashed line indicates the lower border of the low-γ frequency range (25 Hz). *** $P < 0.001$ (generalized linear model). (**D**) Exemplary potentiation experiments for the oscillating conditions in (B). (**E**) Paired boxplots of respective peak power values during KA_1 and KA_2 obtained in experiments shown in (D). ***$P < 0.001$, **$P < 0.01$, and ns (not significant), $P > 0.05$ (Wilcoxon signed-rank test). (**F**) Barplot of the magnitude of potentiation (peak power KA_2/KA_1) for the experiments in (E). ***$P < 0.001$ and **$P < 0.01$ (generalized linear model). Numbers in barplots denote number of slices tested.

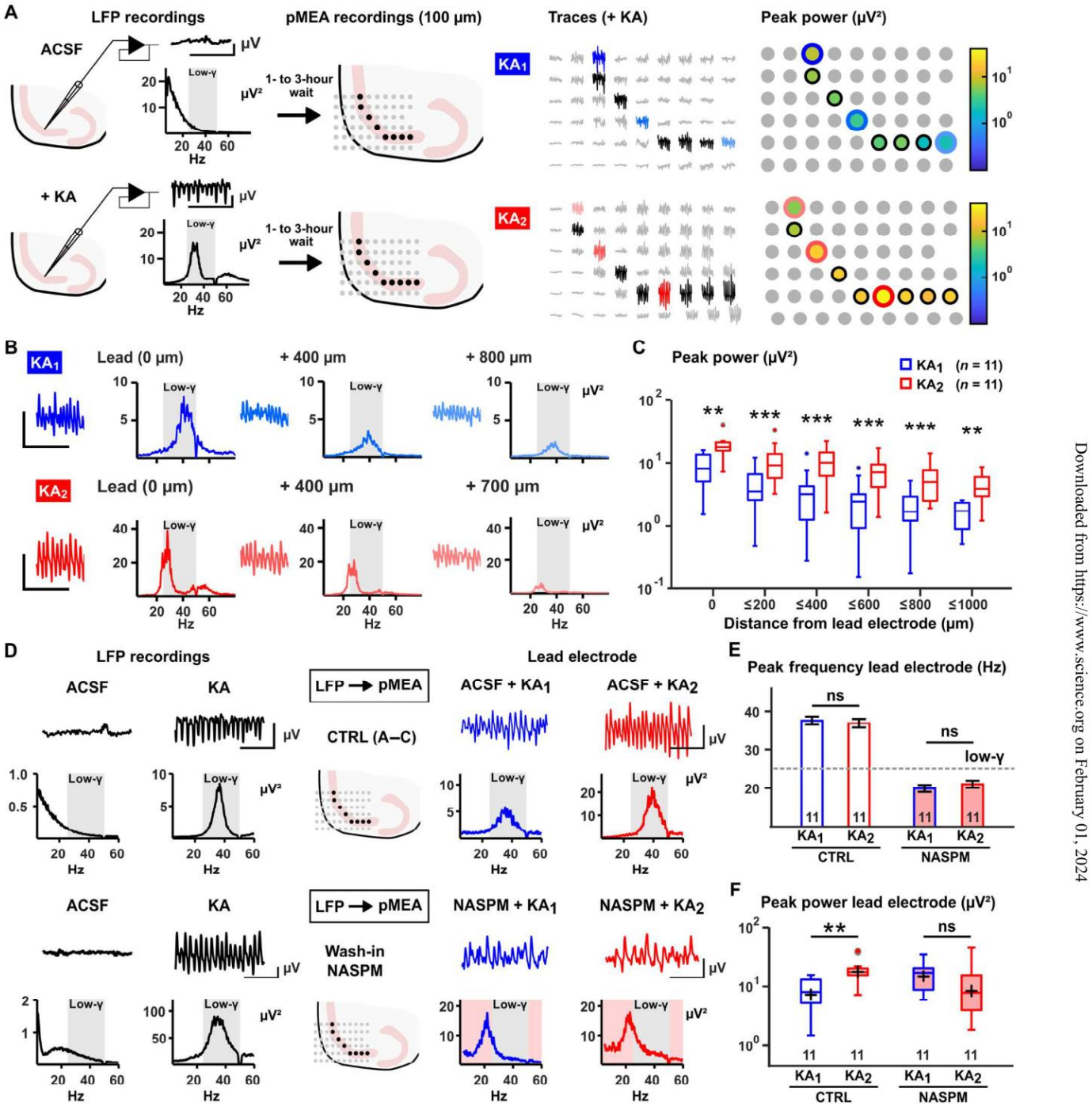

Fig. 3. Gamma potentiation is activity-dependent and expressed via CP-AMPARs. (**A**) Combined LFP-pMEA protocol. Left: In LFP recordings, slices are either left to rest ("ACSF") or treated with KA, yielding low gamma activity. After a waiting period (1 to 3 hours), slices are transferred to pMEAs with the selected electrodes (black) covering the pyramidal cell layer of CA3. KA is applied to untreated (KA_1, blue) and treated slices (KA_2, red), inducing gamma activity. Right: Heatmaps of peak gamma power over the selected electrodes. (**B**) Exemplary traces and PSDs taken from the experiments in (A). Recordings and corresponding PSDs from the electrodes with the highest power (lead electrode) are compared to those performed at distant sites, illustrating a decrease of peak power over distance. (**C**) Boxplots of peak power in both conditions ($n = 11$ slices tested each) pooled over the intralaminar distance from the lead electrode of each slice. Peak power is increased at all recording sites in treated slices (Mann-Whitney *U* test, $^{**}P < 0.01$ and $^{***}P < 0.001$. (**D**) CP-AMPARs express gamma potentiation. Slices were grouped as in (A) and either maintained in regular ACSF [control ("CTRL"), same dataset as in (A) to (C)] or treated with NASPM on pMEAs before application of KA. The PSD of the lead electrode was calculated for analysis. (**E**) Peak frequency of oscillations is reduced in pMEA "NASPM" conditions. Both treated and untreated slices display peak frequencies under 25 Hz after application of KA ($n = 11$ slices tested in all groups, ns denotes $P > 0.05$, Mann-Whitney *U* test). (**F**) In CTRL, peak power on the lead electrode is increased in pretreated slices but not in the NASPM condition ($n = 11$ slices tested each). $^{**}P < 0.01$ and ns (not significant), $P > 0.05$ (Mann-Whitney *U* test).

We developed a microcircuit model of CA3 low gamma oscillations incorporating biophysically constrained, multi-compartmental PYRs ($n = 20$) and PVIs ($n = 2$) and recorded the extracellular "LFP" nearby the pyramidal cell somata. A detailed description of PYR and PVI cellular properties [PVIs adapted from (*33*)] as well as the model's connectivity configuration can be found in Materials and Methods and table S1 to S3. In this model, a baseline period of low gamma activity can be reliably evoked by introducing an input population selectively targeting the PYR population for 1 s, mimicking our ex vivo approach using KA in a shorter timescale (Fig. 4A; "baseline" power: 29.27 [26.70, 30.42] μV^2). We then simulated LTP at either CI-AMPAR containing PYR-PYR (PYR-LTP) and CP-AMPAR containing PYR-PVI (PVI-LTP) synapses or both synapse types (PYR + PVI-LTP) by increasing their respective conductances by 50% and repeated the otherwise identical simulation (Fig. 4B). The PYR + PVI-LTP condition, which most closely approximated our ex vivo control experiments, reliably resulted in an increase of peak low gamma power by a factor of 2.5 to 3 (Fig. 4, C and D; "PYR + PVI-LTP" power: 89.53 [83.69, 98.01] μV^2, $n = 10$ trials; $P = 1.9 \times 10^{-3}$ versus baseline, Wilcoxon signed-rank test). When simulations were repeated under identical conditions, yet applying just PYR-LTP, we still observed a significant increase of peak power yet strongly reduced in magnitude (1.15-fold increase; Fig. 4, C and D; "PYR-LTP" power: 34.88 [28.94, 36.53] μV^2, $n = 10$, $P = 1.36 \times 10^{-2}$ vs. baseline, Wilcoxon signed-rank test). In contrast, applying just PVI-LTP to our simulations sufficiently reproduced the increase of power seen in the PYR + PVI-LTP condition, in some cases outperforming it and revealing no additive interaction in combining PYR-LTP with PVI-LTP (Fig. 4, C and D; "PVI-LTP" power: 89.74 [82.70, 93.21] μV^2, $n = 10$, $P = 0.55$ versus PYR + PVI-LTP, Wilcoxon signed-rank test).

Together, our simulations confirm a superior transfer of plasticity expressed at CP-AMPAR containing synapses, formed at PYR-PVI connections, to increasing low gamma power. This is in line with our initial pharmacological data and predicts a substantial contribution of PVI-specific LTP to ex vivo gamma potentiation.

Mechanisms: Gamma potentiation requires PV-specific mGluR5, mGluR1, PKC, and PKA activation

PVI-LTP obtained during gamma oscillations ex vivo can be prevented by unspecific concentrations (50 μM) of the group I mGluR

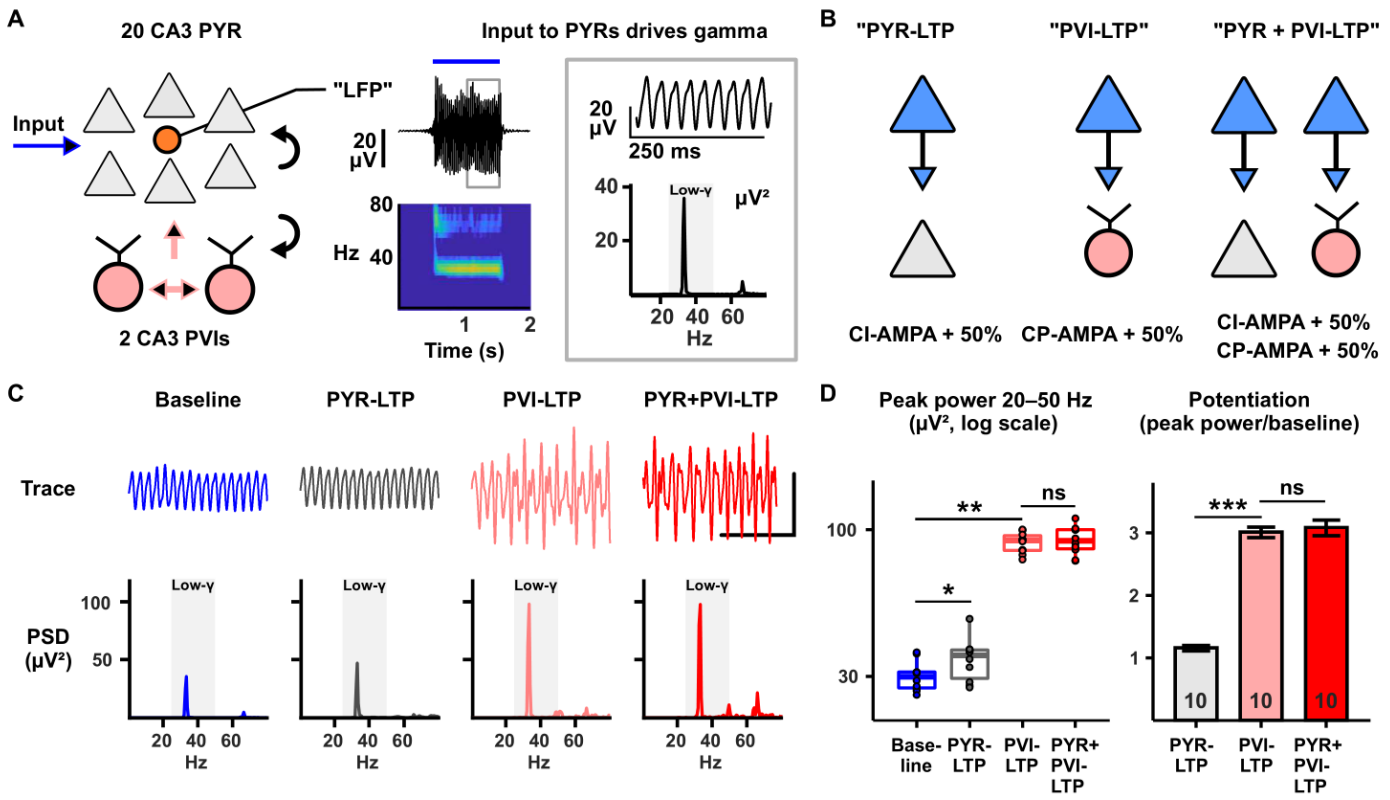

Fig. 4. A biophysically constrained microcircuit model of CA3 low gamma oscillations predicts superior transfer of PVI-LTP to the field potential. (**A**) Left: Microcircuit model of CA3 low gamma oscillations. A population of 20 CA3 pyramidal cells is activated by an input population (blue arrow). The PYR population forms glutamatergic synapses (black arrows) onto PYRs (CI-AMPA and NMDA conductances) and two CA3 PVIs (CP-AMPA and NMDA conductances). The PVIs form synapses onto each other and PYRs with GABAergic synapses (pink arrows). An LFP electrode (orange) is positioned nearby the PYR somata. Center: Exemplary trace of an LFP recording with pseudo-color plot of spectral power below. A 1-s stimulation via the input population produces an oscillation between 30 and 40 Hz. Right: Close-up view of the trace and PSD of the entire 2-s recording. Gray inset marks the low–gamma frequency range (25 to 50 Hz). (**B**) In silico plasticity paradigms. Glutamatergic synapses (blue) formed onto PYRs (gray) and/or PVIs (pink) are modified to simulate cell-type–specific plasticity. CI-AMPA and/or CP-AMPA conductances are increased by 50% for the respective paradigm. (**C**) Traces and power spectra for one exemplary simulation series. Inset denotes 50 μV/250 ms. (**D**) Summary statistics including data from 10 random simulation trials per case. Left: Boxplots of peak low gamma power for all conditions (*$P < 0.05$ and **$P < 0.01$, Wilcoxon signed-rank test). Right: Barplot of the magnitude of potentiation (***$P < 0.001$ and ns, $P > 0.05$, generalized linear model). Numbers in bars denote n = number of simulation trials.

antagonist MPEP (*29*). In an initial set of LFP experiments, we tested the effect of MPEP on gamma potentiation at a concentration specific to mGluR5 blockade (10 μM) as compared to co-application with D-AP5 and found that the magnitude of potentiation was robustly reduced by 50% in both cases (fig. S6). Because of a significant interaction of D-AP5 and MPEP in reducing the average peak frequency of oscillations (by roughly 2 Hz) and a modulating effect of both substances on peak gamma power, all subsequent experiments involving MPEP were performed in the presence of D-AP5 (50 μM).

We next generated mice undergoing Cre/loxp-dependent postnatal ablation of mGluR5 under the PV promoter (*34*), enabling us to assess the cell-type–specific contribution of mGluR5 to gamma potentiation. Slices obtained from these animals ("PV-mGluR5 KO") were compared to those obtained from littermates not expressing the loxp mutation ("PV-mGluR5 WT"), and gamma potentiation was quantified under application of MPEP [Fig. 5A; control (CTRL) versus MPEP]. In both genotypes, gamma oscillations were reliably induced with no apparent difference in peak gamma power between control conditions (Fig. 5B; power KA_1 WT CTRL: 2.38 [0.41, 4.27] μV^2, $n = 16$ versus KO CTRL: 4.00 [1.20, 34.57] μV^2, $n = 28$; $P = 0.40$, multiple Mann-Whitney *U* tests corrected by Holm). Regarding subsequent plasticity, MPEP again attenuated gamma potentiation by approximately 50% compared to wild-type (WT) control slices (Fig. 5, C and D; power KA_2/KA_1 WT CTRL: 2.31 ± 0.21, $n = 16$ versus WT MPEP: 1.49 ± 0.13, $n = 19$; $P = 6.7 \times 10^{-3}$, generalized linear model), confirming our initial results. In slices from PV-mGluR5 KO animals, on the other hand, gamma potentiation was already limited in control slices with no further reduction by MPEP (Fig. 5, C and D; power KA_2/KA_1 KO CTRL: 1.53 ± 0.12, $n = 28$ versus KO MPEP: 1.48 ± 0.11, $n = 19$; $P = 1.0$, generalized linear model). Gamma potentiation in both KO conditions was similarly reduced toward WT control slices as via conventional blockade by MPEP. Moreover, the slightly attenuating effect of MPEP on peak gamma frequency in KA_1 was not observed in KO slices (Fig. 5B). Therefore, the effects of mGluR5 on both gamma activity and subsequent gamma potentiation are mediated specifically via its native expression on PVIs.

mGluR1 coactivation may account for the remaining 50% of gamma potentiation, as both group I mGluRs similarly contribute to CP-AMPAR–mediated PVI-LTP by entraining PKC (*35*, *36*). Beyond such a canonical Gq pathway, PKA or activation of voltage-gated calcium channels (VGCCs), too, contribute to a diverse set of plasticity mechanisms putatively relevant to our paradigm. We tested these assumptions in a set of pharmacological LFP experiments in WT mice (Fig. 5, E to G). First, pre-application of the mGluR1 antagonist JNJ-16259685 (0.3 μM) reduced the magnitude of gamma potentiation toward control conditions [D-AP5, dimethyl sulfoxide (DMSO)] by roughly 50% (Fig. 5E; power KA_2/KA_1 CTRL: 2.13 ± 0.20, $n = 15$ versus JNJ: 1.45 ± 0.11, $n = 16$; $P = 8.1 \times 10^{-3}$, generalized linear model), comparable to sole application of MPEP (power KA_2/KA_1 MPEP: 1.36 ± 0.12, $n = 17$, $P = 1.9 \times 10^{-3}$ versus control, generalized linear model). When both substances were co-applied, we found no residual increase of peak power during the second induction period (MPEP + JNJ peak power KA_1: 34.16 [11.91, 67.14] μV^2 versus KA_2: 35.83 [15.90, 77.57] μV^2, $n = 23$; $P = 0.23$, Wilcoxon signed-rank test), confirming the additive requirement of group I mGluR activation in our protocol. In a second set of experiments, slices were first preincubated for 1 hour with either the PKC antagonist GF 109203X (GF; 3 μM), the PKA antagonist H-89 (3 μM), or a respective DMSO control (0.01%). Gamma oscillations could be reliably induced in all conditions, whereas oscillations induced following blockade of PKC, but not PKA, displayed a decreased initial peak gamma power (fig. S7). However, both preincubation with GF or H-89 entirely prevented gamma potentiation during the second induction period, demonstrating a requirement of both PKC and PKA activation for gamma potentiation (Fig. 5F; peak power control KA_1: 1.46 [0.77, 6.18] μV^2 versus KA_2: 3.22 [1.64, 9.98] μV^2, $n = 24$, $P = 1.2 \times 10^{-7}$; GF KA_1: 0.30 [0.14, 0.85] μV^2 versus KA_2: 0.41 [0.15, 1.02] μV^2, $n = 20$, $P = 0.18$; H-89 KA_1: 1.40 [0.30, 5.91] μV^2 versus KA_2: 1.58 [0.46, 2.68] μV^2, $n = 25$, $P = 0.62$, Wilcoxon signed-rank tests). Last, when either the L-type VGCC antagonist nifedipine (10 μM) or the T-type antagonist ML-218 (5 μM) was pre-applied, neither the induction of oscillations (fig. S7) nor their subsequent potentiation was significantly affected (Fig. 5G; power KA_2/KA_1 CTRL: 2.07 ± 0.26, $n = 8$; nifedipine: 2.25 ± 0.21, $n = 6$; ML-218: 1.82 ± 0.18, $n = 6$).

This completes a mechanistic profile of gamma potentiation nearly identical to known plasticity rules of glutamatergic LTP onto PVIs: Plasticity of gamma power is independent of NMDARs and VGCCs and instead requires CP-AMPARs, group I mGluRs and PKC (*36*) with an additional requirement of PKA activation. This profile is directly tied to PVIs by the requirement of their cell-type–specific expression of mGluR5.

DREADD-based metabotropic manipulation of PVIs determines the induction of gamma potentiation

Whereas our data from PV-mGluR5 KO slices accounted for the pharmacological effect of MPEP (50% of overall potentiation), open questions remained regarding the residual mGluR1 component and the locus of PKA action. We addressed this by applying two DREADD (Designer Receptors Exclusively Activated by Designer Drugs)-based strategies specific to PVIs and bred mice expressing either the hM4Di-DREADD (*37*) or the hemagglutinin-tagged hM3Dq-DREADD under the PV promoter alongside the fluorescent marker Ai9 ("PV-Ai9-hM4Di" and "PV-Ai9-hM3Dq" animals, respectively). In slices obtained from these animals, the respective DREADD pathway can be reliably activated with the selective compound deschloroclozapine (DCZ) (*38*).

Slices obtained from PV-Ai9-hM4Di animals were preincubated with DCZ (3 μM) before KA application, arguably reducing intracellular cyclic adenosine 3′,5′-monophosphate levels and downstream thereof PKA activity in PVIs (Fig. 6A) (*39*). To preclude nonspecific effects of DCZ, concomitant experiments were performed in mice lacking hM4Di expression ("PV-Ai9"). Neither in slices from PV-Ai9 nor PV-Ai9-hM4Di animals did DCZ affect the induction or maintenance of gamma activity during KA_1 in LFP recordings (Fig. 6B). However, in slices from PV-Ai9-hM4Di animals, subsequent gamma potentiation was completely prevented by DCZ (Fig. 6B; power KA_2/KA_1 PV-Ai9-hM4Di control: 2.37 ± 0.23, $n = 15$ versus DCZ: 1.09 ± 0.10, $n = 15$; $P = 3.4 \times 10^{-6}$, generalized linear model) but not in slices from PV-Ai9 animals (PV-Ai9 control: 2.24 ± 0.23, $n = 13$ versus DCZ: 2.25 ± 0.19, $n = 13$; $P = 0.96$, generalized linear model), indicating that the effect of PKA that we had observed in WT animals can be attributed to its specific activation in PVIs.

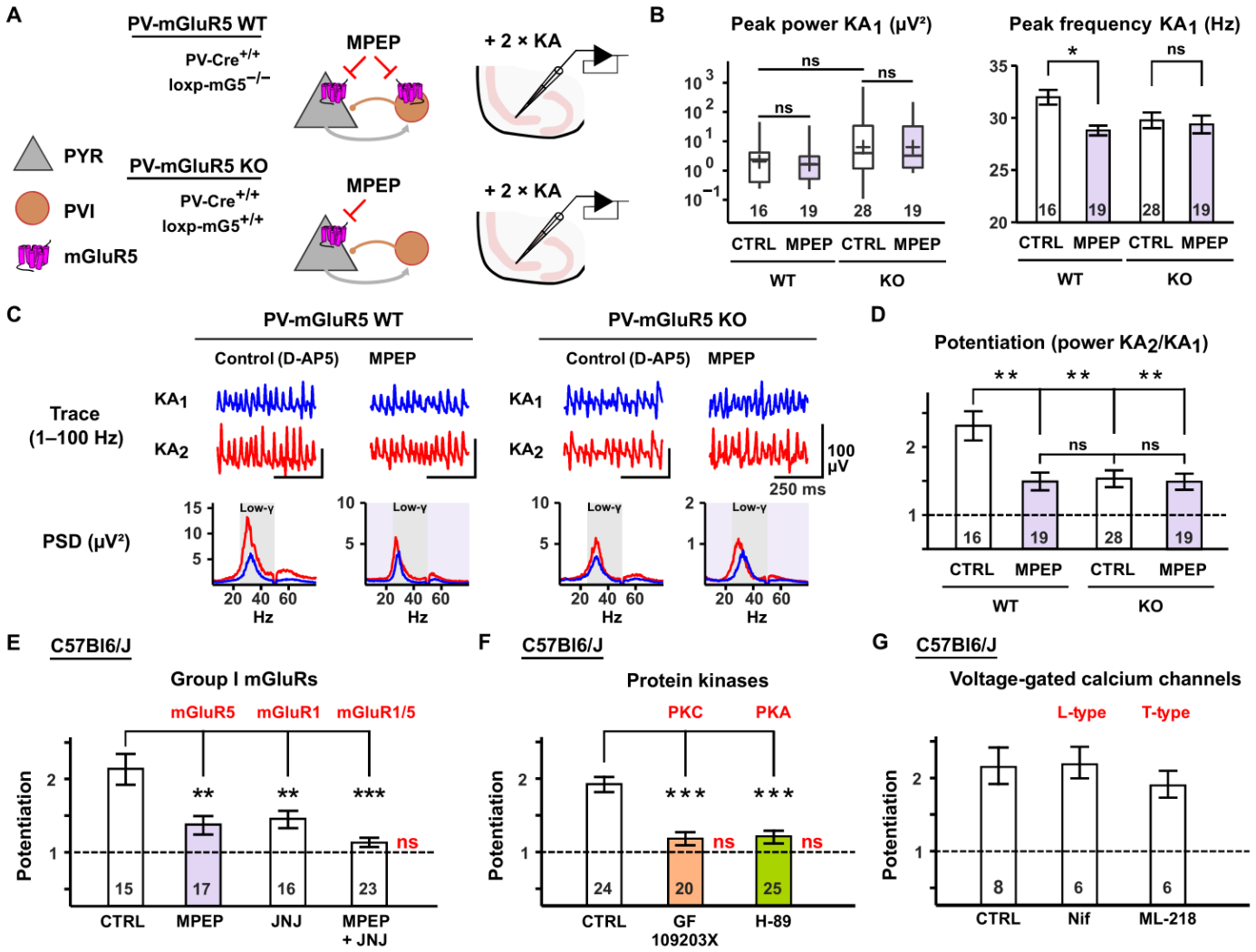

Fig. 5. Gamma potentiation requires PVI-specific mGluR5, mGluR1, PKC, and PKA activation. (**A**) Schematic of PV-mGluR5 experiments. Mice were bred PV-Cre$^{+/+}$ and either lacking (PV-mGluR5 WT) or expressing the loxp-mGluR5 mutation (PV-mGluR5 KO). MPEP blocks mGluR5. Slices from both genotypes were tested with the LFP paradigm. (**B**) Baseline values of KA-induced oscillations under application of MPEP. Left: No differences in peak gamma power ($P > 0.05$, Mann-Whitney U test). Right: MPEP reduces peak frequency in WT, but not KO slices [$^*P < 0.05$ and ns (not significant), $P > 0.05$, generalized linear model]. (**C**) Exemplary traces and PSDs of control and MPEP conditions in WT and KO slices during the first (KA_1) and second (KA_2) induction period, performed in D-AP5 (50 µM). (**D**) Average potentiation in (C). Potentiation is reduced in KO slices with no additional effect of MPEP ($^{**}P < 0.01$ and ns, $P > 0.05$, generalized linear model). (**E** to **G**) Pharmacological profile of gamma potentiation in slices from wild-type (WT; C57Bl6/J) animals. (E) Average potentiation under blockade of mGluR5 (MPEP, 50 µM), mGluR1 (JNJ-16259685, "JNJ," 0.3 µM), or both, performed in D-AP5 (50 µM) and dimethyl sulfoxide (DMSO; 0.01%). (F) Average potentiation under blockade of PKC (GF 109203X, 3 µM) or PKA (H-89, 3 µM), performed in DMSO (0.01%). (G) Average potentiation under blockade of L-type (nifedipine, "Nif," 10 µM) or T-type calcium channels (ML-218, 5 µM), performed in DMSO (0.01%). Red insets "ns" in barplots indicate no increase of peak power in KA_2 ($P > 0.05$, Wilcoxon signed-rank test; power KA_2 versus KA_1). Numbers in plots denote n = number of slices tested. (E) and (F) $^{***}P < 0.001$, $^{**}P < 0.01$, and ns, $P > 0.05$ (generalized linear model). Purple, orange, and green insets mark the application of MPEP, GF, and H-89, respectively.

In slices from PV-Ai9-hM3Dq animals, we applied the inverse strategy: If gamma potentiation is prevented by blockade of endogenous Gq receptors or PKC, activation of the xeno-receptor hM3Dq in PVIs may be sufficient to rescue blockade of the mGluRs, yet not blockade of downstream PKC (Fig. 6C). On the other hand, hM3Dq activation and subsequent depolarization of PVIs independent of PKC may itself drive PVI firing and thus induce gamma activity, as has been shown for optogenetic strategies (*9*). We tested these assumptions in multiple steps: First, when applied by itself, DCZ was insufficient to induce any form of network synchronization, highlighting the requirement of synaptic excitation we had demonstrated earlier (fig. S8). Second, when mGluR5 and mGluR1 were blocked with MPEP (10 µM) and JNJ-16259685 (0.3 µM), gamma potentiation was again prevented in slices from PV-Ai9-hM3Dq animals (power KA_2/KA_1 PV-Ai9-hM3Dq control: 2.31 ± 0.15, $n = 14$ versus MPEP + JNJ: 1.10 ± 0.16, $n = 12$; $P = 7 \times 10^{-5}$, generalized linear model). This was entirely rescued when DCZ was co-applied with KA, with the magnitude of potentiation nearly identical

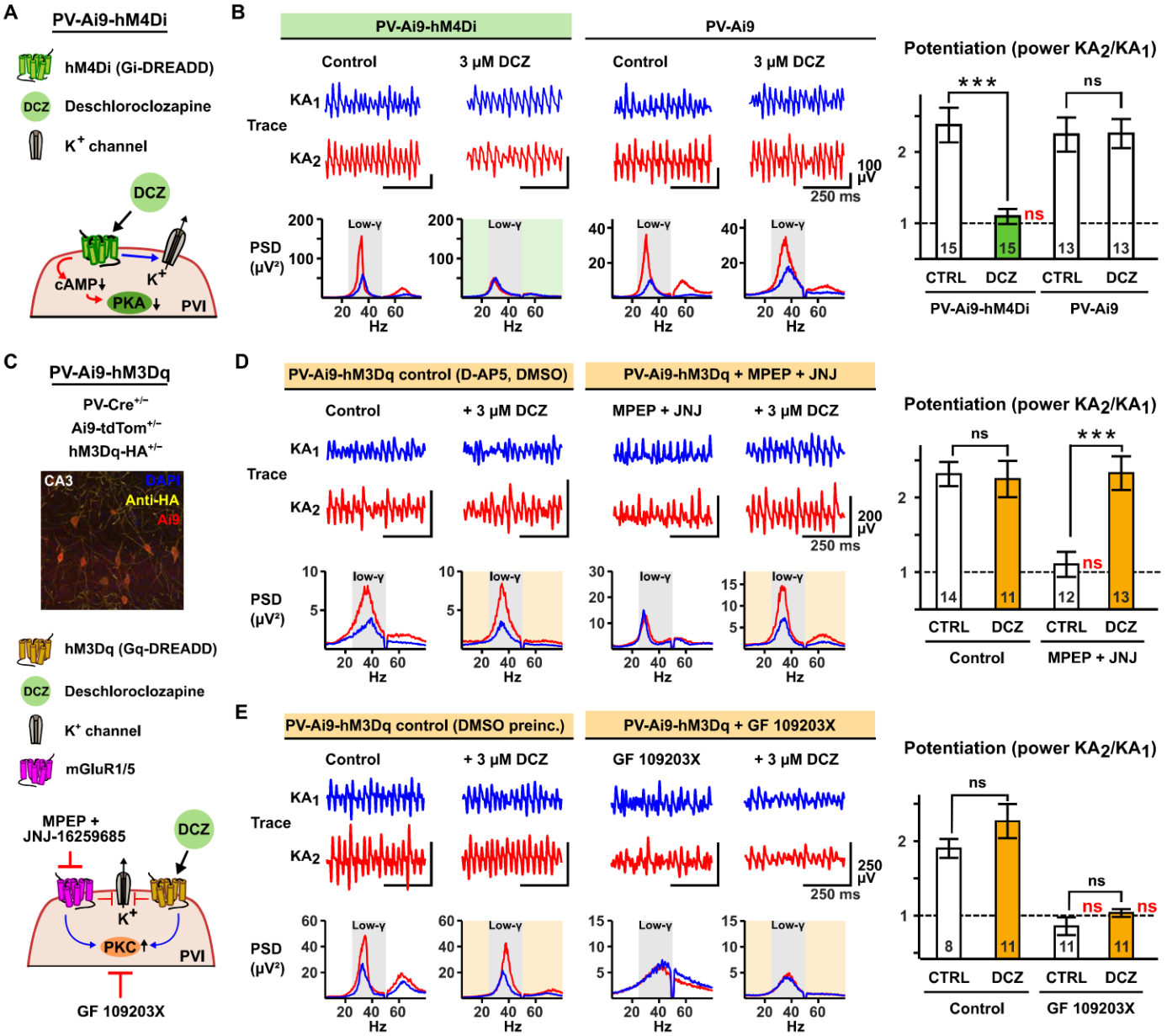

Fig. 6. PVI-specific DREADD manipulations determine the induction of gamma potentiation. (**A**) Schematic of PV-Ai9-hM4Di model. Deschloroclozapine (DCZ) activates hM4Di in PVIs, reducing intracellular cyclic adenosine 3′,5′-monophosphate (cAMP) and PKA activity and activating potassium channels. (**B**) DCZ prevents gamma potentiation in PV-Ai9-hM4Di slices. Left: Exemplary traces of Control and DCZ conditions for both genotypes during the first (KA_1) and second (KA_2) induction period. Corresponding PSDs below. Right: Barplot of average potentiation. (**C**) Above: Hemagglutinin (HA)–tagged hM3Dq is expressed in CA3 PVIs in PV-Ai9-hM3Dq animals (blue: DAPI, 4',6-diamidino-2-phenylindole, yellow: HA-tag from Cell Signaling Technology, 3724S, RRID:AB_1549585, ×30 magnification, red: Ai9). Below: Schematic of PV-Ai9-hM3Dq model and pharmacological approach. DCZ activates hM3Dq in PVIs, potassium channels inactivate, and PKC is activated. MPEP and JNJ-16259685 block mGluR1 and mGluR5, which target PKC. PKC is antagonized with GF 109203X (GF). (**D**) DCZ rescues gamma potentiation in PV-Ai9-hM3Dq slices after blockade of mGluR1 and mGluR5. Left: Exemplary traces of control and DCZ conditions with and without MPEP and JNJ application. Corresponding PSDs below. Experiments performed in D-AP5 (50 µM) and DMSO (0.01%). Right: Barplot of average potentiation. (**E**) DCZ-dependent rescue requires PKC. Left: Traces and PSDs as in (D) for control and under application of GF. Experiments performed after preincubation (preinc.) with DMSO (0.01%) for 1 hour. Right: Barplot of average potentiation. Red insets ns in potentiation plots mark groups with no significant increase of peak gamma power in KA_2 ($P > 0.05$, Wilcoxon signed-rank test; power KA_2 versus KA_1). Numbers in plots denote n = number of slices tested for each group. ***$P < 0.001$ and ns (not significant), $P > 0.05$ (generalized linear model). Colored insets in PSDs and barplots highlight the application of DCZ.

to control experiments (Fig. 6D; power KA_2/KA_1 PV-Ai9-hM3Dq MPEP + JNJ + DCZ: 2.32 ± 0.21, $n = 13$). Third, gamma potentiation was alternatively prevented by preincubation with GF (3 μM, DMSO). In this case, co-application of DCZ failed to reinstate gamma potentiation (Fig. 6E; power KA_2/KA_1 PV-Ai9-hM3Dq control: 1.93 ± 0.12, $n = 8$ versus GF: 0.86 ± 0.11, $n = 11$ and GF + DCZ: 1.04 ± 0.05, $n = 11$). Therefore, gamma potentiation can be entirely accounted for by metabotropic signaling in PVIs dependent on a Gq/PKC- and a Gi-sensitive PKA pathway, with DREADD-based strategies in PVIs functioning as effective on/off switches for network plasticity.

DISCUSSION

Studying the intersections of interneuron plasticity, oscillatory activity, and learning has emerged as a challenging yet promising field of research (*40*, *41*). Particularly in the hippocampus, the learning of context has been associated with changes of oscillation patterns: Following contextual fear conditioning in vivo, oscillations in the theta (*22*), gamma (*24*), and ripple (*22*, *23*) frequency bands undergo plastic changes in CA1. In CA3, theta-gamma coupling increases during successive trials of item-context association (*5*), and low gamma power increases following object learning, a change associated with improved assembly formation of CA3 pyramidal cells (*7*). Whereas targeted cell-type–specific manipulations have linked some of these phenomena to the activation of interneurons, an understanding of cause and effect of oscillatory plasticity remains elusive. In a first step, we previously demonstrated that hippocampal gamma activity itself induces plasticity of sharp-wave ripple complexes in vivo and ex vivo, which was associated with synaptic plasticity on both pyramidal cells and interneurons (*29*).

Here, we present a general plasticity mechanism intrinsic to hippocampal network oscillations by which gamma power is increased upon repeated exposure to an equal excitatory stimulus (Fig. 1). This plasticity mechanism, gamma potentiation, is embedded in a reciprocal relationship with PVI synaptic plasticity (Figs. 4 to 6): Evoking network activity in the gamma frequency range induces long-lasting plasticity onto PVIs (*29*, *35*, *36*, *42*), which, in turn, translates to subsequent network activity as a function of peak gamma power. Besides our PVI-specific interventions (Figs. 5 and 6), this is supported by two inductive approaches: Ex vivo, our data from CA1-Mini slices (fig. S3), a slice model of reduced recurrent excitation on pyramidal cells (*32*), demonstrate that local pyramidal cell–interneuron interactions are sufficient for the induction of oscillation plasticity. In silico, our microscale model of CA3 connectivity containing both PYR-PYR and PYR-PVI synapses further corroborates that plasticity at the PYR-PVI synapse critically outperforms plasticity at the PYR-PYR synapse in increasing low gamma power (Fig. 4). Intriguingly, PV-expressing interneurons themselves form diverse clusters of anatomically, molecularly, and physiologically distinct cell types (*43*, *44*), which differentially contribute to network oscillations (*45*) and therefore may share or delegate contributions to their respective plasticity. Our modeling data assume a fast-spiking, basket cell–type morphology and predicts effective plasticity of gamma oscillations (Fig. 4). This is in line with findings demonstrating a heightened activity of fast-spiking, PV-expressing interneurons during gamma activity in vivo (*45*) and ex vivo (*46*). Once active, fast-spiking basket and axo-axonic cells exert powerful inhibition over the local pyramidal cell population, e.g. during KA-evoked gamma oscillations (*18*), making them likely candidates for mediating gamma potentiation. However, we cannot exclude additional contributions of other interneuron subtypes: Dendrite-targeting, somatostatin (SOM)–positive interneurons substantially contribute to gamma oscillations in the hippocampus and neocortex (*47*–*50*). The transgenic lines used in this study are unlikely to target large populations of SOM-positive interneurons (*51*), yet coexpression of SOM and PV has been observed specifically in oriens–lacunosum moleculare (O-LM) interneurons, a cell-type particularly active during theta-nested gamma oscillations in vivo (*52*) and ex vivo (*53*). O-LM interneurons exhibit synaptic and intrinsic plasticity following theta-rate stimulation patterns that obey a similar profile as gamma plasticity, requiring CP-AMPARs and mGluR1 (*54*). Other than in PVIs, O-LM output is primarily modulated by theta rather than gamma oscillations (*45*, *46*), making a direct overall contribution of O-LMs to gamma plasticity unlikely, yet predicting an indirect contribution via the modulation of concomitant theta states and/or in supporting long-range synchronization of gamma-coherent assemblies (*55*). In summary, our study provides a first step in identifying cell-type–specific cell-to-network plasticity of gamma oscillations and motivates more granular investigations of interneuron subtype-specific contributions. Within this study, and given our previous findings for gamma-induced plasticity (*29*), plasticity at the CA3 pyramidal cell–PV basket cell synapse is both sufficient and mandatory to modulate the gamma rhythm.

We investigate this relationship mechanistically using a robust (fig. S1) ex vivo paradigm, permitting the analysis of gamma activation states under maximal experimental control and circumventing confounders of in vivo oscillation power such as running speed, respiration rate, or cross-frequency coupling (*56*, *57*), as well as spatial limitations concerning the origin (*6*, *7*, *58*) and focality (*59*) of oscillations. In the approach used here, gamma activity is gradually introduced to the isolated hippocampal network and tapered under constant control of external excitation via defined application of KA. This allows the precise mechanistic dissection of plasticity rules with pharmacological and genetic tools. Plasticity in our protocol occurs in an activity-dependent manner and already has effect after short- to intermediate-term delays in subsequent episodes (1 to 3 hours; fig. S2), predating alterations in transcriptional and anatomical PVI properties (*26*, *27*) and making changes of transmembrane conductances the most likely mechanism. Although KA-induced ex vivo gamma power correlates with its in vivo counterpart and behavioral performance (*60*), our conclusions on plasticity remain to be confirmed in vivo. Translating our ex vivo model of gamma potentiation to the ground-truth in vivo gamma rhythm and possible effects on behavior will require temporally precise synapse-specific tools (*61*) and an experimental environment closely controlling the emergence and reinstatement of gamma oscillations on short timescales.

The specific synaptic recruitment of PVIs via CP-AMPARs is the decisive determinant in procuring and expressing gamma potentiation, as demonstrated by both our ex vivo and in silico data sets (Figs. 2 to 4). Through their rapid activation and decay kinetics, CP-AMPARs enable the temporally precise integration of converging inputs on and co-activation of PVIs (*62*, *63*), which, as our data suggest, is mandatory for the induction of >30 Hz oscillations themselves. Therefore, increased CP-AMPAR conductance is a convincing mechanistic candidate underlying gamma potentiation. Given our previous findings for sharp-wave ripple–associated plasticity (*29*)

and present modeling predictions, this points to the induction of synaptic glutamatergic LTP onto PVIs (PVI-LTP) as the primary facilitator of gamma potentiation. The specific requirement of CP-AMPAR activation reported here separates our protocol from previous optogenetic or chemogenetic manipulations of network plasticity in vivo purportedly relying on the isolated activation of PVIs, but which cannot target or exclude coincident glutamatergic drive (*22*, *23*, *64*). Whether downstream effectors of PVI-LTP such as intrinsic membrane excitability (*65*) and/or an increased transmission at GABAergic output synapses (*66*–*68*) similarly contribute to the resulting field potential remains to be determined.

Like PVI-LTP in the dentate gyrus and gamma-mediated PVI-LTP in CA3 (*29*, *36*), gamma potentiation is independent of NMDAR activation and instead requires group I mGluRs and downstream PKC, in line with a canonical Gq cascade. We tie this to PVIs with two genetic strategies: the conditional ablation of mGluR5 in PVIs and the PV-specific Gq-DREADD activation. Moreover, both our pharmacological and chemogenetic evidence using hM4Di activation suggest the requirement of a second pathway recruiting PKA (Figs. 5 and 6). A dual requirement of two kinase pathways may act as a gating mechanism for network plasticity (*69*): If gamma oscillations were both induced and amplified via CP-AMPAR activation alone, then local networks would be exposed to runoff dynamics in which oscillation power continuously increases. Expanding such a model by a prerequisite of metabotropic costimulation stabilizes network dynamics and discriminates between sub- and supra-critical stimuli to the hippocampal network during learning. This mirrors a recent proposal of three-factor plasticity in interneurons (*41*), in which mGluRs function as effective detectors of converging activity during oscillations (*70*), and putative activators of PKA (e.g., dopamine and noradrenaline) encode novelty (*71*, *72*). Whether the Gq/PKC and PKA pathways effectuate plasticity independently, converge with each other, or interact via cross-talk (*73*) remains beyond the scope of this study yet may provide crucial insights into how targeting PVI-LTP translates into network oscillations.

The mechanistic composition of gamma potentiation provides a promising framework for the understanding and potential treatment of neuropsychiatric diseases associated with aberrant network oscillations. The PV-mGluR5 knockout model used here (Fig. 5) displays disrupted hippocampus-dependent behavior (*34*), establishing a direct link between insufficient ex vivo gamma plasticity and phenotypes of neurodevelopmental disease. mGluR5 activity is down-regulated in postmortem tissue of patients with schizophrenia (*74*), and, conversely, positive allosteric modulation of mGluR5 has been successfully targeted in animal models of schizophrenia (*75*), a disease etiologically tied to PVI dysfunction and disrupted network oscillations. The link between PVI plasticity, gamma potentiation, and disease is further supported by a string of recent preclinical studies successfully treating symptoms of neurodevelopmental disorders: Similar to the bimodal control of PVI-dependent DREADD manipulations over gamma potentiation (Fig. 6), hM4Di inhibition of PVIs induces deficits of cognitive performance (*23*, *76*), while PVI-specific hM3Dq activation rescues such deficits in animal models of schizophrenia and disruptions in network oscillations (*76*–*78*). Further, the physiological induction of gamma oscillations via sensory stimuli (gamma entrainment using sensory stimuli) is itself effective in treating animals models of Alzheimer's disease (*79*) and schizophrenia (*80*), whereas the exact mechanism underlying these treatments has been recently contested (*81*). An inert, bidirectional cortical mechanism of gamma rhythm plasticity via synaptic plasticity of PVIs may therefore lie at the core of future clinical interventions and serve to inform therapeutic strategies.

MATERIALS AND METHODS

Animals

Adolescent (P45 to P70) male C57Bl6/J mice (the Jackson Laboratory, RRID:IMSR_JAX:000664) were used for experiments in WT animals. For experiments involving cell-type–specific manipulations of PVIs, PV-Cre animals (the Jackson Laboratory, RRID:IMSR_JAX:017320) were crossbred with either Ai9 (the Jackson Laboratory, RRID:IMSR_JAX:007909), loxp-mG5 (RRID:IMSR_JAX:028626, provided by P. Wulff), Flex-hM4Di [Rosa26-FLEX-hM4D (MGI:7528984); see (*37*); provided by B. Rost], or loxp-hM3Dq (the Jackson Laboratory, RRID:IMSR_JAX:026220) animals, and experiments were performed from adolescent (P45 to P70) offspring of both sexes. Animal procedures were conducted in accordance with the guidelines of the European Communities Council and the institutional guidelines approved by the Berlin Animal Ethics Committee (Landesamt für Gesundheit und Soziales Berlin, T0045/15 and T-CH0014/23). All efforts were made to minimize animal suffering and to reduce the number of animals used.

Slice preparation

Mice were deeply anesthetized with isoflurane and decapitated. Their brains were removed and immersed in ice-cold sucrose solution (75 mM sucrose, 87 mM NaCl, 2.5 mM KCl, 25 mM $NaHCO_3$, 1.25 mM NaH_2PO_4, 3 mM $MgCl_2$, 0.5 mM $CaCl_2$, and 10 mM glucose) saturated with carbogen gas (95% O_2/5% CO_2). The brain was cut into 400-μm-thick horizontal slices containing the hippocampal formation with a vibratome (Leica VT 1200S, Leica Biosystems, Germany). Slices were subsequently transferred to interface-type recording chambers perfused with ACSF (129 mM NaCl, 3 mM KCl, 21 mM $NaHCO_3$, 1.25 mM NaH_2PO_4, 1.8 mM $MgSO_4$, 1.6 mM $CaCl_2$, and 10 mM glucose; 32° to 34°C; flow rate, 1.5 ml/min) saturated with carbogen and left to incubate for 2 hours before recordings. To obtain CA1-Mini slices, slices were cut in the interface chamber shortly after preparation with a surgical blade to separate CA1 from CA2 and the subiculum under consideration of CA1 dendrite morphology.

For experiments involving pharmacological agents, drugs were added to the ACSF at least 1 hour before recording. In experiments involving GF or H-89, slices were first left to recover for 1 hour after slicing in a submerged-type beaker at 34°C containing the respective substance diluted at its final concentration in sucrose solution before being transferred to interface chambers. Corresponding control experiments were performed in the presence of 0.01% DMSO in the beaker.

Electrophysiology

LFP recordings

LFPs were recorded from stratum pyramidale of hippocampal CA3 (and/or CA1 when indicated) with glass pipettes filled with ACSF (1 to 10 megaohms). Recordings were amplified by EXB-EXT-02B amplifiers (npi Electronic, Germany), low-pass–filtered at 1 kHz, sampled at 5 kHz by a CED 1401 AD-converter [Cambridge Electronic

Design (CED), UK] and saved to disk via Spike2 software (CED, UK, RRID:SCR_000903). Following an initial 30-min period of recording baseline activity, network oscillations were induced in one or two separate periods by bath application of 150 to 400 nM KA over a period of 30 min with a 60-min "resting" interval between both application periods. In a subset of experiments, the resting period was extended to 3 hours. After the second application of KA, slices rested for up to 1 hour before terminating the recording. Pipette resistances were monitored before and after recordings with an EXB-REL08B electrode resistance meter (npi), and recordings were discarded if resistances deviated >10%.

pMEA recordings

pMEA recordings were performed on a MEA2100-HS(2x)60 system (Multichannel Systems) using 60pMEA100/30iR-Ti pMEAs (Multichannel Systems). Slices were transferred from their previous interface storage to the pMEA and carefully placed above the electrodes with the aim of maximal coverage of the pyramidal cell layer (identified visually under magnification and confirmed by the positive polarity of spontaneous sharp-wave ripple complexes). Slices were kept in place via a continuous negative pressure supplied by a constant vacuum pump (CVP-230 V, Multichannel Systems) and allowed to rest in position for 15 to 20 min before recording. After a brief recording of baseline activity confirming the absence of ambient gamma oscillations, oscillations were induced via bath application of 200 nM KA (flow rate of 10 ml/min, 32° to 34°C). The dual headstage configuration of the MEA2100-HS(2x)60 system allowed us to test individual treated and untreated slices in time control.

Drugs

KA (Tocris), D-AP5 (Cayman Chemicals), MPEP (Cayman Chemicals), JNJ-16259685 (Tocris, JNJ), GYKI-53655 (hellobio), NASPM (Cayman Chemicals, NASPM), GF(Tocris), H-89 (Cayman Chemicals), UBP-302 (Tocris, UBP), DCZ-dihydrochloride (Cayman Chemicals), nifedipine (Tocris), and ML-218 (Tocris) were dissolved in either deionized water or DMSO (JNJ, GF, H-89, UBP, nifedipine, and ML-218) and stored in aliquots at −20°C. Aliquots were dissolved in ACSF immediately before the experiments. Experiments involving nifedipine were conducted in the dark.

Computational modeling

Model implementation and availability

We conducted all modeling simulations using the NEURON (NEURON v7.6, RRID:SCR_005393) Simulator (*82*) on a High-Performance Computing Cluster with 111 CPU cores, running on a 64-bit CentOS Linux operating system. The source code and datasets used to generate Fig. 4 are publicly available; please refer to the Data and materials availability statement for the link.

PV basket cell model

The multi-compartmental models of the CA3 PV basket cells (PVIs) ($n = 2$) used in this study were adapted from previously published work (*33*). These models have been extensively validated against experimental data and have been shown to accurately capture the intrinsic, active, and morphological properties of PVIs (for more detailed information, please refer to the previous publication).

Pyramidal neuron model

The CA3 pyramidal neuron cell model (PYR) was simulated on the basis of the Hodgkin-Huxley formalism and consists of six compartments: one soma and five dendrites. The model simulates one proximal and two distal apical dendrites, as well as two basal dendrites. It includes a Ca^{2+} pump and buffering mechanism, Ca^{2+}-activated slow AHP and medium AHP potassium (K^+) currents, an HVA L-type calcium (Ca^{2+}) current, an HVA R-type Ca^{2+} current, an LVA T-type Ca^{2+} current, an h current, a fast sodium (Na^+) current, a delayed rectifier K^+ current, a slowly inactivating K^+ M-type current, and a fast inactivating K^+ A-type current. The current mechanisms were distributed in a nonuniform way along the somatodendritic compartments (for detailed information about the passive and active properties of the PYR model, including conductance values, please see table S1). The active and passive properties of the PYR model were validated against in vitro experimental data from CA3 recordings (*83*). This was done to ensure that the in silico model reproduces the electrophysiological profile of the in vitro CA3 pyramidal cells (for more detailed information, please see table S2).

Synaptic properties

The PYR models were equipped with CI-AMPA, NMDA, and γ-aminobutyric acid type A ($GABA_A$) synapses, while the PV BC models had CP-AMPA, NMDA, $GABA_A$, and autaptic $GABA_A$ synapses. The synaptic properties were validated against previously published data (*84*–*86*). The conductance values for each synapse type are provided in table S3.

Plasticity protocols

The plasticity simulations were performed by increasing the conductance values of different types of synapses in the microcircuit model. Specifically, the three conditions tested were PYR plasticity (PYR-LTP), which involved a 50% increase in the CI-AMPA conductance value of PYR to PYR connections, PVI plasticity (PVI-LTP), which involved a 50% increase in the CP-AMPA conductance value of PYR to PVI connections, and PYR and PVI plasticity (PYR + PVI-LTP), which involved a 50% increase in both the CI-AMPA and CP-AMPA conductance values of PYR to PYR and PYR to PVI connections (see also table S3).

Microcircuit configuration

The biologically constrained CA3 microcircuit model comprised 22 neurons, specifically 20 PYRs and 2 PVIs. In each random simulation trial ($n = 10$), each PYR contacted up to four other PYRs with one CI-AMPA and one NMDA synapse activation per contact (convergence = 1). On the other hand, every PVI received synaptic input (convergence = 1) from five different PYRs in each simulation trial. In addition, every PYR received one feedback inhibitory GABAergic input from each PVI per simulation trial. Each of the two PVIs formed four GABAergic synapses per simulation trial and was self-inhibited through autapses. To record the LFP, an in silico electrode was simulated on the basis of NEURON's extracellular function [based on (*87*)]. The electrode was placed close to the PYR somata and remained in the same position throughout the simulation trials. The sampling frequency was set at 10 kHz. For simplicity reasons, other inhibitory interneuron types, such as dendrite-targeting interneurons, and network properties, such as gap junctions, were not simulated as they were not relevant to the experimental observations of this study.

Inputs and simulation

The input was modeled as an artificial presynaptic population using NEURON's NetStim function (interval = 30, number = 30). The input targeted only the PYR population of the microcircuit for 1 s, and three input synapses were activated in every pyramidal cell (see table S3), mimicking the experimental protocol of KA activation primarily in the pyramidal cells. In addition, both pyramidal cells

and PVI populations received the same excitatory subthreshold background fluctuation input (subthreshold noise). For every case (including baseline, PYR-LTP, PVI-LTP, or PYR + PVI-LTP), we ran the microcircuit for 10 random trials. In every trial, the number of total synaptic contacts and the connectivity ratios remained identical, but different random neurons were connected to different random neurons. To capture any variability related to morphological features, synapses were allocated in different random dendrites and locations across the selected dendrites in every trial. The recording time was 2 s for every simulation trial.

Data analysis and statistics

LFP recordings

Recordings were band-pass–filtered (1 to 100 Hz, 12 pole IIR digital filter) and band-stop–filtered (49 to 51 Hz, 12 pole IIR digital filter). Power spectra were calculated every 30 s throughout the recording in each recorded slice individually. Peak power and peak frequency were determined offline by using custom-made MATLAB scripts and visualized as time-power and time-frequency plots, respectively. Slices were excluded from analysis if (i) they only displayed synchronous activity for an interval shorter than 10 min or during only one induction period or (ii) network activity was instable, e.g., peak power would intermittently decrease during KA application by >10%.

For each included slice, a 10-min time window was detected corresponding to maximal peak power in the first induction period. Peak power and frequency were extracted from an additional 10-min power spectral density obtained with MATLABs "pwelch" function (0.34-Hz resolution) and auto-/cross-correlograms obtained over the same interval with the "xcorr" function. For experiments investigating network activity in two separate episodes of KA application, the identical analysis was performed twice in time control to the first application period.

pMEA recordings

Recordings were preprocessed, and peak power and frequency values as well as cross-correlograms for each channel were obtained identically to LFP recordings. Channels included in subsequent analysis were identified by their positioning below the pyramidal cell layer, marked as nodes in relation to their position on the pMEA that were connected via edges to the respectively adjacent selected electrodes (MATLAB "digraph" function). For each individual recording, a lead electrode, corresponding to the highest peak power value determined, was identified. Intralaminar distances to this electrode were calculated with the "shortestpath" MATLAB function.

Simulation data

Data were band-pass– and band-stop–filtered as LFP recordings. Power spectra were obtained from the entire 2-s recording with the same parameters as LFP recordings and peak power values extracted between 20 and 40 Hz.

Statistical analysis

Statistical analysis and data visualization were performed in R 4.1.3. As absolute peak spectral power is non-normally distributed in our datasets and in single LFP recordings is highly dependent on the intralaminar location of the recording site (compare Fig. 3 and fig. S4), all testing on raw power data was performed nonparametrically using the Mann-Whitney *U* test (independent samples) or Wilcoxon signed-rank test (dependent samples). Power data are presented as median [first quartile, third quartile] and visualized as boxplots (crosses in boxplots denote the mean). Other positive-only, skewed datasets (i.e., peak frequency of network oscillations or potentiation of peak power; compare fig. S1) were fitted with a generalized linear model assuming a log-linked gamma distribution (*88*) to account for zero truncation. *T* statistics and *P* values for group comparisons were subsequently obtained from the estimated marginal means ("emmeans" package, https://cran.r-project.org/web/packages/emmeans/index.html). Non-power data are presented as means ± SEM and visualized as barplots. Numbers in barplots or below boxplots denote the sample size with *n* referring to the number of slices tested or simulation trials run, respectively. Significance was set to an α level of 0.05. *P* values obtained from multiple group comparisons were corrected with the Bonferroni-Holm method.

Supplementary Materials

This PDF file includes:

Figs. S1 to S8
Tables S1 to S3

REFERENCES AND NOTES

1. W. Singer, Neuronal oscillations: Unavoidable and useful? *Eur. J. Neurosci.* **48**, 2389–2398 (2018).
2. Z. Nadasdy, D. H. P. Howell, A. Török, T. P. Nguyen, J. Y. Shen, D. E. Briggs, P. N. Modur, R. J. Buchanan, Phase coding of spatial representations in the human entorhinal cortex. *Sci. Adv.* **8**, eabm6081 (2022).
3. G. Buzsáki, A. Draguhn, Neuronal oscillations in cortical networks. *Science* **304**, 1926–1929 (2004).
4. G. Buzsáki, *Rhythms of the Brain* (Oxford Univ. Press, 2006).
5. A. B. L. Tort, R. W. Komorowski, J. R. Manns, N. J. Kopell, H. Eichenbaum, Theta–gamma coupling increases during the learning of item–context associations. *Proc. Natl. Acad. Sci. U.S.A.* **106**, 20942–20947 (2009).
6. V. Lopes-dos-Santos, G. M. van de Ven, A. Morley, S. Trouche, N. Campo-Urriza, D. Dupret, Parsing hippocampal theta oscillations by nested spectral components during spatial exploration and memory-guided behavior. *Neuron* **100**, 940–952.e7 (2018).
7. A. Fernández-Ruiz, A. Oliva, M. Soula, F. Rocha-Almeida, G. A. Nagy, G. Martin-Vazquez, G. Buzsáki, Gamma rhythm communication between entorhinal cortex and dentate gyrus neuronal assemblies. *Science* **372**, eabf3119 (2021).
8. P. J. Uhlhaas, W. Singer, Neural synchrony in brain disorders: Relevance for cognitive dysfunctions and pathophysiology. *Neuron* **52**, 155–168 (2006).
9. J. A. Cardin, M. Carlén, K. Meletis, U. Knoblich, F. Zhang, K. Deisseroth, L.-H. Tsai, C. I. Moore, Driving fast-spiking cells induces gamma rhythm and controls sensory responses. *Nature* **459**, 663–667 (2009).
10. V. S. Sohal, F. Zhang, O. Yizhar, K. Deisseroth, Parvalbumin neurons and gamma rhythms enhance cortical circuit performance. *Nature* **459**, 698–702 (2009).
11. K. K. A. Cho, R. Hoch, A. T. Lee, T. Patel, J. L. R. Rubenstein, V. S. Sohal, Gamma rhythms link prefrontal interneuron dysfunction with cognitive inflexibility in Dlx5/6$^{+/-}$ mice. *Neuron* **85**, 1332–1343 (2015).
12. G. Buzsáki, X.-J. Wang, Mechanisms of gamma oscillations. *Annu. Rev. Neurosci.* **35**, 203–225 (2012).
13. L. L. Colgin, Rhythms of the hippocampal network. *Nat. Rev. Neurosci.* **17**, 239–249 (2016).
14. M. Bartos, I. Vida, P. Jonas, Synaptic mechanisms of synchronized gamma oscillations in inhibitory interneuron networks. *Nat. Rev. Neurosci.* **8**, 45–56 (2007).
15. X.-J. Wang, G. Buzsáki, Gamma oscillation by synaptic inhibition in a hippocampal interneuronal network model. *J. Neurosci.* **16**, 6402–6413 (1996).
16. E. O. Mann, J. M. Suckling, N. Hajos, S. A. Greenfield, O. Paulsen, Perisomatic feedback inhibition underlies cholinergically induced fast network oscillations in the rat hippocampus in vitro. *Neuron* **45**, 105–117 (2005).
17. B. V. Atallah, M. Scanziani, Instantaneous modulation of gamma oscillation frequency by balancing excitation with inhibition. *Neuron* **62**, 566–577 (2009).
18. T. Dugladze, D. Schmitz, M. A. Whittington, I. Vida, T. Gloveli, Segregation of axonal and somatic activity during fast network oscillations. *Science* **336**, 1458–1461 (2012).
19. H. Hu, J. Gan, P. Jonas, Fast-spiking, parvalbumin GABAergic interneurons: From cellular design to microcircuit function. *Science* **345**, 1255263 (2014).
20. E. C. Fuchs, H. Doheny, H. Faulkner, A. Caputi, R. D. Traub, A. Bibbig, N. Kopell, M. A. Whittington, H. Monyer, Genetically altered AMPA-type glutamate receptor kinetics in interneurons disrupt long-range synchrony of gamma oscillation. *Proc. Natl. Acad. Sci. U.S.A.* **98**, 3571–3576 (2001).

21. E. C. Fuchs, A. R. Zivkovic, M. O. Cunningham, S. Middleton, F. E. N. LeBeau, D. M. Bannerman, A. Rozov, M. A. Whittington, R. D. Traub, J. N. P. Rawlins, H. Monyer, Recruitment of parvalbumin-positive interneurons determines hippocampal function and associated behavior. *Neuron* **53**, 591–604 (2007).
22. N. Ognjanovski, S. Schaeffer, J. Wu, S. Mofakham, D. Maruyama, M. Zochowski, S. J. Aton, Parvalbumin-expressing interneurons coordinate hippocampal network dynamics required for memory consolidation. *Nat. Commun.* **8**, 15039 (2017).
23. F. Xia, B. A. Richards, M. M. Tran, S. A. Josselyn, K. Takehara-Nishiuchi, P. W. Frankland, Parvalbumin-positive interneurons mediate neocortical-hippocampal interactions that are necessary for memory consolidation. *eLife* **6**, e27868 (2017).
24. X. He, J. Li, G. Zhou, J. Yang, S. McKenzie, Y. Li, W. Li, J. Yu, Y. Wang, J. Qu, Z. Wu, H. Hu, S. Duan, H. Ma, Gating of hippocampal rhythms and memory by synaptic plasticity in inhibitory interneurons. *Neuron* **109**, 1013–1028.e9 (2021).
25. A. I. Ramsaran, Y. Wang, A. Golbabaei, S. Aleshin, M. L. de Snoo, B. A. Yeung, A. J. Rashid, A. Awasthi, J. Lau, L. M. Tran, S. Y. Ko, A. Abegg, L. C. Duan, C. McKenzie, J. Gallucci, M. Ahmed, R. Kaushik, A. Dityatev, S. A. Josselyn, P. W. Frankland, A shift in the mechanisms controlling hippocampal engram formation during brain maturation. *Science* **380**, 543–551 (2023).
26. F. Donato, S. B. Rompani, P. Caroni, Parvalbumin-expressing basket-cell network plasticity induced by experience regulates adult learning. *Nature* **504**, 272–276 (2013).
27. N. Dehorter, G. Ciceri, G. Bartolini, L. Lim, I. del Pino, O. Marín, Tuning of fast-spiking interneuron properties by an activity-dependent transcriptional switch. *Science* **349**, 1216–1220 (2015).
28. D. M. Kullmann, K. P. Lamsa, Long-term synaptic plasticity in hippocampal interneurons. *Nat. Rev. Neurosci.* **8**, 687–699 (2007).
29. S. Zarnadze, P. Bäuerle, J. Santos-Torres, C. Böhm, D. Schmitz, J. R. Geiger, T. Dugladze, T. Gloveli, Cell-specific synaptic plasticity induced by network oscillations. *eLife* **5**, e14912 (2016).
30. R. Zemankovics, J. M. Veres, I. Oren, N. Hájos, Feedforward inhibition underlies the propagation of cholinergically induced gamma oscillations from hippocampal CA3 to CA1. *J. Neurosci.* **33**, 12337–12351 (2013).
31. R. D. Traub, M. O. Cunningham, T. Gloveli, F. E. N. LeBeau, A. Bibbig, E. H. Buhl, M. A. Whittington, GABA-enhanced collective behavior in neuronal axons underlies persistent gamma-frequency oscillations. *Proc. Natl. Acad. Sci. U.S.A.* **100**, 11047–11052 (2003).
32. S. Yang, S. Yang, T. Moreira, G. Hoffman, G. C. Carlson, K. J. Bender, B. E. Alger, C.-M. Tang, Interlamellar CA1 network in the hippocampus. *Proc. Natl. Acad. Sci. U.S.A.* **111**, 12919–12924 (2014).
33. A. Tzilivaki, G. Kastellakis, P. Poirazi, Challenging the point neuron dogma: FS basket cells as 2-stage nonlinear integrators. *Nat. Commun.* **10**, 3664 (2019).
34. S. A. Barnes, A. Pinto-Duarte, A. Kappe, A. Zembrzycki, A. Metzler, E. A. Mukamel, J. Lucero, X. Wang, T. J. Sejnowski, A. Markou, M. M. Behrens, Disruption of mGluR5 in parvalbumin-positive interneurons induces core features of neurodevelopmental disorders. *Mol. Psychiatry* **20**, 1161–1172 (2015).
35. K. P. Lamsa, J. H. Heeroma, P. Somogyi, D. A. Rusakov, D. M. Kullmann, Anti-Hebbian long-term potentiation in the hippocampal feedback inhibitory circuit. *Science* **315**, 1262–1266 (2007).
36. T. Hainmuller, K. Krieglstein, A. Kulik, M. Bartos, Joint CP-AMPA and group I mGlu receptor activation is required for synaptic plasticity in dentate gyrus fast-spiking interneurons. *Proc. Natl. Acad. Sci. U.S.A.* **111**, 13211–13216 (2014).
37. R. De Filippo, B. R. Rost, A. Stumpf, C. Cooper, J. J. Tukker, C. Harms, P. Beed, D. Schmitz, Somatostatin interneurons activated by 5-HT2A receptor suppress slow oscillations in medial entorhinal cortex. *eLife* **10**, e66960 (2021).
38. Y. Nagai, N. Miyakawa, H. Takuwa, Y. Hori, K. Oyama, B. Ji, M. Takahashi, X.-P. Huang, S. T. Slocum, J. F. DiBerto, Y. Xiong, T. Urushihata, T. Hirabayashi, A. Fujimoto, K. Mimura, J. G. English, J. Liu, K. Inoue, K. Kumata, C. Seki, M. Ono, M. Shimojo, M.-R. Zhang, Y. Tomita, J. Nakahara, T. Suhara, M. Takada, M. Higuchi, J. Jin, B. L. Roth, T. Minamimoto, Deschloroclozapine, a potent and selective chemogenetic actuator enables rapid neuronal and behavioral modulations in mice and monkeys. *Nat. Neurosci.* **23**, 1157–1167 (2020).
39. D. Atasoy, S. M. Sternson, Chemogenetic tools for causal cellular and neuronal biology. *Physiol. Rev.* **98**, 391–418 (2018).
40. L. Topolnik, S. Tamboli, The role of inhibitory circuits in hippocampal memory processing. *Nat. Rev. Neurosci.* **23**, 476–492 (2022).
41. A. R. McFarlan, C. Y. C. Chou, A. Watanabe, N. Cherepacha, M. Haddad, H. Owens, P. J. Sjöström, The plasticitome of cortical interneurons. *Nat. Rev. Neurosci.* **24**, 80–97 (2022).
42. H. Alle, P. Jonas, J. R. P. Geiger, PTP and LTP at a hippocampal mossy fiber-interneuron synapse. *Proc. Natl. Acad. Sci. U.S.A.* **98**, 14708–14713 (2001).
43. R. D. Hodge, T. E. Bakken, J. A. Miller, K. A. Smith, E. R. Barkan, L. T. Graybuck, J. L. Close, B. Long, N. Johansen, O. Penn, Z. Yao, J. Eggermont, T. Höllt, B. P. Levi, S. I. Shehata, B. Aevermann, A. Beller, D. Bertagnolli, K. Brouner, T. Casper, C. Cobbs, R. Dalley, N. Dee, S.-L. Ding, R. G. Ellenbogen, O. Fong, E. Garren, J. Goldy, R. P. Gwinn, D. Hirschstein, C. D. Keene, M. Keshk, A. L. Ko, K. Lathia, A. Mahfouz, Z. Maltzer, M. McGraw, T. N. Nguyen, J. Nyhus, J. G. Ojemann, A. Oldre, S. Parry, S. Reynolds, C. Rimorin, N. V. Shapovalova, S. Somasundaram, A. Szafer, E. R. Thomsen, M. Tieu, G. Quon, R. H. Scheuermann, R. Yuste, S. M. Sunkin, B. Lelieveldt, D. Feng, L. Ng, A. Bernard, M. Hawrylycz, J. W. Phillips, B. Tasic, H. Zeng, A. R. Jones, C. Koch, E. S. Lein, Conserved cell types with divergent features in human versus mouse cortex. *Nature* **573**, 61–68 (2019).
44. S. Bugeon, J. Duffield, M. Dipoppa, A. Ritoux, I. Prankerd, D. Nicoloutsopoulos, D. Orme, M. Shinn, H. Peng, H. Forrest, A. Viduolyte, C. B. Reddy, Y. Isogai, M. Carandini, K. D. Harris, A transcriptomic axis predicts state modulation of cortical interneurons. *Nature* **607**, 330–338 (2022).
45. T. Klausberger, P. Somogyi, Neuronal diversity and temporal dynamics: The unity of Hippocampal circuit operations. *Science* **321**, 53–57 (2008).
46. T. Gloveli, T. Dugladze, S. Saha, H. Monyer, U. Heinemann, R. D. Traub, M. A. Whittington, E. H. Buhl, Differential involvement of oriens/pyramidale interneurones in hippocampal network oscillationsin vitro. *J. Physiol.* **562**, 131–147 (2005).
47. P. Antonoudiou, Y. L. Tan, G. Kontou, A. L. Upton, E. O. Mann, Parvalbumin and somatostatin interneurons contribute to the generation of Hippocampal gamma oscillations. *J. Neurosci.* **40**, 7668–7687 (2020).
48. J. Veit, R. Hakim, M. P. Jadi, T. J. Sejnowski, H. Adesnik, Cortical gamma band synchronization through somatostatin interneurons. *Nat. Neurosci.* **20**, 951–959 (2017).
49. L. Liu, H. Xu, J. Wang, J. Li, Y. Tian, J. Zheng, M. He, T.-L. Xu, Z.-Y. Wu, X.-M. Li, S.-M. Duan, H. Xu, Cell type–differential modulation of prefrontal cortical GABAergic interneurons on low gamma rhythm and social interaction. *Sci. Adv.* **6**, eaay4073 (2020).
50. J. Veit, G. Handy, D. P. Mossing, B. Doiron, H. Adesnik, Cortical VIP neurons locally control the gain but globally control the coherence of gamma band rhythms. *Neuron* **111**, 405–417.e5 (2023).
51. L. Que, D. Lukacsovich, W. Luo, C. Földy, Transcriptional and morphological profiling of parvalbumin interneuron subpopulations in the mouse hippocampus. *Nat. Commun.* **12**, 108 (2021).
52. J. J. Tukker, P. Fuentealba, K. Hartwich, P. Somogyi, T. Klausberger, Cell type-specific tuning of hippocampal interneuron firing during gamma oscillations *in vivo*. *J. Neurosci.* **27**, 8184–8189 (2007).
53. T. Gloveli, T. Dugladze, H. G. Rotstein, R. D. Traub, H. Monyer, U. Heinemann, M. A. Whittington, N. J. Kopell, Orthogonal arrangement of rhythm-generating microcircuits in the hippocampus. *Proc. Natl. Acad. Sci. U.S.A.* **102**, 13295–13300 (2005).
54. M. Sammari, Y. Inglebert, N. Ankri, M. Russier, S. Incontro, D. Debanne, Theta patterns of stimulation induce synaptic and intrinsic potentiation in O-LM interneurons. *Proc. Natl. Acad. Sci. U.S.A.* **119**, e2205264119 (2022).
55. A. B. L. Tort, H. G. Rotstein, T. Dugladze, T. Gloveli, N. J. Kopell, On the formation of gamma-coherent cell assemblies by oriens lacunosum-moleculare interneurons in the hippocampus. *Proc. Natl. Acad. Sci. U.S.A.* **104**, 13490–13495 (2007).
56. C. Zheng, K. W. Bieri, S. G. Trettel, L. L. Colgin, The relationship between gamma frequency and running speed differs for slow and fast gamma rhythms in freely behaving rats. *Hippocampus* **25**, 924–938 (2015).
57. W. Zhong, M. Ciatipis, T. Wolfenstetter, J. Jessberger, C. Müller, S. Ponsel, Y. Yanovsky, J. Brankačk, A. B. L. Tort, A. Draguhn, Selective entrainment of gamma subbands by different slow network oscillations. *Proc. Natl. Acad. Sci. U.S.A.* **114**, 4519–4524 (2017).
58. B. Lasztóczi, T. Klausberger, Hippocampal place cells couple to three different gamma oscillations during place field traversal. *Neuron* **91**, 34–40 (2016).
59. M. Strüber, J.-F. Sauer, P. Jonas, M. Bartos, Distance-dependent inhibition facilitates focality of gamma oscillations in the dentate gyrus. *Nat. Commun.* **8**, 758 (2017).
60. C. B. Lu, J. G. R. Jefferys, E. C. Toescu, M. Vreugdenhil, In vitro hippocampal gamma oscillation power as an index of in vivo CA3 gamma oscillation strength and spatial reference memory. *Neurobiol. Learn. Mem.* **95**, 221–230 (2011).
61. B. R. Rost, J. Wietek, O. Yizhar, D. Schmitz, Optogenetics at the presynapse. *Nat. Neurosci.* **25**, 984–998 (2022).
62. J. R. P. Geiger, T. Melcher, D.-S. Koh, B. Sakmann, P. H. Seeburg, P. Jonas, H. Monyer, Relative abundance of subunit mRNAs determines gating and Ca^{2+} permeability of AMPA receptors in principal neurons and interneurons in rat CNS. *Neuron* **15**, 193–204 (1995).
63. J. R. P. Geiger, J. Lübke, A. Roth, M. Frotscher, P. Jonas, Submillisecond AMPA receptor-mediated signaling at a principal neuron–interneuron synapse. *Neuron* **18**, 1009–1023 (1997).
64. G. Etter, S. van der Veldt, F. Manseau, I. Zarrinkoub, E. Trillaud-Doppia, S. Williams, Optogenetic gamma stimulation rescues memory impairments in an Alzheimer's disease mouse model. *Nat. Commun.* **10**, 5322 (2019).
65. E. Campanac, C. Gasselin, A. Baude, S. Rama, N. Ankri, D. Debanne, Enhanced intrinsic excitability in basket cells maintains excitatory-inhibitory balance in hippocampal circuits. *Neuron* **77**, 712–722 (2013).
66. M. Udakis, V. Pedrosa, S. E. L. Chamberlain, C. Clopath, J. R. Mellor, Interneuron-specific plasticity at parvalbumin and somatostatin inhibitory synapses onto CA1 pyramidal neurons shapes hippocampal output. *Nat. Commun.* **11**, 4395 (2020).

67. E. D. Vickers, C. Clark, D. Osypenko, A. Fratzl, O. Kochubey, B. Bettler, R. Schneggenburger, Parvalbumin-interneuron output synapses show spike-timing-dependent plasticity that contributes to auditory map remodeling. *Neuron* **99**, 720–735.e6 (2018).
68. E.-L. Yap, N. L. Pettit, C. P. Davis, M. A. Nagy, D. A. Harmin, E. Golden, O. Dagliyan, C. Lin, S. Rudolph, N. Sharma, E. C. Griffith, C. D. Harvey, M. E. Greenberg, Bidirectional perisomatic inhibitory plasticity of a Fos neuronal network. *Nature* **590**, 115–121 (2021).
69. Z. Brzosko, S. B. Mierau, O. Paulsen, Neuromodulation of spike-timing-dependent plasticity: Past, present, and future. *Neuron* **103**, 563–581 (2019).
70. A. Reiner, J. Levitz, Glutamatergic signaling in the central nervous system: Ionotropic and metabotropic receptors in concert. *Neuron* **98**, 1080–1098 (2018).
71. A. Wagatsuma, T. Okuyama, C. Sun, L. M. Smith, K. Abe, S. Tonegawa, Locus coeruleus input to hippocampal CA3 drives single-trial learning of a novel context. *Proc. Natl. Acad. Sci. U.S.A.* **115**, E310–E316 (2018).
72. A. Chowdhury, A. Luchetti, G. Fernandes, D. A. Filho, G. Kastellakis, A. Tzilivaki, E. M. Ramirez, M. Y. Tran, P. Poirazi, A. J. Silva, A locus coeruleus-dorsal CA1 dopaminergic circuit modulates memory linking. *Neuron* **110**, 3374–3388.E8 (2022).
73. Y. Chen, A. J. Granger, T. Tran, J. L. Saulnier, A. Kirkwood, B. L. Sabatini, Endogenous Gαq-coupled neuromodulator receptors activate protein kinase a. *Neuron* **96**, 1070–1083.e5 (2017).
74. H.-Y. Wang, M. L. MacDonald, K. E. Borgmann-Winter, A. Banerjee, P. Sleiman, A. Tom, A. Khan, K.-C. Lee, P. Roussos, S. J. Siegel, S. E. Hemby, W. B. Bilker, R. E. Gur, C.-G. Hahn, mGluR5 hypofunction is integral to glutamatergic dysregulation in schizophrenia. *Mol. Psychiatry* **25**, 750–760 (2020).
75. J. M. Rook, Z. Xiang, X. Lv, A. Ghoshal, J. W. Dickerson, T. M. Bridges, K. A. Johnson, D. J. Foster, K. J. Gregory, P. N. Vinson, A. D. Thompson, N. Byun, R. L. Collier, M. Bubser, M. T. Nedelcovych, R. W. Gould, S. R. Stauffer, J. S. Daniels, C. M. Niswender, H. Lavreysen, C. Mackie, S. Conde-Ceide, J. Alcazar, J. M. Bartolomé-Nebreda, G. J. Macdonald, J. C. Talpos, T. Steckler, C. K. Jones, C. W. Lindsley, P. J. Conn, Biased mGlu 5-positive allosteric modulators provide in vivo efficacy without potentiating mGlu 5 modulation of NMDAR currents. *Neuron* **86**, 1029–1040 (2015).
76. Y. Huang, H. Jiang, Q. Zheng, A. H. K. Fok, X. Li, C. G. Lau, C. S. W. Lai, Environmental enrichment or selective activation of parvalbumin-expressing interneurons ameliorates synaptic and behavioral deficits in animal models with schizophrenia-like behaviors during adolescence. *Mol. Psychiatry* **26**, 2533–2552 (2021).
77. A. Mukherjee, F. Carvalho, S. Eliez, P. Caroni, Long-lasting rescue of network and cognitive dysfunction in a genetic Schizophrenia model. *Cell* **178**, 1387–1402.e14 (2019).
78. T. Marissal, R. F. Salazar, C. Bertollini, S. Mutel, M. De Roo, I. Rodriguez, D. Müller, A. Carleton, Restoring wild-type-like CA1 network dynamics and behavior during adulthood in a mouse model of schizophrenia. *Nat. Neurosci.* **21**, 1412–1420 (2018).
79. C. Adaikkan, S. J. Middleton, A. Marco, P.-C. Pao, H. Mathys, D. N.-W. Kim, F. Gao, J. Z. Young, H.-J. Suk, E. S. Boyden, T. J. McHugh, L.-H. Tsai, Gamma entrainment binds higher-order brain regions and offers neuroprotection. *Neuron* **102**, 929–943.e8 (2019).
80. M. Shen, Y. Guo, Q. Dong, Y. Gao, M. E. Stockton, M. Li, S. Kannan, T. Korabelnikov, K. A. Schoeller, C. L. Sirois, C. Zhou, J. Le, D. Wang, Q. Chang, Q.-Q. Sun, X. Zhao, FXR1 regulation of parvalbumin interneurons in the prefrontal cortex is critical for schizophrenia-like behaviors. *Mol. Psychiatry* **26**, 6845–6867 (2021).
81. M. Soula, A. Martín-Ávila, Y. Zhang, A. Dhingra, N. Nitzan, M. J. Sadowski, W.-B. Gan, G. Buzsáki, Forty-hertz light stimulation does not entrain native gamma oscillations in Alzheimer's disease model mice. *Nat. Neurosci.* **26**, 570–578 (2023).
82. M. L. Hines, N. T. Carnevale, The NEURON simulation environment, *Neural Comput.* 9, 1179–1209 (1997).
83. Q. Sun, A. Sotayo, A. S. Cazzulino, A. M. Snyder, C. A. Denny, S. A. Siegelbaum, Proximodistal heterogeneity of hippocampal CA3 pyramidal neuron intrinsic properties, connectivity, and reactivation during memory recall. *Neuron* **95**, 656–672.e3 (2017).
84. T. G. Banke, C. J. McBain, GABAergic input onto CA3 hippocampal interneurons remains shunting throughout development. *J. Neurosci.* **26**, 11720–11725 (2006).
85. F. Fukushima, K. Nakao, T. Shinoe, M. Fukaya, S. Muramatsu, K. Sakimura, H. Kataoka, H. Mori, M. Watanabe, T. Manabe, M. Mishina, Ablation of NMDA receptors enhances the excitability of hippocampal CA3 neurons. *PLOS ONE* **4**, e3993 (2009).
86. Z. Kohus, S. Káli, L. Rovira-Esteban, D. Schlingloff, O. Papp, T. F. Freund, N. Hájos, A. I. Gulyás, Properties and dynamics of inhibitory synaptic communication within the CA3 microcircuits of pyramidal cells and interneurons expressing parvalbumin or cholecystokinin. *J. Physiol.* **594**, 3745–3774 (2016).
87. N. Vladimirov, R. D. Traub, Synaptic gating at axonal branches, and sharp-wave ripples with replay: A simulation study. *Eur. J. Neurosci.* **38**, 3435–3447 (2013).
88. V. K. Y. Ng, R. A. Cribbie, Using the gamma generalized linear model for modeling continuous, skewed and heteroscedastic outcomes in psychology. *Curr. Psychol.* **36**, 225–235 (2017).

Acknowledgments: We thank C. Birchmeier, J. Poulet, and B. Rost for the provision of PV-Cre, Ai9, and Flex-hM4Di animals, respectively. We thank P. Wulff for the generation and provision of loxp-mG5 mice. We thank L. Soso Zradkovic for assistance with imaging and A. Wilke for technical assistance with animal husbandry. We thank R. Bernard, D. Parthier, B. Rost, N. Maier, and J. Sauer for insightful comments on an earlier version of the manuscript. **Funding:** This work was supported by the Deutsche Forschungsgemeinschaft (DFG; FOR 2143 and TRR 295 to M.D.H. and J.R.P.G; TRR 1315 to A.T. and D.S.; and FOR 3004 and TRR 958 to D.S.), the Federal Ministry of Education and Research (grant 01GQ1420B to D.S.), and the European Research Council (grant 810580 to D.S.). A.T. is supported by the DFG with the SFB1315-2 TP A01 Brenda Milner Award and the Einstein Center for Neurosciences Berlin PhD Fellowship. **Author contributions:** Conceptualization: M.D.H. and J.R.P.G. Electrophysiology: M.D.H. Computational modeling: A.T. Visualization: M.D.H. Supervision: H.A., D.S., and J.R.P.G. Writing—original draft: M.D.H. Writing—review and editing: M.D.H., A.T., D.S., H.A., and J.R.P.G. **Competing interests:** The authors declare that they have no competing interests. **Data and materials availability:** All data needed to evaluate the conclusions in the paper are present in the paper and/or the Supplementary Materials. Analysis datasets and statistical reporting (DOI: 10.5281/zenodo.8383858), MATLAB code for time-series analysis of LFP and pMEA data (DOI: 10.5281/zenodo.8432332), and the computational model's source code and the datasets used to generate Fig. 4 (DOI: 10.5281/zenodo.8432491) are publicly available on the Zenodo platform.

Submitted 20 July 2023
Accepted 2 January 2024
Published 31 January 2024
10.1126/sciadv.adj7427

Science Advances
AAAS

Supplementary Materials for

Gamma-oscillation plasticity is mediated via parvalbumin interneurons

Michael D. Hadler, et al.
Corresponding authors. Email: michael.hadler@charite.de & joerg.geiger@charite.de

This PDF file includes:

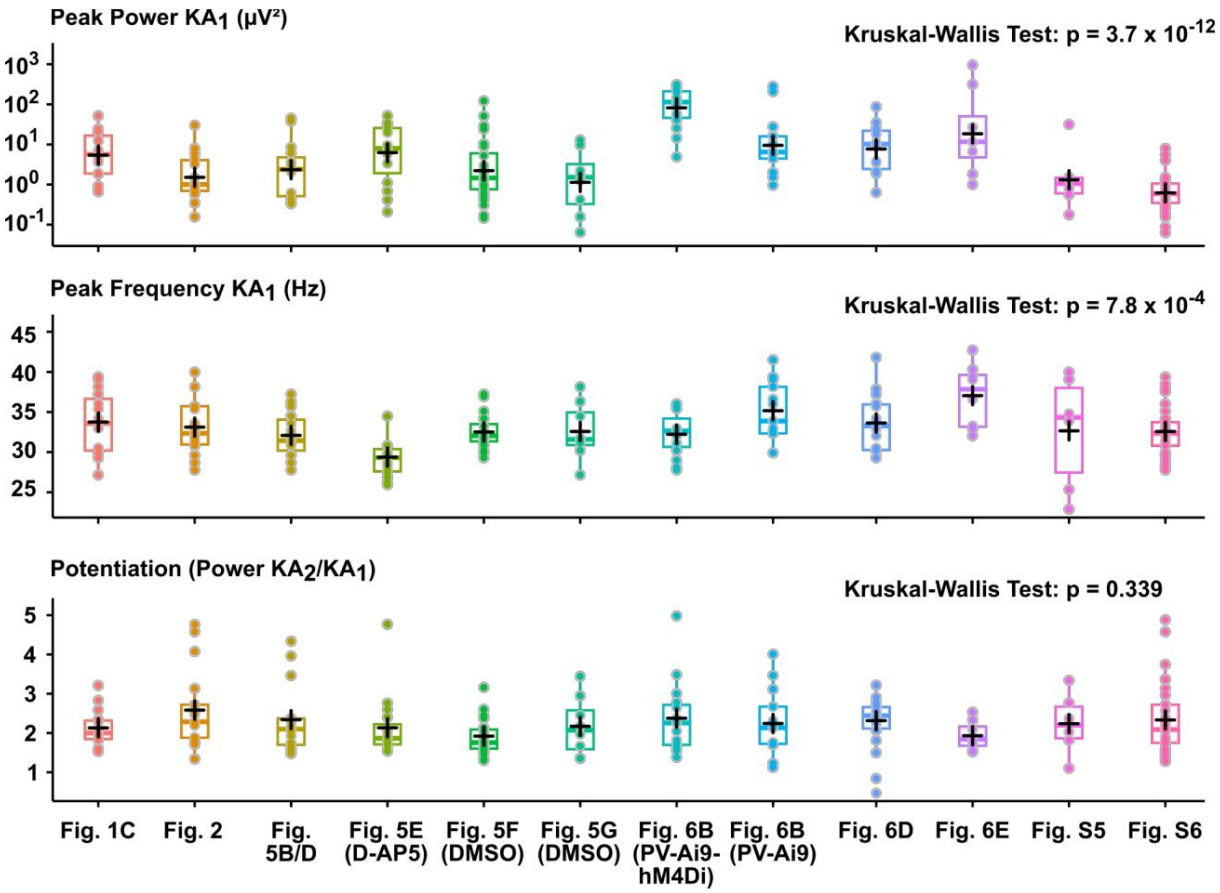

Fig. S1. Multi-trial stability of gamma-potentiation in LFP recordings. Boxplots of all control experiments in the twelve interventions reported. Crosses denote the mean. Above: Log-scale boxplot of peak gamma-power in the first induction period (KA_1). Centre: Peak frequency of oscillations in the first induction period. Below: Magnitude of gamma potentiation. Note the high variability of KA_1 peak power and frequency amongst trials, which is not mirrored in the subsequent potentiation of peak power.

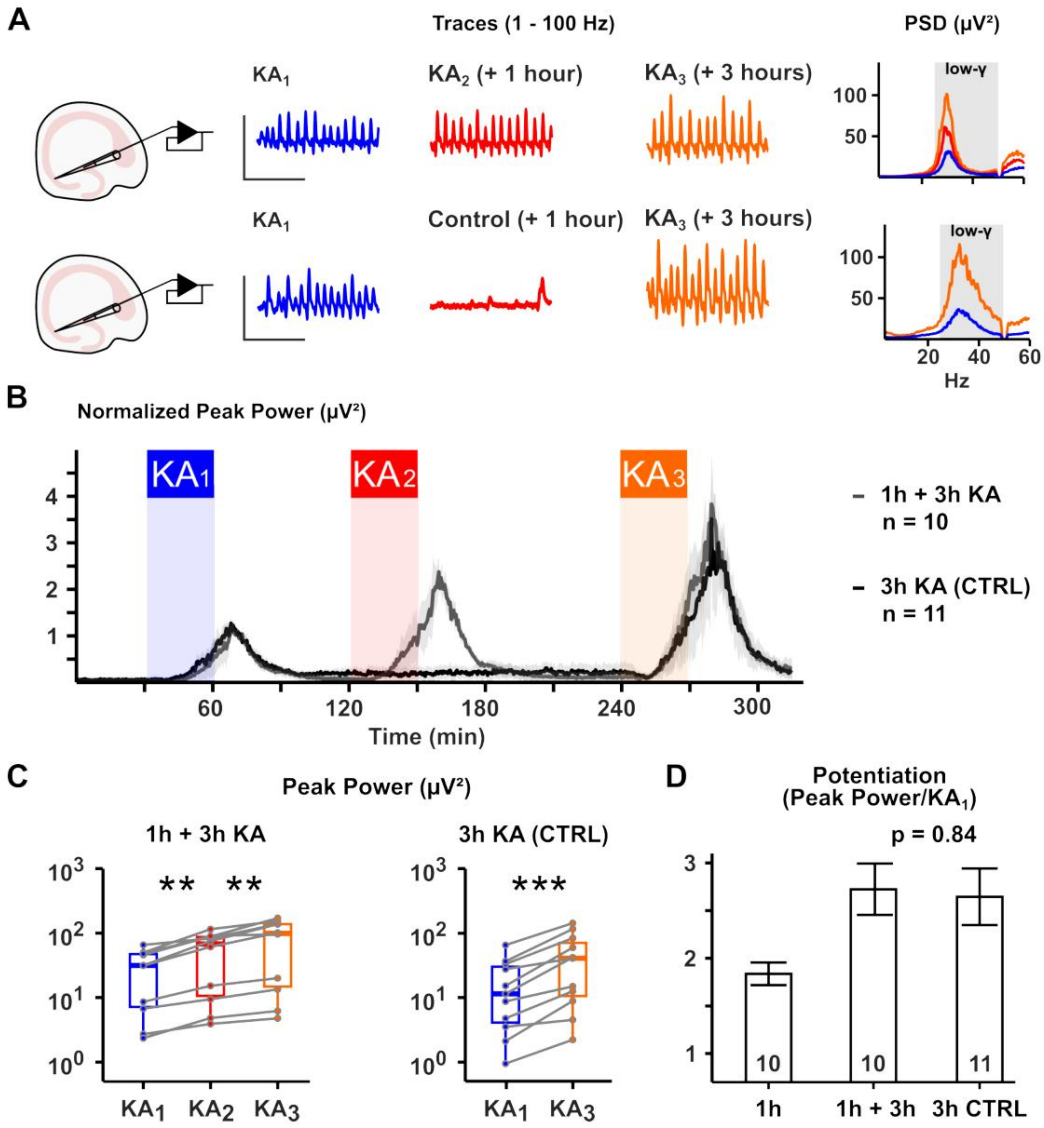

Fig. S2 Long-term saturation of gamma-potentiation. (A) Schematic of the experimental paradigm. All slices are stimulated identically with KA in the first induction period (KA_1), yielding persistent gamma-activity. Slices are subsequently divided into a group receiving two further, identical treatments with KA after 1 hour (KA_2) and 3 hours (KA_3) and a control group receiving just the second additional treatment after 3 hours (KA_3). Spectrograms are obtained and analyzed from all three induction periods. Scales indicate 500 µV/250 ms. **(B)** Time-Power plot of peak power (15 – 49 Hz) for both groups normalized to the first application period. Ribbons denote the 95% confidence interval. **(C)** Paired boxplots of peak gamma-power in both application periods with either 1- and/or 3-hour delay. ** and *** denote $p < 0.01$ and < 0.001, respectively (Wilcoxon signed-rank test). **(D)** Barplot of average potentiation for each application cycle in both groups. P-value in barplot obtained from a log-linked gamma-GLM with post-hoc comparison of estimated marginal means.

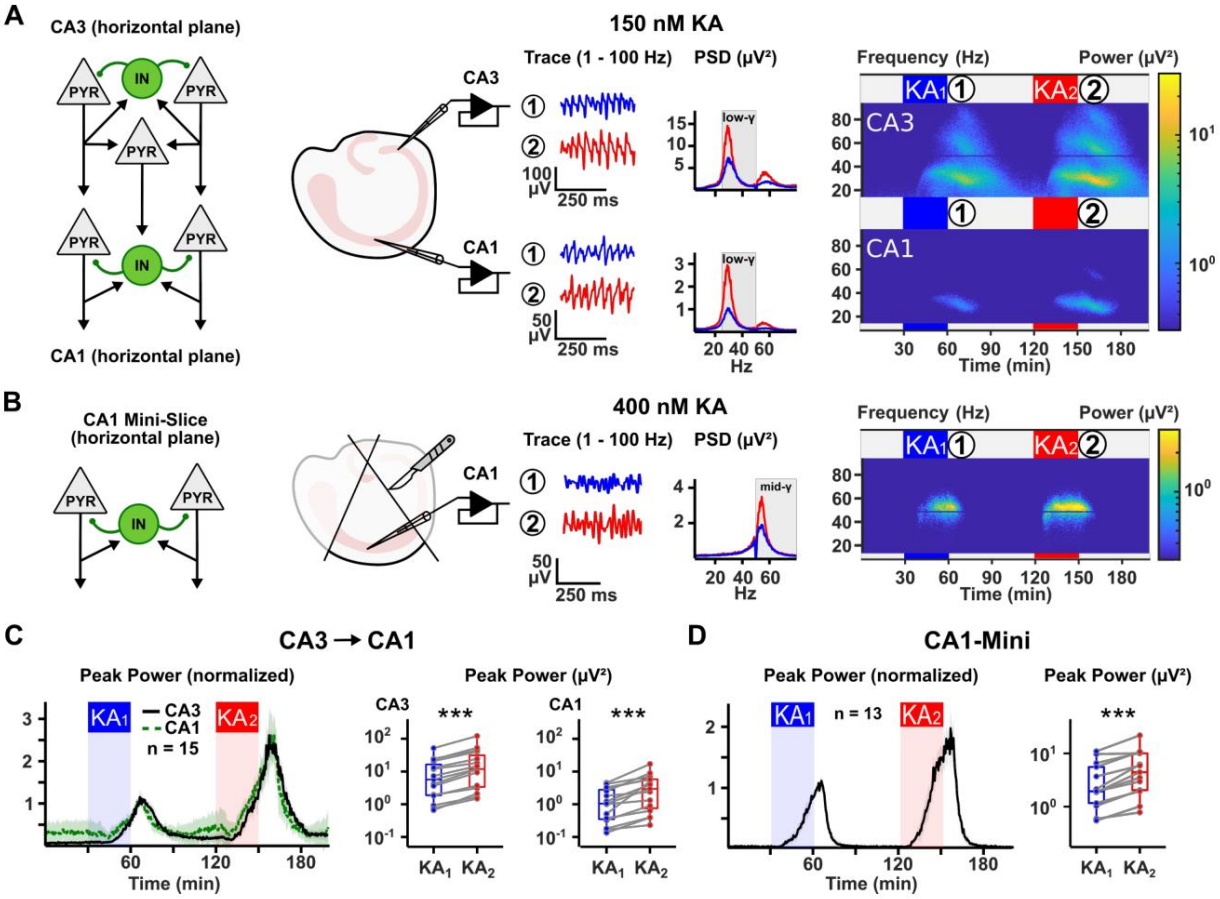

Fig. S3. Gamma-potentiation in paired CA3-CA1 and CA1-Mini LFP recordings. (A) *Left*: Schematic of CA3 and CA1 connectivity in the horizontal slice plane. CA3 pyramidal cells (PYR) are interconnected amongst themselves and local interneurons (INs) and target CA1 PYRs and INs via the Schaffer collateral pathway. CA1 PYRs do not connect amongst each other but are interconnected with local CA1 INs. *Centre*: Schematic of a hippocampal slice with LFP electrodes in CA3 and CA1. Exemplary traces as in Fig. 1A with simultaneous recordings of CA3 and CA1. *Right*: Pseudocolor plots of the entire experiment. **(B)** *Left*: Schematic of the CA1 Mini-slice microcircuit. *Centre*: Schematic drawing of the hippocampus with surgical cuts separating CA1 from the subiculum and CA3. A recording pipette was placed in stratum pyramidale. *Right*: Same as in (A) but for an exemplary recording in a CA1-Mini slice. Gamma-activity was induced with 400 nM KA instead of 150 nM. Grey inset "mid-gamma" in the PSDs denotes the window spanning 50 – 80 Hz. **(C)** *Left:* Time-Power plot for all paired CA3-CA1 recordings normalized to the first induction period. *Right:* Paired boxplots of peak gamma-power in both application periods in CA3 and CA1. **(D)** Same as (C), but for the experiments in CA1-Mini slices. *** denotes $p < 0.001$ (Wilcoxon Signed-Rank test).

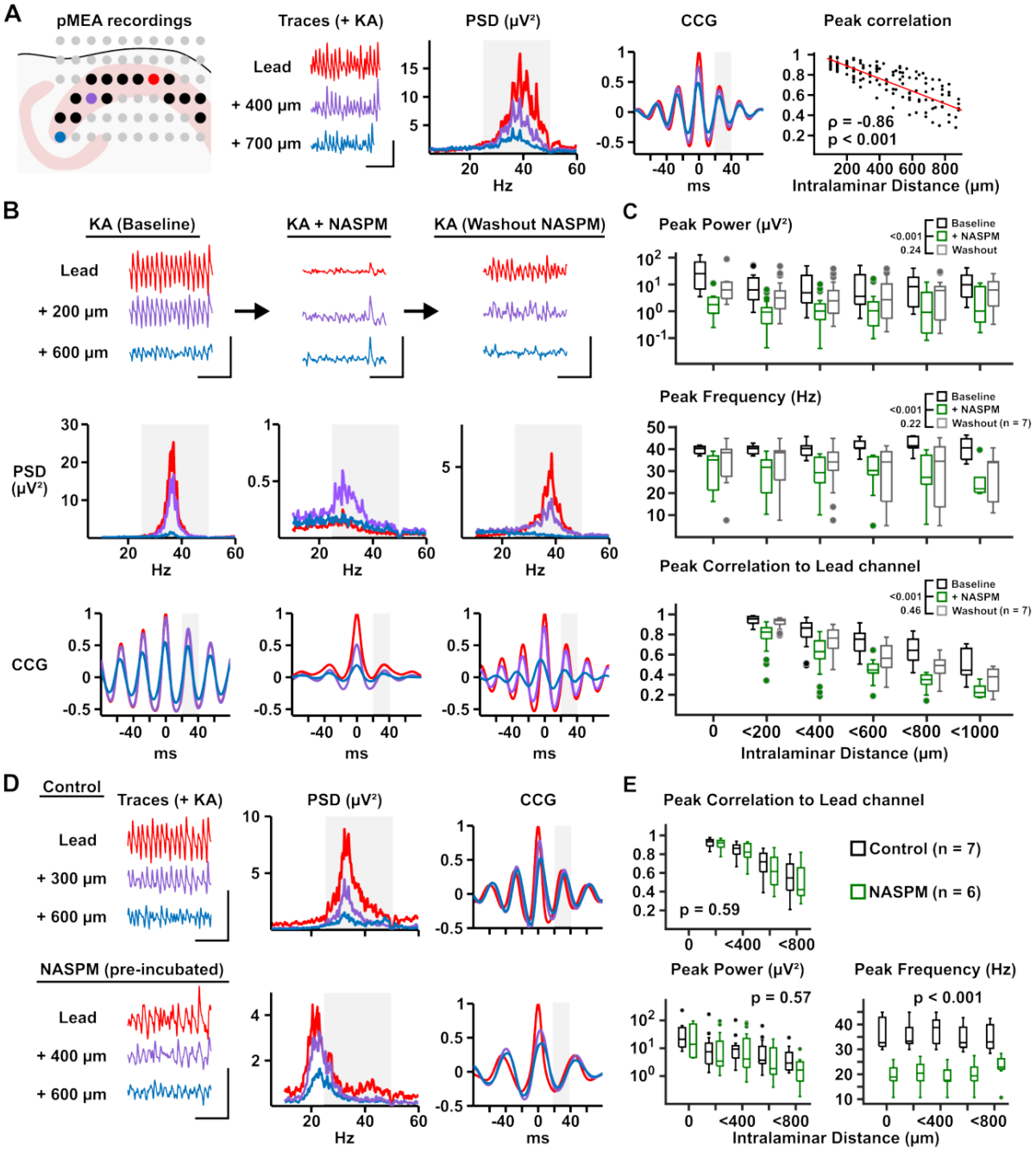

Fig. S4. CP-AMPARs generate and maintain the gamma-rhythm in pMEA recordings. (A) Gamma-oscillations are generated across CA3 with decreasing inter-site cross-correlation. *Left, Centre*: Exemplary recording configuration in the 6 x 10 MEA grid with selected electrodes in black. Red, purple and blue electrodes resemble the recordings displayed in the traces, PSDs and cross-correlograms (CCG) after application of KA (200 nM). The red correlogram represents the auto-correlogram of the "lead electrode" (highest power in PSD). *Right*: Scatter plot of pooled peak cross-correlation of electrodes to the lead electrode. A linear fit is superimposed. Rho and p refer to the results of Pearson's correlation test. **(B)** Gamma-oscillations are maintained by CP-

AMPARs. An exemplary experiment with traces at three sites (above) and the corresponding PSDs (centre) and correlograms (below). After an initial induction of gamma-oscillations with 200 nM KA (left), NASPM is added to the bath (centre) and oscillations dissipate. Following washout of NASPM (right), oscillations re-appear in 2/3 sites displayed. **(C)** Boxplots to the experiments in (B). Values are displayed for peak power, frequency and cross-correlation as a function of intralaminar distance. P-values refer to group comparisons towards baseline (generalized linear model). Peak power values were log-transformed before statistical testing. **(D)** CP-AMPAR lacking rhythms are similar to gamma-oscillations in power and inter-site cross-correlation, but markedly reduced in peak frequency. Exemplary experiments as in (B) for a control slice (above) and a slice pre-incubated with NASPM (100 μM) before application of KA (200 nM). In the presence of NASPM, the peak of the PSD and correlograms is clearly below the low gamma-frequency range (25 – 50 Hz and 20 – 40 ms for PSD and correlograms, respectively). **(E)** Boxplots of recorded peak values for power, frequency and cross-correlation to the lead channel as a function of intralaminar distance toward the lead channel. A reduction in peak frequency is observed across all recording sites after pre-incubation with NASPM. P-Values obtained from a generalized linear model.

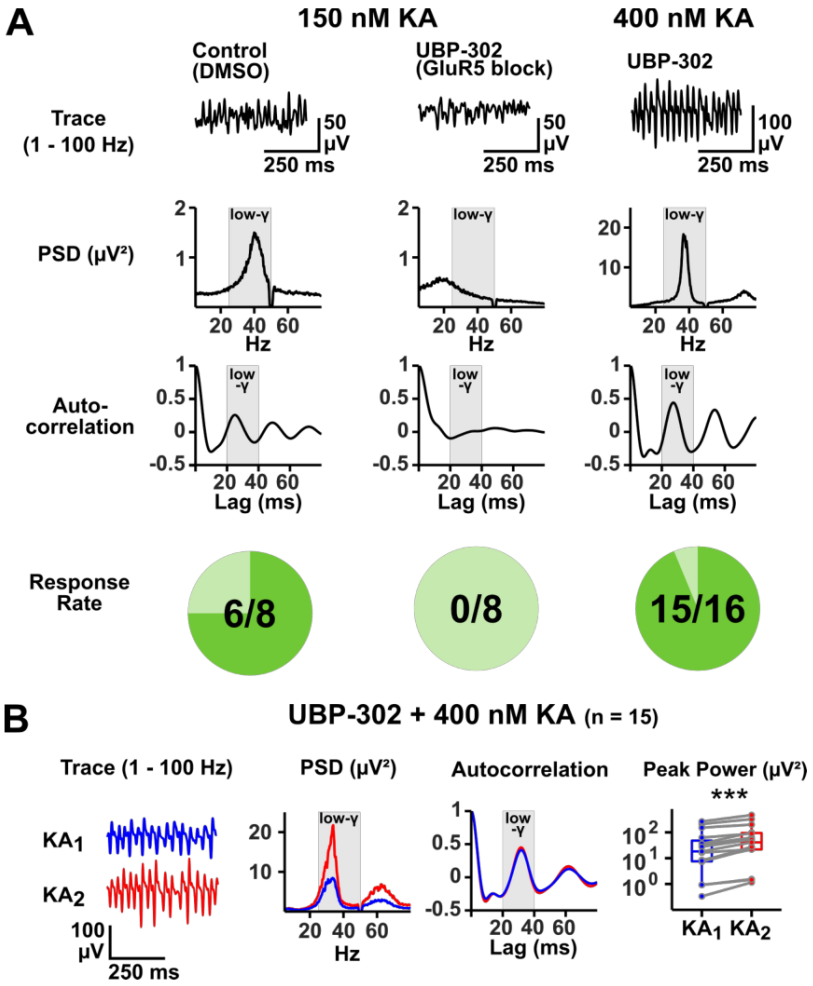

Fig. S5. Blockade of GluK1 with UBP-302 attenuates the induction of gamma-oscillations but does not alter gamma-potentiation. (A) Exemplary traces, power spectra and ACGs for DMSO Control experiments and UBP-302 pre-incubation with two concentrations of KA (150 and 400 nM). At 150 nM KA, pre-incubation with UBP-302 prevents the generation of a discernible rhythm in the ACG. Below: Pie charts of the response rates of the individual paradigms. **(B)** Gamma-potentiation in the presence of UBP-302 at 400 nM KA. *Left*: Exemplary traces during the first and second induction period (KA_1 and KA_2). *Centre*: Corresponding PSD and ACG. Grey insets "low-gamma" in the PSDs and ACGs denotes the window spanning 25 – 50 Hz. *Right*: Paired boxplot of peak gamma-power during both induction periods. *** denotes $p < 0.001$ (Wilcoxon Signed-Rank test).

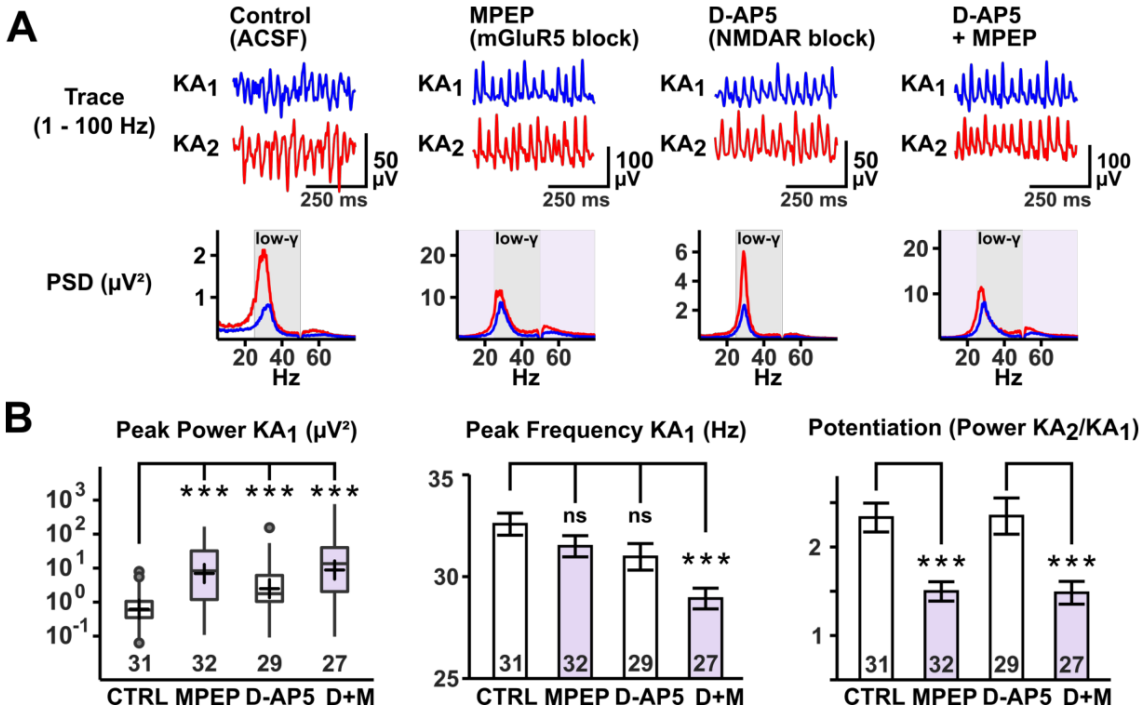

Fig. S6. mGluR5, not NMDARs, contributes to gamma-potentiation. Blockade of NMDARs and mGluR5 increases peak gamma-power and decreases peak gamma-frequency. (A) Exemplary traces and power spectra for Control, D-AP5, MPEP and D-AP5 + MPEP (D+M) conditions during both induction periods (KA_1, KA_2). **(B)** Summary statistics for all conditions. *Left*: Boxplot of peak gamma-power in KA_1 for all conditions. *** indicates $p < 0.001$, multiple Mann-Whitney U-tests. *Centre*: Barplot of peak gamma-frequency during KA_1. *Right*: Barplot of potentiation of peak power in all conditions. *** and ns in barplots denote $p < 0.001$ and $p > 0.05$ (generalized linear model). Purple insets denote the application of MPEP.

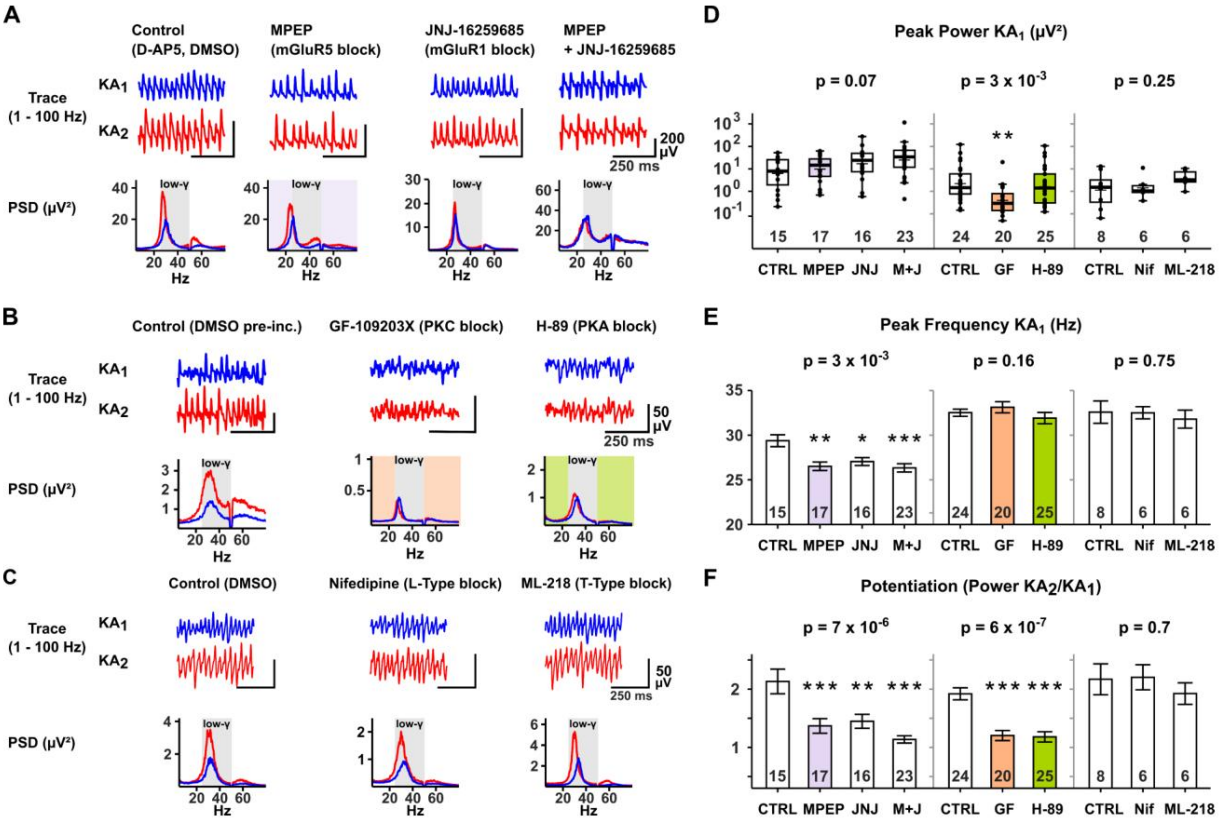

Fig. S7. Contribution of mediators of synaptic plasticity towards induction and plasticity of gamma oscillations. (A-C) Exemplary traces and PSDs for data presented in Fig. 5E-G. **(D)** Boxplots of peak gamma power in the first induction period (KA_1) in all three studies. Blockade of PKC with GF 109203X (3 µM) reduces peak gamma power. **(E)** Barplot of average peak frequencies in KA_1. Blockade of either mGluR5 with MPEP (10 µM) or JNJ-16259685 (0.3 µM) or both substances reduces the peak frequency. **(F)** Barplots of average potentiation as shown in Fig. 5E-G. P-values in plots indicate the result of the Kruskal-Wallis test in the respective study. *, ** and *** indicate $p < 0.05$, 0.01 and 0.001 (Mann-Whitney U-test in (D), generalized linear models in (E-F)).

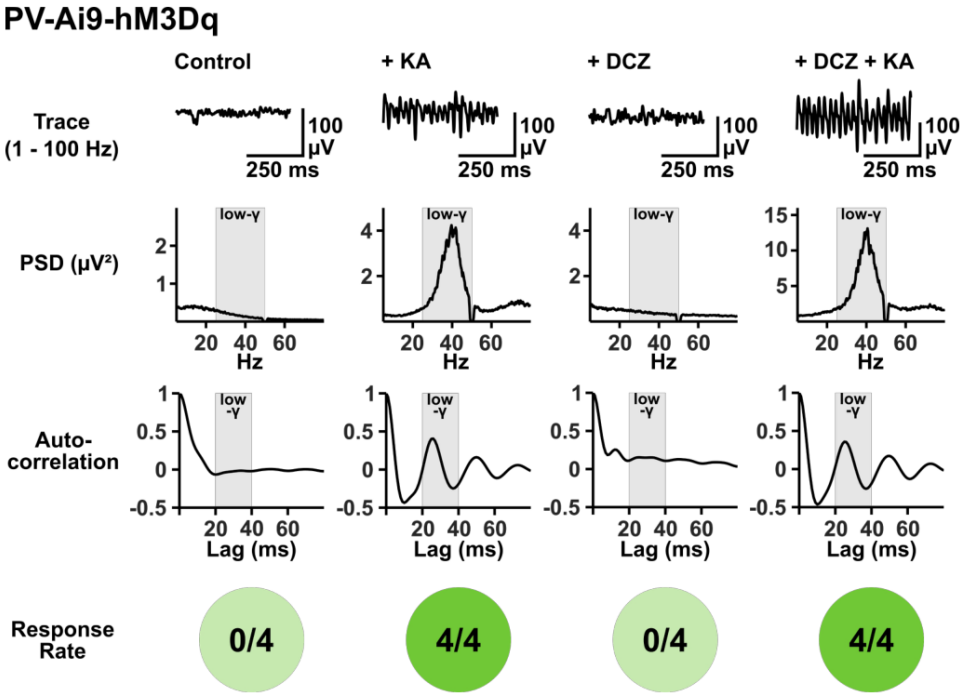

Fig. S8. Sole activation of hM3Dq in PVIs is insufficient to synchronize CA3 network activity. Traces, PSDs and ACGs of conditions testing whether gamma-activity can be induced with just 3 µM DCZ as compared to application of kainate (KA, 150 nM). Pie charts below indicate the numbers of slices in which oscillations were induced for each condition. KA or DCZ were applied or co-applied for 30 minutes.

Table S1. Passive parameters and active conductance values for all compartments of the pyramidal model cell.

Mechanism	***Soma***	***Proximal Apical Dendrite***	***Distal Apical Dendrites***	***Basal Dendrites***
Leak conductance [S/cm^2]	0,0002	0,0002	0,0002	0,0002
Na^+ conductance [S/cm^2]	0,0105	0,0084	0,0084	0,0084
Delayed rectifier K+ conductance [S/cm^2]	0,00086	0,00086	0,00086	0,00086
Proximal A-type K+ conductance [S/cm^2]	0,0075	0,015	-	0,0075
Distal A-type K+ conductance [S/cm^2]	-	-	0,04875	-
M-type K+ conductance [S/cm^2]	0.06	0.06	-	0.06
Ih conductance [S/cm^2]	0.00005	0.0001	-	0.00005
L-type Ca2+ conductance [S/cm^2]	0.0007	0.00003	-	0.00003
R-type Ca2+ conductance [S/cm^2]	0.0003	0.00003	-	-
T-type Ca2+ conductance [S/cm^2]	0.00005	0.0001	-	0.0001
Ca^{2+}-dependent sAHP K^+ conductance [S/cm^2]	0.0015	0.001	-	0.0005
Ca^{2+}-dependent mAHP K^+ conductance [S/cm^2]	0,9	0,03	-	0,08
Membrane capacitance Cm [µF/cm^2]	1	1	1	1
Membrane resistance Rm [Ohm cm^2]	6000	6000	6000	6000
Axial resistance Ra [Ohm cm]	150	150	150	150

Table S2. Electrophysiological characterization of the pyramidal model cell.

Parameter	***Value***
Rheobase (pA)	200
Input Resistance (MΩ)	142
Spike Threshold (mV)	-43,11
Spike Amplitude (mV)	73,11
Spike Overshoot (mV)	30
Resting Membrane Potential (mV)	-70
AP Frequency (Hz) during Rheobase current clamp	6

Table S3. CA3 microcircuit synaptic conductance values.

Synapse Type	*Pyramidal model*	*PV Basket Cell model*
INPUT AMPA	0,002	-
INPUT NMDA	0,005	-
CI-AMPA	0,0017 (baseline) 0,00255 (plasticity)	-
CP-AMPA	-	0,0015 (baseline) 0,00225 (plasticity)
NMDA	0,0051	0,0016
GABA	0,004	0,005
Autapse GABA	-	0,007

Curriculum Vitae

My curriculum vitae does not appear in the electronic version of my paper for reasons of data protection.

Publication list

Publications

Hadler, M.D., Alle, H., Geiger, J.R.P., 2024a. Parvalbumin interneuron cell-to-network plasticity: mechanisms and therapeutic avenues. Trends in Pharmacological Sciences 45, 586–601. https://doi.org/10.1016/j.tips.2024.04.003

Hadler, M. D., Tzilivaki, A., Schmitz, D., Alle, H. & Geiger, J. R. P., 2024b. Gamma oscillation plasticity is mediated via parvalbumin interneurons, *Science Advances*, eadj7427(2024). https://doi.org/10.1126/sciadv.adj7427

Gebhardt, C., von Bohlen und Halbach, O., **Hadler, M. D.**, Harteneck, C., & Albrecht, D., 2016. A novel form of capsaicin-modified amygdala LTD mediated by TRPM1. *Neurobiology of Learning and Memory*, *136*, 1–12. https://doi.org/10.1016/j.nlm.2016.09.005

Impact factor

Journal name	Year	Impact factor
Science Advances	2024	14.136
Trends in Pharmacological Sciences	2024	13.8
Neurobiology of Learning and Memory	2016	3.543

Preprints

Hadler, M. D., Tzilivaki, A., Schmitz, D., Alle, H., & Geiger, J. R. P., 2023. Gamma-Oscillation Plasticity Is Mediated by Parvalbumin Interneurons [Preprint]. *bioRxiv.* https://doi.org/10.1101/2023.06.21.545901

Acknowledgments

This thesis was a long process during which I was fortunate enough to receive an incredible amount of support and to meet many helpful, dedicated people, who all deserve my utmost gratitude.

First and foremost, I would like to thank Prof. Jörg Geiger for the opportunity and trust to pursue this project under his supervision at the Institute of Neurophysiology. His encyclopedic knowledge of neuroscience has been and continues to be a constant source of inspiration for me, and it was his own experimental experience in the field of interneuron plasticity that laid the foundation for this work. Despite his willingness to participate in project design, I am also grateful for the many freedoms granted me, actively and passively, allowing me to grow as a scientist.

I want to express my sincere gratitude to Prof. Geiger for the warm support around the birth of my daughter, which gave me confidence and reassurance in a time of rapid, sometimes frightening change.

I would also like to thank my co-supervisors, Drs. Zoltan Gerevich and Henrik Alle, for their support and cooperation. Dr. Gerevich's previous work as an expert in ex vivo gamma-oscillations was an indispensable prerequisite for the completion of this work, and I would like to thank him for the years of patiently sharing a rig with me – flaws and all. Dr. Alle has been and continues to be a constant role model for me due to his unparalleled competence as a scientist and educator, and his enthusiasm for science communication has profoundly influenced and shaped me.

I would like to thank my co-author, Alexandra Tzilivaki, for her enthusiasm and commitment, which resulted in a significant contribution to our project in a short period of time. I also want to thank Dietmar Schmitz for his support, experience, and insights into hippocampal network phenomena, as well as for tricks and tips for the publication process, which saved me a lot of mental effort.

I want to thank numerous colleagues at the Institute of Neurophysiology for their support over the years. Whether it was a small (or big) favor, an interesting conversation, or words of encouragement, everything contributed to the completion of this work: Doris Albrecht, Victoria Antemann, Tom Bickel, Matti Blunck, Anatoli Ender, Sonja Frosinski, Christine

Gebhardt, Luisa Hasam-Hendersson, Marcel Heim, Sridhar Jagannathan, Zin Klafft, Alexander Klemz, Constantin Klisch, Richard Kovacs, Mirja Grote Lambers, Agustin Liotta, Christian Madry, Franz Mittermaier, Julia Neugebauer, David Owald, Yangfan Peng, Henrike Planert, Heidi Pretorius, Davide Raccuglia, Eric Reynolds, Ali Rifat, Roland Schneider, Katrin Schulze, Philip Steiskal, Leon Steiner, Raquel Súarez-Grimalt, Michael Surala, Ecem Tütüncü, Florian Wildner, Vera Wuntke, Zhen-Hao Xue, Luna Šošo Zdravković and Daniela Zurkan. In particular, I would like to highlight the daily, active support of Andrea Wilke, who supported me with great patience, especially in the care of the animal lines described here.

I would like to thank René Bernard, Nikolaus Maier, Daniel Parthier, and Benjamin Rost from the Schmitz lab, as well as Paul Turko and Imre Vida from the Institute of Integrative Neuroanatomy for their versatile support. Every exchange with them helped me to better understand my own project.

Finally, there are endless scientists and labs whose trail-blazing works I have not adequately referenced in here – both due to my own ignorance and the unfortunate limitations on reference number in our thesis guidelines. Whether I knew it or not, your contributions to science were essential to this work and I am most grateful for it.

*** * ***

Life is not just about work. There were several people in my life who supported me in completing this thesis without sharing a spark of academic interest. They supported me because they loved me, believed in me, and wished me well. It is a great gift for which I am immensely grateful.

I thank my parents, Adrienne and Dietrich Hadler, for their ongoing support and the immense contribution they both made to fascinating me with nature and people. I thank my siblings, Patricia and Thomas Hadler, for everything and much more.

I thank friends who accepted me as I was and lent me an ear when the stress of this project overwhelmed me. I want to especially thank Max Krafft, who became like a brother to me during this time.

To Luise and Levi, I thank them for their patience when I was not with them, for the inspiration to always carry a smile within me, and for the boundless love they brought into my life. You are perfect.